



University of Pretoria

**Modelling joint parameters to understand the influence of
a pegmatite vein on excessive seepage at the De-Hoop
Dam, South Africa**

by

Katlego Philicia Segole

29313717

Submitted in partial fulfilment of the requirements for the degree

MSc Engineering Geology

In the Faculty of Natural and Agricultural Sciences

University of Pretoria

2018

DECLARATION OF ORIGINALITY/ DECLARATION ON PLAGIARISM

The **Department of Geology (University of Pretoria)** places great emphasis upon integrity and ethical conduct in the preparation of all written work submitted for academic evaluation. Whilst academic staff teaches you about referencing techniques and how to avoid plagiarism, you too have a responsibility in this regard. If you are at any stage uncertain as to what is required, you should speak to your lecturer before any written work is submitted.

You are guilty of plagiarism if you copy something from another author's work (a book, an article or a website) without acknowledging the source and pass it off as your own. In effect you are stealing something that belongs to someone else. This is not only the case when you copy work word-for-word (verbatim), but also when you submit someone else's work in a slightly altered form (paraphrase) or use a line of argument without acknowledging it. You are not allowed to use work previously produced by another student. You are also not allowed to let anybody copy your work with the intention of passing it off as his/her work.

Students who commit plagiarism will not be provided any credit for plagiarised work. The matter may also be referred to the Disciplinary Committee (Students) for a ruling. Plagiarism is regarded as a serious contravention of the University's rules and can lead to expulsion from the University.

The declaration which follows, must accompany all written work submitted, whilst you are a student of the **Department of Geology (University of Pretoria)**. No written work will be accepted, unless the declaration has been completed and attached.

I, the undersigned, declare that:

1. I understand what plagiarism is and am aware of the University's policy in this regard.
2. I declare that this assignment (essay, report, project, assignment, dissertation, or thesis) is my own original work. Where other people's work has been used (either from a printed source, the internet or any other source), this has been

properly acknowledged and referenced in accordance with Departmental requirements.

3. I have not used work previously produced by another student or any other person to submit as my own.
4. I have not allowed, and will not allow, anyone to copy my work with the intention of passing it off as his or her own work.

I, Katlego Philicia Segole, declare that the dissertation, which I hereby submit for the degree MSc Engineering at the University of Pretoria, is my own work and I have not submitted it previously for a degree at any other tertiary institution.

Student: Katlego Philicia Segole

Student number: 29313717


Date submitted: 2018

Topic of work: Modelling joint parameters to understand the influence of a pegmatite vein on excessive seepage at De-Hoop Dam, South Africa

Signature: Ms K.P. Segole

Supervisor: Prof. Jan Louis Van Rooy, Department of Geology

I, Katlego Philicia Segole, declare that the thesis/dissertation, which I hereby submit for the degree Master of Science in Engineering Geology at the University of Pretoria, is my own work and has not previously been submitted by me for a degree at this or other institution.

SIGNATURE: 

DATE: 31 July 2018

ABSTRACT

Water supply dams are essential infrastructural components, contributing to water security, ensuring economic growth. The construction of De Hoop Dam in South Africa is no exception. Water supply needs to keep abreast with the rapidly growing district in Limpopo. Prior to construction, detailed ground investigations are conducted that ultimately inform the design and construction methods. Certain water losses are anticipated, irrespective of conducted studies. Seepage levels are capped at certain flow rates, provided no safety concerns arise. External from these flow rates, leakage and excessive seepage is assumed. This is primarily identified through Lugeon testing. Several features were identified. This study focusses on the pegmatite feature. Through back analysis, the study examines the influence of joint parameters, aperture and roughness, comprehending the excessive seepage that the pegmatite vein exhibits. This analysis is achieved through a single fracture plexiglass model, based on parallel-plate assumptions. Appropriately sized strips are used to simulate the applicable aperture. An altered plexiglass plate and two diverse rock samples with varying uneven surfaces, are casted to examine the influence of uneven surfaces on the fluid flow. Possible flow regimes or flow structures associated with the varying aperture and roughness can then be identified, deducing favourable discontinuity surface conditions, inciting a pronounced flow. From the collected data, minute differences between the average joint roughness coefficient values, for variously grouped fracture faults grouped from the dam site, denote that a higher roughness coefficient value does not imply a pronounced fluid flow; joint roughness coefficient can be misleading. The visual experiments from this study, illustrate that an interplay between gravitational and capillarity forces, influences liquid flow migration. No specific aperture and roughness conditions leads to a pronounced flow. These experiments do not identify the occurrence of any distinct flow structures. Localised preferential fluid flow migration, with variable aperture or roughness conditions, either promoting or inhibiting flows, are observable. The excessive seepage recognised at De Hoop Dam, cannot be attributed to a single or a definite joint parameter, resulting in distinct flow structures. A combination of variable fracture parameters, resulting in preferential flow pathways, are indicated. This is a favourable condition for a pronounced flow.

TABLE OF CONTENTS

DECLARATION OF ORIGINALITY/ DECLARATION ON PLAGIARISM.....	i
ABSTRACT	iv
LIST OF FIGURES.....	ix
LIST OF TABLES.....	xv
LIST OF ACRONYMS/DEFINITIONS/ABBREVIATIONS.....	xvi
Chapter 1 : INTRODUCTION	1
1.1. Rational.....	1
1.2. The aim of the research	3
1.3. Objectives	4
Chapter 2 : LITERATURE REVIEW	6
2.1. Unsaturated (<i>vadose</i>) zone.....	6
2.2. Fracture flow	8
2.3. Flow regimes in fractured rock	10
2.3.1. Discrete and continuous liquids.....	10
2.4. Joint descriptor.....	20
2.4.1. Aperture	21
2.4.1.1 Definition.....	21
2.4.1.2 Joint aperture measurement techniques.....	24
2.4.1.3 Effects of joint aperture on fracture flow	30
2.4.2. Roughness (Asperities).....	37

2.4.2.1	Definition.....	37
2.4.2.2	Measurement and characterisation of joint roughness	39
2.4.3.	Effects of roughness on fracture flow	47
Chapter 3 : MATHEMATICAL AND NUMERICAL MODELLING		56
3.1.	Mathematical modelling	56
3.1.1.	Navier-Stokes and Reynolds number.....	56
3.1.2.	Parallel-plate model	64
3.2.	Numerical modelling techniques	65
Chapter 4 : BACKGROUND OF DE HOOP DAM		69
4.1.	Site location and description	70
4.2.	Regional geology	72
4.2.1.	Left flank geology	73
4.2.2.	Pegmatite vein in the left flank	74
4.3.	Statistical and comparative analysis of left flank joint line surveys dam data..	82
4.4.	Current state of left flank seepage flow	89
Chapter 5 : MATERIALS AND METHODS.....		91
5.1.	Experimental set-up	92
5.1.1	Model description	92
5.1.2	Roughness tests	93
5.2.	Experimental procedure	98

Chapter 6 : RESULTS	102
6.1. Aperture	102
6.1.1. 0.18mm Aperture	102
6.1.2. 0.5mm Aperture	105
6.1.3. 1.0mm Aperture	107
6.1.4. 1.5mm Aperture	108
6.1.5. 2.0mm Aperture	111
6.1.6. 3.0mm Aperture	112
6.2. Roughness	115
6.2.1. R ₁ (JRC 0-2).....	115
6.2.2. R ₂ (JRC 4-6).....	115
6.2.3. R ₃ (JRC 10-12).....	117
6.2.4. R ₄ (JRC 14-16).....	119
Chapter 7 : DISCUSSION	122
7.1. Limitations and assumptions of this study	126
7.2. Main findings and progress	127
ACKNOWLEDGEMENTS	130
REFERENCES	131
APPENDIX I <i>In situ</i> joint line descriptions	I-I
APPENDIX II As built foundation maps.....	II-I
APPENDIX III Pegmatite vein identified in different foundation blocks.....	III-I

LIST OF FIGURES

Figure 1.1	Summarised procedure of the adopted back analysis	4
Figure 2.1:	Vertical cross-section indicating the definitions of terms used to describe the subsurface water	6
Figure 2.2:	Geological variability of the <i>vadose</i> zone	7
Figure 2.3:	Types of discontinuities	8
Figure 2.4:	Examples of fracture geometric features that trigger fragmentation: (a) Localised plug, (b) fracture discontinuity, and (c) fracture intersection.....	13
Figure 2.5:	Idealised representation of liquid bridge suspended below fracture discontinuity and schematic illustration of elongation and extension of a typical fluid element	14
Figure 2.6:	Growth and elongation of a liquid bridge, attached to a solid obstruction within a fracture. Time and Bond number (Bo) increase from left to right. The liquid element elongate (deviate from semi-circular shape) when $Bo > Bo^*$	14
Figure 2.7:	Relative velocity of travelling liquid bridges for a wide range of fracture apertures and three values of $\Delta\theta$ (0.01, 0.1 and 0.5) (Different values of result in different critical lengths at detachment with associated different velocities).....	15
Figure 2.8:	Average velocity of travelling liquid bridges (lines) and film (dashed lines) for a wide range of volumetric fluxes; fracture apertures of 0.2mm (blue lines) and 1mm (red lines). The vertical lines (at fluxes of 10^{-8} m ³ /day and 10^{-4} m ³ /day) mark values used for comparison of distance of liquid bridges and film.....	16
Figure 2.9:	Comparison of distances travelled by liquid bridges (solid lines) and film (dashed lines) down a fracture in one day, assuming an infinitely long fracture and constant flow rates of 10^{-8} m ³ /day (red lines) and 10^{-4} m ³ /day (blue lines) along a 1cm wide fracture section.....	17

Figure 2.10:	(a) Film flow does not span the aperture and only wets one wall at a time, h is the film thickness, w is the film width and W is the width of the fracture plane. (b) Droplet with rivulets span the aperture and are under capillary tension. (c) Non-snapping rivulet spans the aperture and is under capillary tension, width (w) of the rivulet depends on flow rate. (d) Droplet after rivulet has snapped has curved meniscus at the advancing and receding ends. Radius of curvature of menisci in the plane of the fracture wall is much greater than in the plane that spans the aperture. (e) Cross-sectional sketch in the plane of the fracture aperture for (A-A') film, (B-B') rivulet and (C-C') droplets	19
Figure 2.11:	Geometric properties of discontinuities to be recorded	20
Figure 2.12:	Fracture properties determined by fracture void geometry.....	21
Figure 2.13:	Definition of fracture aperture, $b(x,y)$	22
Figure 2.14:	Illustration of the various aperture definitions as defined	22
Figure 2.15:	Techniques for measuring joint aperture.....	25
Figure 2.16:	Various approaches to measure fracture void geometry.....	28
Figure 2.17:	Aperture measurement technique	29
Figure 2.18:	Effect of stress on a single rock	31
Figure 2.19:	a) Normal stress (b) Shear stress on the aperture of a rough fracture (c) the influence of stress on a smooth fracture	32
Figure 2.20:	Residual apertures for different granitic rock samples with single fracture	32
Figure 2.21:	Effects of loading and unloading on flow characteristics of jointed rock	33
Figure 2.22:	Fracture specific stiffness and fluid flow through a fracture are implicitly related through the geometry of the fracture.....	35

Figure 2.23:	Flow per unit head as a function of normal stress for thirteen different samples, each containing a single fracture	36
Figure 2.24:	Asperities in fracture walls	37
Figure 2.25:	Roughness of a discontinuity surface.....	38
Figure 2.26:	Categories of roughness.....	39
Figure 2.27:	Roughness profile	40
Figure 2.28:	Example of straight edge method used to measure the waviness of a rock discontinuity.....	42
Figure 2.29:	Measured profile used to estimate JRC value.....	42
Figure 2.30:	Measurement of local surface orientation with circular discs of varying sizes, fixed to clar-type compass	43
Figure 2.31:	Graph used to determine JRC value	44
Figure 2.32:	Available profilometers based on modes of measurement.....	47
Figure 2.33:	Flow through a single fracture: (a) Natural fracture; (b) Idealised fracture	48
Figure 2.34:	Real aperture E to Induced aperture E_m variation	51
Figure 2.35:	X- and Y- velocity components across the fracture aperture.....	54
Figure 2.36:	Shear rate distribution across the fracture aperture	55
Figure 3.1:	Relationship of flow behaviour to relative roughness and Reynolds Number	63
Figure 3.2:	Joint flow relationship based on pressure drop coefficient, Reynolds number and relative roughness.....	63
Figure 4.1:	De Hoop Dam (Labuschagne, 2013).....	69

Figure 4.2:	Extract from the 1:250 000 topocadastral sheet, 2430 Pilgrim's Rest (2000), indicating the locality of the De Hoop farm.....	70
Figure 4.3:	Plan view of De Hoop Dam and investigated area	71
Figure 4.4:	Extract from the 1: 250 00 sheet, 2428 Nylstroom (1978), indicating regional geology of the study area	73
Figure 4.5:	Approximate location of pegmatite vein, with an approximate width of 250mm	75
Figure 4.6:	Exploded view of the highly weathered and jointed pegmatite vein...	76
Figure 4.7:	Geologic setting of some of the discordant bodies of ultramafic rock in part of the eastern Bushveld Complex	78
Figure 4.8:	(A) Zonal subdivision of the layered sequence in the eastern limb of the Bushveld Complex concerning important marker layers. (B) Vertical distribution of the different types of discordant ultramafic body	79
Figure 4.9:	Major element analysis of three samples	80
Figure 4.10:	Mineralogical content of three samples.....	81
Figure 4.11:	Climatic N-value = 5 plotted for southern Africa (From Weinert, 1980)	82
Figure 4.12:	Illustration of the final combined JLS data sheet.....	83
Figure 4.13:	a) Stereographic projections of the tension joints with two prominent sets. b) Stereographic projections of the fracture faults with fracture sets. c) Stereographic projections of the stress relief joints	86
Figure 4.14:	Fracture fault stereographic projection of high permeability blocks	88
Figure 4.15:	Fracture fault stereographic projection of low permeability blocks .	89
Figure 5.1:	Simple classification of modelling materials	91

Figure 5.2: Schematic of plexiglass single; fracture model.....	92
Figure 5.3: Built model;	92
Figure 5.4: Granite sample.....	95
Figure 5.5 Mudrock sample.....	95
Figure 5.6: Casted granite sample	95
Figure 5.7: Casted Mudrock sample.....	95
Figure 5.8: Granite laser scan image	96
Figure 5.9: Mudrock laser scan image	97
Figure 5.10: Schematic of experimental set-up.....	98
Figure 5.11: (A) Festo valve with 6mm diameter openings on either side. (B) Top view of the valve, further illustrating the numbering of the ridges. The rectangular red blocks serve as points where the ridge needs to align when opened.....	99
Figure 5.12: Approximated flow velocity of various tests.....	101
Figure 6.1: 0.18mm Aperture, water flow movement at 38% flow (Test 3)	103
Figure 6.2: 0.18mm Aperture, water flow movement at 63% flow (Test 5)	104
Figure 6.3: 0.18mm Aperture, water flow movement at 100% flow (Test 8)	104
Figure 6.4: 0.5mm Aperture, water flow movement at 38% flow (Test 3)	105
Figure 6.5: 0.5mm Aperture, water flow movement at 63% flow (Test 5)	106
Figure 6.6: 0.5mm Aperture, water flow movement at 100% flow (Test 8)	106
Figure 6.7: 1mm Aperture, water flow movement at 38% flow (Test 3)	107
Figure 6.8: 1mm Aperture, water flow movement at 63% flow (Test 5)	107
Figure 6.9: 1mm Aperture: water flow movement at 100% flow (Test 8)	108

Figure 6.10:	1.5mm Aperture, water flow movement at 38% flow (Test 3).....	109
Figure 6.11:	1.5mm Aperture, water flow movement at 63% flow (Test 5).....	110
Figure 6.12:	1.5mm Aperture, water flow movement at 100% flow (Test 8).....	110
Figure 6.13:	2mm Aperture, water flow movement at 38% flow (Test 3).....	111
Figure 6.14:	2mm Aperture, water flow movement at 63% flow (Test 5).....	111
Figure 6.15:	2mm Aperture, water flow movement at 100% flow (Test 8).....	112
Figure 6.16:	3mm Aperture, water flow movement at 38% flow (Test 3).....	112
Figure 6.17:	3mm Aperture, water flow movement at 63% flow (Test 5).....	113
Figure 6.18:	3mm Aperture, water flow movement at 100% flow (Test 8).....	113
Figure 6.19:	The change in linear flow velocity with a change in aperture	114
Figure 6.20:	The influence of aperture (ϵ) on fracture conductivity (K_f).....	114
Figure 6.21:	R ₂ (JRC 4-6), water flow movement at 38% flow (Test 3).0	116
Figure 6.22:	R ₂ (JRC 4-6), water flow movement at 63% flow (Test 5)	116
Figure 6.23:	R ₂ (JRC 4-6), water flow movement at 100% flow (Test 8)	117
Figure 6.24:	R ₃ (JRC 10 - 12), water flow movement at 38% flow (Test 3)	118
Figure 6.25:	R ₃ (JRC 10-12), water flow movement at 63% flow (Test 5)	118
Figure 6.26:	R ₃ (JRC 10-12), water flow movement at 100% flow (Test 8)	119
Figure 6.27:	R ₄ (JRC 14-16), Water flow movement at 38% flow (Test 3)	120
Figure 6.28:	R ₄ (JRC 14-16), water flow movement at 63% flow (Test 5)	121
Figure 6.29:	R ₄ (JRC 14-16), water flow movement at 100% flow (Test 8)	121

LIST OF TABLES

Table 2.1:	Various accelerating and retarding forces responsible for subsurface movement of flow	11
Table 2.2:	Classification of joint apertures by its magnitude.....	26
Table 2.3:	Description of aperture	27
Table 2.4:	Roughness scale.....	38
Table 2.5:	Description of roughness.....	45
Table 2.6:	Validity of cubic law to different types of fractures under varying stress conditions	49
Table 2.7:	Estimated real apertures and induced apertures.....	50
Table 3.1:	Flow laws concerning water flow in a joint (frequency is equal to 1) .	60
Table 3.2:	The unit flow rate and pressure drop coefficient for a single fracture	62
Table 3.3	Typical numerical modelling methods for fluid flow through fractured rock	67
Table 4.1:	Summary of the three dam wall zones	72
Table 4.2:	A summary for s the average parameter values for three discontinuity types	84
Table 4.3:	A summary for the average values obtained for high and low permeability fault fractures zones.....	87
Table 4.4:	Five areas of significant seepage flows.....	90
Table 5.1:	Ridges corresponding to flow rate	100

LIST OF ACRONYMS/DEFINITIONS/ABBREVIATIONS

APES	Academic and Professional Editing Services
CRC	Chemical Rubber Company
DFN	Discrete Fracture Network
DHDC	De Hoop Dam Consultants
DSP	Dam Safety Programs
DWS	Department of Water and Sanitation
HDR	Hot Dry Rock
ISRM	International Society for Rock Mechanics
JCS	Joint Compressive Strength
JLS	Joint Line Surveys
JRC	Joint Roughness Coefficient
KPC	Knight Piesold Consulting
NS	Navier-Stokes
ORWRDP	Olifants River Water Resources Development Project
RCC	Roller Compacted Concrete
RLS	Rustenburg Layered Suite
SC	Stochastic Continuum
SF	Single Fracture
TP	Triple Porosity
USRMS	United States Symposium on Rock Mechanics

CHAPTER 1 : INTRODUCTION

1.1. Rational

Dams signify global important development infrastructures. They hold various purposes, such as water supply, irrigation, flood control and hydroelectric power. Secure water supply is one of several components, essential for economic growth (González De Vallejo & Ferrer, 2011).

De Hoop Dam, on Steelpoort River, South Africa, is constructed to supply bulk water to the rapidly expanding Sekhukhune district in the Limpopo province. The dam supplies water to the construction and mining industries, including approximately 800 000 residents of the Nebo Plateau (Davies, 2006; Van Vuuren, 2008).

Dam safety is crucial throughout the planning, construction and operation phases. Effective, continuous and constant monitoring of dams, allowing for early detection of possible dam safety issues, is imperative to ensure human safety (Chinh & Radzicki, 2014; González De Vallejo & Ferrer, 2011).

According to Bedmar and Araguas (2002), some water loss may be expected, irrespective of conclusions of studies prior to the construction phase, or preventative measures taken during the construction phase. It is not always possible to accurately predict the hydraulic behaviour of a dam wall, or the underlying and proximate geological formations. A certain level of seepage is therefore allowed if no safety concerns arise. Seepage effects are critical for dam foundations as it may lead to the ultimate failure of the dam construction through:

- Piping at the dam toe (the junction of the downstream face of a dam with the natural ground surface), contacts of the dam wall with the foundation, or underlying geology.
- Blow out due to excessive uplift pressure below the dam foundation.

- Excessive seepage (leakage) below the dam foundation (Bedmar & Araguas, 2002; González De Vallejo & Ferrer, 2011).
- Slope failures associated with insufficient filters, on down or upstream faces.
- Movement of materials within the foundation, or abutments along planes of weakness.

According to Bedmar and Araguas (2002), assessing risks and consequences derived from an excessive seepage, is an essential aspect of Dam Safety Programs (DSPs). It is important to curb the effects of uncontrolled seepage of the dam stability, including complementary structures and surrounding geological formations, regarding financial and safety concerns.

Discontinuities are considered to be the most important hydrogeological structures, should the factors and processes governing fracture flow be understood, to implement proper water seepage control strategies, during construction or excavation (Singhal & Gupta, 2010).

An accepted practice of describing discontinuity parameters affecting flow, is through numerical methods (Barker, 1988; Cacas *et al.*, 1990; Cundall & Hart, 1992; Rutqvist *et al.*, 2002; Tsang & Tsang, 1987; Wu, 2002). Subsequently, these methods proved the successful application to produce accurate and reliable results. This is attainable through extensive simulations of nonequilibrium flow processes, based on elaborated field data. The data aid in comprehending and determining pronounced results of heterogeneities, including the impact of fractures on a flow (Jing, 2003; Van Genuchten *et al.*, 1999).

Physical and empirical models, in the form of single fracture (SF) experimental studies, such as the disciplines of hydrology and petroleum engineering, provide the basis for fracture flow behaviour, differentiating various interactions, such as fracture-matrix and hydromechanical research disciplines (Lomize, 1951; Louise, 1969; Pyrak-Nolte *et al.*, 1987; Witherspoon *et al.*, 1980). There is still a universal preference, indicating

empirical models as base for fracture flow modelling, due to complexities associated with rock mass modelling (Iwai, 1976; Lomize, 1951; Qian, *et al.*, 2011).

The magnitude of variables that can be incorporated into an experimental model, limits SF studies. This normally indicates a plane strain, such as 2D. Significant results were collected, providing practical insight on flow. Examples of these studies include illustrating scale-dependent hydraulic conductivity through experimental SF studies (Qian *et al.*, 2007) and impacts of isolated fractures on flow (Barton *et al.*, 1995).

This research adopts the use of a back analysis procedure. Figure 1.1, signifies investigating the influence of a pegmatite vein on the excessive seepage at De Hoop Dam, through SF flow analysis. Physical modelling was used to examine the influence of varying aperture and roughness, considering the most vital properties governing flow, on flow through an SF (Barton & Quadros, 1997; Brown, 1987; Brush & Thompson, 2003; Hakami & Larsson, 1996; Liu, 2005).

1.2. The aim of the research

The aim of this research is to establish how the pegmatite vein contributes to the excessive seepage at De Hoop Dam, through physically modelling the joint parameters affecting flow, and to extrapolate the data to the pegmatite vein. Figure 1.1 illustrates the research procedure.

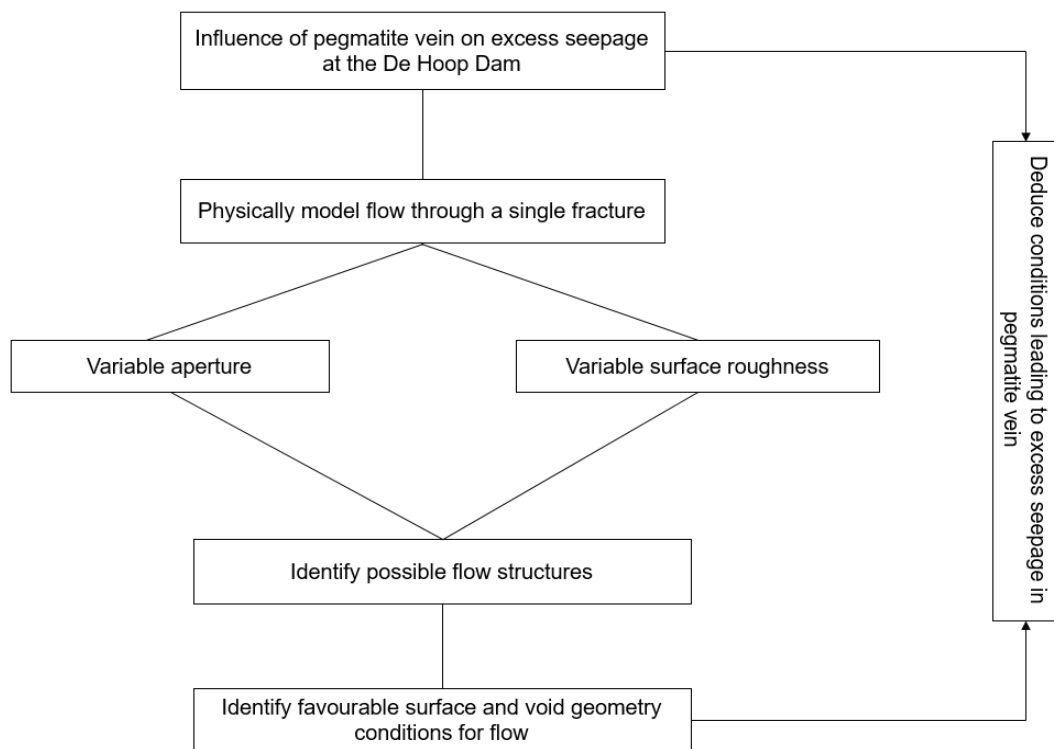


Figure 1.1 Summarised procedure of the adopted back analysis

1.3. Objectives

The following objectives outline the scope for this study:

- Conduct a literature survey examining rock fracture flow, prominent flow mechanisms and flow regimes, including influences of aperture and roughness on flow, with various modelling techniques.
- Compare geological foundation maps of De Hoop Dam with scanline survey data.
- Model the influence of varying roughness and aperture on flow, through an SF, by changing the limit conditions of one parameter and keeping the other constant within the fracture.
- Deduce the influence of the aperture and roughness fracture properties on flow, quantifying these changes with linear flow velocity.
- Identify flow regimes observed in the various SF tests.

- Establish an association between the physical model, the discontinuity parameters of the pegmatite vein, and the contribution thereof on excessive seepage.

CHAPTER 2 : LITERATURE REVIEW

Understanding groundwater flow through rock fractures, flow in the unsaturated (*vadose*) zone including influences of discontinuity properties on the influence flow is crucial prior to constructing an appropriate model. The literature review emphasises predominant fracture flow mechanisms, flow regimes and discontinuity properties, indicating aperture and roughness, affecting flow.

2.1. Unsaturated (*vadose*) zone

The unsaturated (*vadose*) zone (Figure 2.1) is defined as the area of the top subsurface, towards the groundwater table. This includes the plant root, intermediate zones and the capillary fringe. The region is characterised by pore pressures below atmospheric pressure (Fitts 2002, in Dippenaar *et al.*, 2014; Singhal & Gupta 2010).

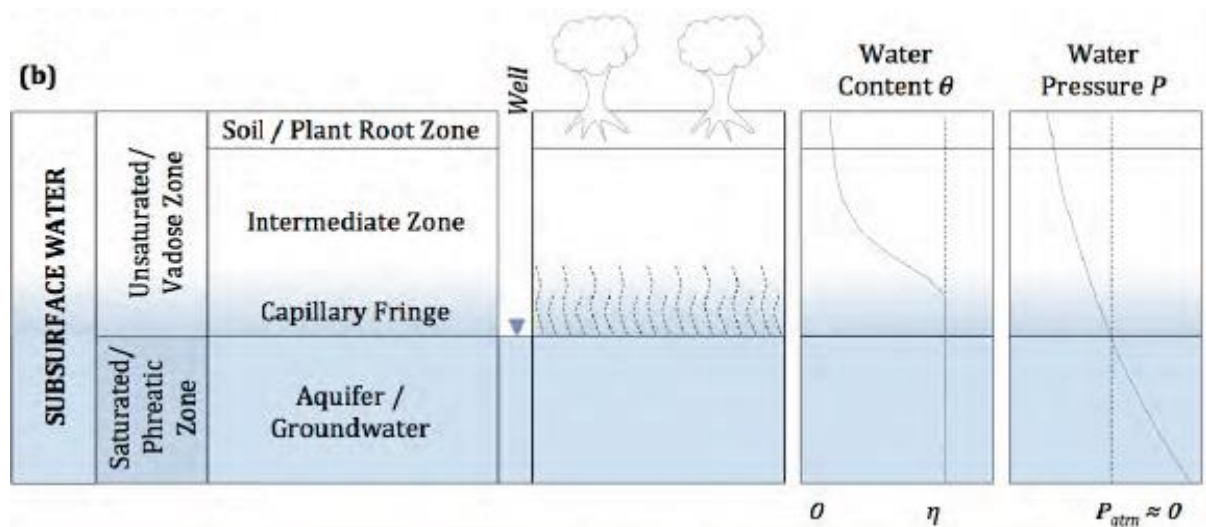


Figure 2.1: Vertical cross-section indicating the definitions of terms used to describe the subsurface water

Source: Dippenaar *et al.* 2014, adapted from Fitts, 2002.

The unsaturated zone additionally comprises soil and or rock, with water flowing over material surfaces in the presence of significant air. Figure 2.2 illustrates the complexity of this subsurface environment.

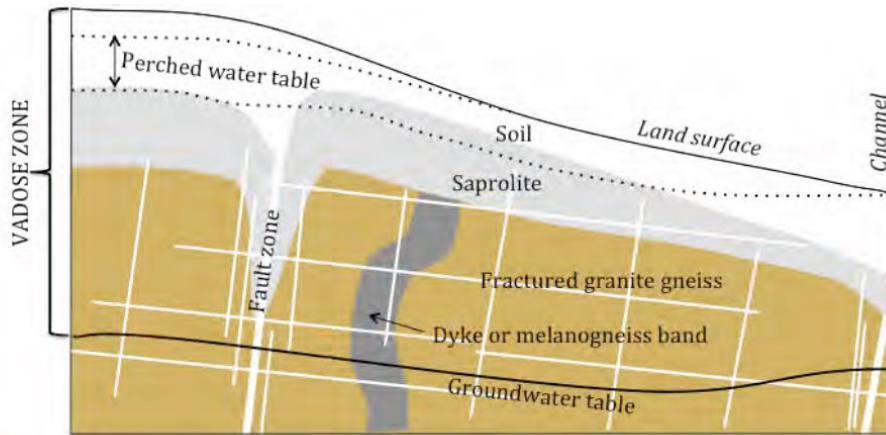


Figure 2.2: Geological variability of the vadose zone

Source: Dippenaar *et al.* 2014.

Variable geological settings in the unsaturated zone explain the mechanisms, controlling preferential and nonequilibrium flow. The following section elaborates on the former process, prevalent in fracture flow. Nonequilibrium flow forms an integral feature of preferential flow. Jarvis (1998) defines flow type as, “which for various reasons, infiltrating water does not have sufficient time to equilibrate with slowly moving resident water in the bulk of the soil matrix”.

Nonequilibrium flows have negative implications, such as the ability to accelerate the mobility of agricultural contaminants (Šimůnek *et al.*, 2003). Preferential flow displays severe implications on potential underground repositories, the migration of contaminants and sanitary landfills (Evans *et al.*, 2001; Neretnieks, 1980; Nicholson & Evans 1987; Tsang & Tsang, 1987).

These mechanisms, combined with transport processes, pose various modelling challenges as they hamper accurate predictions of contaminant transport in soils and fractured rock, including, accurate modelling of fracture-matrix domains. The lack of sufficient data restricts validating field models of preferential flow. Limited models can be applied to natural systems (Šimůnek *et al.*, 2003).

2.2. Fracture flow

Dippenaar *et al.* (2014) define fracture flow as flow that occurs through discontinuities below the ground surface.

Joints (used interchangeably with fractures) indicate types of discontinuity planes, defined as those where stress resulted in partial loss of cohesion in the rock or planes, with zero tensile strength. Figure 2.3 provides additional types of discontinuities, indicating two primary types, specified as planar and linear (Dippenaar *et al.*, 2014; González De Vallejo & Ferrer, 2011).

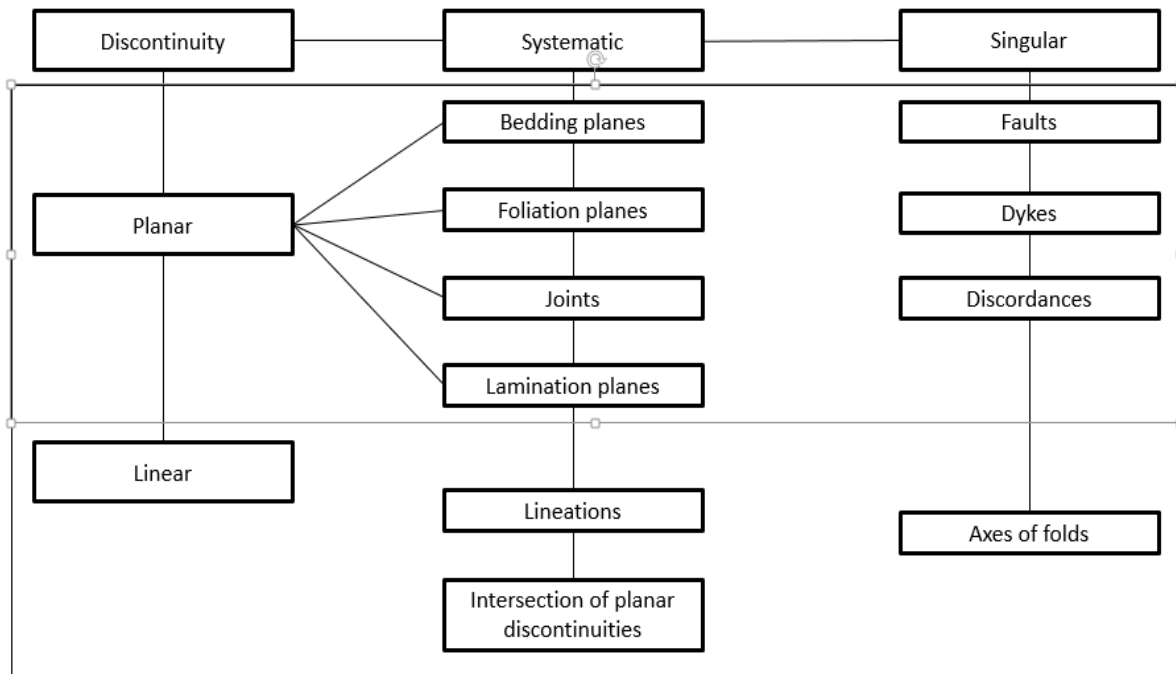


Figure 2.3: Types of discontinuities

Source: Modified from González De Vallejo and Ferrer, 2011.

Fractured rock comprises both fracture zones, characterised by low porosity and large lateral continuity. This includes porous media, characterised by a larger porosity with lesser spatial continuity. For low permeability rock mass, groundwater flow predominantly occurs in discontinuities with flow conductivity, controlled by the degree

of fracturing, the interconnectivity of the discontinuities and their permeability (Zimmerman *et al.*, 1996; Singal & Gupta, 2010).

Hendrickx and Flury (2001, in Šimůnek *et al.*, 2003) define preferential flow as “all phenomena where water and solutes move along certain pathways, whilst bypassing a fraction of the porous matrix”. Whether preferential flow occurs through macropores or fractures, is heavily dependent on the matric potential (Hillel, 1980; Sposito, 1981 in Tokunaga & Wan, 1997).

Field evidence by Faybishenko *et al.* (2000), further illustrates that the mechanism may occur in fracture networks even in the existence of sorptive matrices. According to Neretnieks *et al.* (cited in Hakami & Larsson, 1996), the mechanism further denotes a variation in flow velocities between flow paths on a fracture surface.

Pruess (1999) reports that fast preferential flow in steeply dipping fractures over large vertical distances, is feasible in the presence of permeable rock-matrix at strong suction pressures. Further evidence illustrates that certain fractures, depending on their geological origin (faults), act as important conduits of groundwater flow. Flow occurs at much higher rates under these geological environments.

Su *et al.*, (2003) conducted a study, using Berea sandstone samples from Germany, investigating the physical mechanisms controlling flow in a wide aperture single isolated fracture, oriented at 20° and 60° from the horizontal base. These mechanisms illustrate preferential water flow in the vicinity of the fracture flow, in consort with higher pressures in regions with rapid flow. The conclusion signifies that isolated fractures accelerate water flow in the unsaturated zone.

The term “preferential flow pathway” is used synonymously with “flow channelling”, defined as flow occurring through long and narrow conduits, due to the presence of extensive contact areas in fractures. Aperture variation within these conduits, results in fluid pressure and flow velocity variation over fracture surfaces. It essentially behaves similar to preferential flow, as flow along certain paths is much faster, compared to other flows (Hakami, 1995).

Channelling effects are more pronounced in SFs where apertures are well correlated. These fractures are characteristically as either extensively sheared, or comprising an uneven distribution of infill. On a broader rock mass scale, it is the differences in aperture distribution between individual fractures that significantly increases flow channelling effects. Although it is virtually impossible to directly observe flow channelling through natural fractured rock, research predicts that fluid flow may only occur in approximately 5% to 20 % of the fracture void (Hakami, 1995).

Similarly, Liu *et al.* (1998), upon studying fracture-matrix in the Yucca Mountain, found that 18% to 27% of the connected fractures in the Topopah Spring welded (TSw) unit, are active under ambient conditions. Fluid flow is complicated by large nonlinearities within the unsaturated zone and heterogeneities in the fractures at various scales. Only a portion of the fracture surface is expected to contribute to flow. On a localised fracture surface scale, tortuous flow is discerned, ascending from an improved interaction between the solid and fluid interface (Hakami, 1988, cited in Hakami, 1995).

2.3. Flow regimes in fractured rock

The identification of flow regimes, in the SF model is an imperative exercise, forging a link between observations from the model and possible seepage flow structures in the pegmatite vein. Flow regimes discussed herein focus on “discrete” and “continuous” liquids.

2.3.1. Discrete and continuous liquids

The interaction of a fluid in contact with a solid surface, depends on the wetting properties of both the liquid the solid surface which ultimately affects the occurrence of water on the surface. According to Kovács (1981), a balance between accelerating and retarding forces, is necessary for continuous flow movement. Table 2.1 lists these accelerating and retarding forces in the subsurface.

Table 2.1: Various accelerating and retarding forces responsible for subsurface movement of flow

Accelerating forces	Retarding forces
Gravity	Inertia
Overburden pressure	Friction
Vapour and gas pressure	Adhesion

Source: Kovács, 1981.

Unsaturated (including saturated) fracture flow indicate that where adhesion is insignificant due to lower surface area, gravity will predominantly accelerate flow.

The various means of liquid migration, the formation of flow structures and other complex flow phenomena in the unsaturated media, episodic fluxes, intermittent fluxes and preferential flow paths, result from the interaction between gravity, capillarity, pressure and viscous forces in fractures. These continue even under constant inlet conditions where unsteady or highly variable flow structure processes persist. This further includes portions of flow, undergoing cycles of snapping and reforming (Su *et al.*, 1999).

To appreciate the interplay between the gravity, capillarity, pressure and viscous forces, it is necessary to discuss a feature as minute as a liquid bridge and its influence on flow migration in the unsaturated zone.

According to Su *et al.* (1999), the relative magnitude of the gravity and capillary forces can be quantified, using the bond (Equation 2.1) and capillary (Equation 2.2) numbers, indicating the ratio between capillary and gravity forces, and viscous and capillary forces, respectively:

$$\text{Bo (Bond number)} = \frac{\text{gravity force}}{\text{capillary force}} = \frac{\Delta \rho b^2 \sin \beta}{\sigma \cos \gamma} \quad \text{Equation 2.1}$$

$$\text{Ca (Capillary number)} = \frac{\text{viscous force}}{\text{capillary force}} = \frac{\mu_1 u_1}{\sigma \cos \gamma} \quad \text{Equation 2.2}$$

Where $\Delta\rho$ is the density difference between the infiltrating liquid and the air, g is the gravitational acceleration constant, β is the angle of inclination of the fracture measured from the horizontal; b is the aperture, σ is the liquid surface tension, μ_l is the viscosity of the liquid, u_l is the velocity of the liquid and $\beta\gamma$ is the contact angle of the wetting phase on the solid surface.

Measurements of infiltration and flow in unsaturated fractured rock from the field, led to the realisation that significantly intermittent fluxes emerge from fractures. Laboratory experiments in fracture analogues verified the statement, involving the formation and detachment of discrete liquid bridges, liquid fragmentation and fingering within various fracture geometries. Consequently, this revealed that flow through an unsaturated fracture network occurs most likely, in the form of string of dripping spouts, opposed to continuous flow. This is predicted by Darcy and Richards' equations, posing challenges to the standard continuum theories (Faybishenko *et al.*, 2003 and 2000, cited in Ghezzehei & Or, 2005; Ghezzehei & Or, 2007).

Liquid bridges arise due to asperities in fracture surfaces and other geometrical variabilities, serving as an attachment for capillary forces in emergent liquid bridges (Su *et al.*, 2004). Figure 2.4 illustrates liquid, accumulating beneath a local plug or asperity within a fracture with an invariant aperture. Asperities may form due to sediment deposition, irregularities between unmatched surfaces, elicited by faulting, formation by localised precipitation and biomass accumulation, due to bacteria (Dobson *et al.*, 2003; Geller *et al.*, 2000).

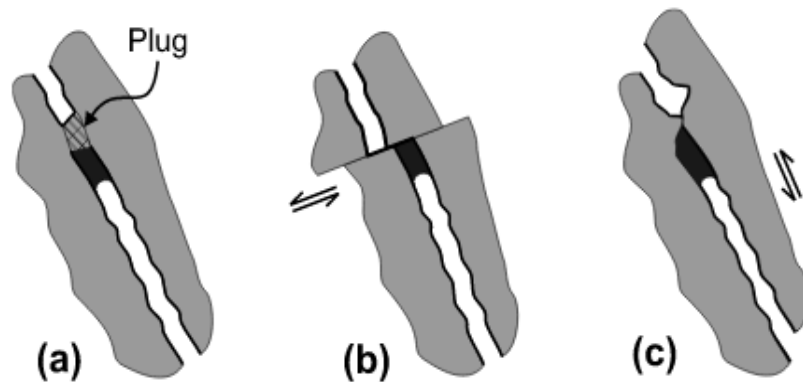


Figure 2.4: Examples of fracture geometric features that trigger fragmentation: (a) Localised plug, (b) fracture discontinuity, and (c) fracture intersection

Source: Ghezzehei and Or, 2005.

A sufficient supply of liquid redirected to the point of anchoring, either as film or matrix flow, perpetuates the cyclical occurrence of intermittent liquid accumulation and detachment when a liquid mass exceeds stabilising capillary forces. Figure 2.5 considers a fracture of uniform aperture b , inclined at an angle of α from a horizontal plane with a constant volumetric flow rate Q , diverted towards obstruction forming a liquid bridge beneath it. The conversion from a gradually accumulating anchored liquid bridge to a finger-forming mobile liquid bridge, results from an interplay between retarding capillary and accelerating forces, and gravitational and viscous (Or & Ghezzehei, 2007).

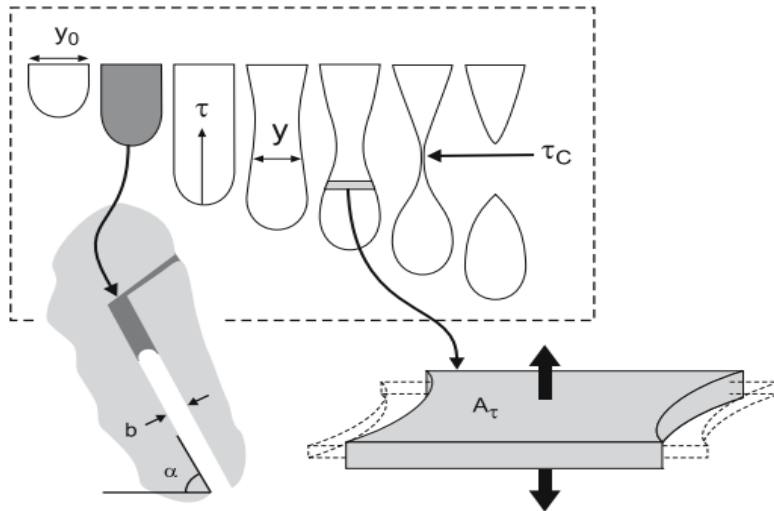


Figure 2.5: Idealised representation of liquid bridge suspended below fracture discontinuity and schematic illustration of elongation and extension of a typical fluid element

Source: Or and Ghezzehei, 2007.

When the lateral extent of the liquid mass exceeds the fracture aperture ($y \gg b$), the Bo number (increase in gravitational forces relative to capillary forces) either increases with the diameter of the liquid mass y , or the inclination of angle α . The liquid bridge consequently responds to the increasing Bo number, through adjusting the increasing or decreasing contact angles, assuming an elongated geometry (Figure 2.6).

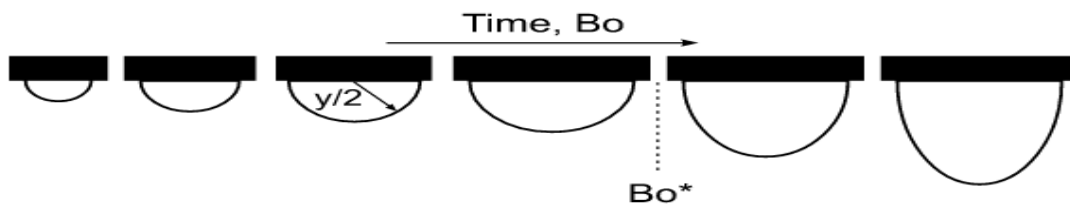


Figure 2.6: Growth and elongation of a liquid bridge, attached to a solid obstruction within a fracture. Time and Bond number (Bo) increase from left to right. The liquid element elongate (deviate from semi-circular shape) when $Bo > Bo^*$

Source: Ghezzehei and Or, 2005.

According to Or and Ghezzehei (2007), liquid accumulation post onset elongation, results in an increase of bridge length with a uniform and constant width, provided the interfacial (capillary) forces remain higher than the weight of the suspended liquid bridge. Detachment will occur at a certain critical value of weight of suspended liquid bridge, where a narrowing and gradually stretching neck appears.

Differences in velocities between detached liquid bridges and velocities for a range of various fracture apertures and their interactions with smooth and rough fracture walls, are examined. Figure 2.7, observes that the length of the detached liquid bridge concerning the fixed length, increases with aperture. For instance, a significantly large initial bridge length arises in fractures with a relatively wide aperture (~1mm) resulting in a velocity, comparable to the saturated hydraulic conductivity. It is concluded that these accelerated discrete cluster velocities, with an absent hydraulic conductivity, fail to meet present continuum estimations (Or & Ghezzehei, 2007).

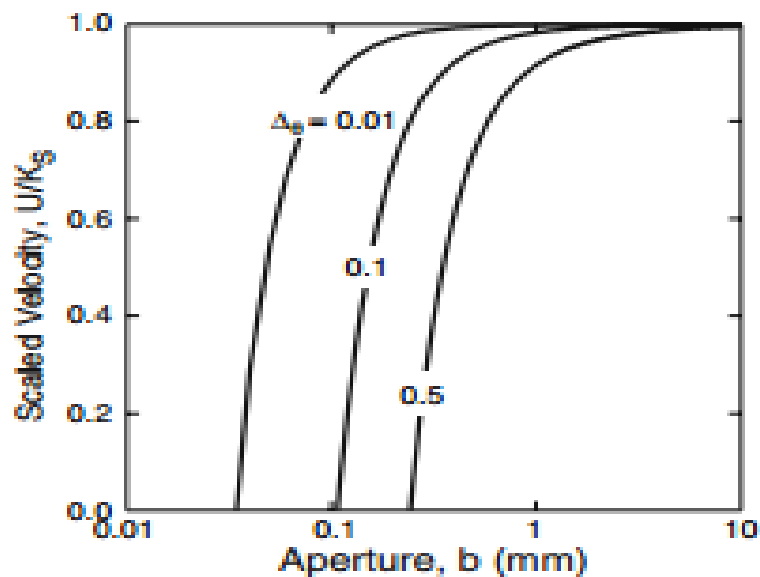


Figure 2.7: Relative velocity of travelling liquid bridges for a wide range of fracture apertures and three values of $\Delta\theta$ (0.01, 0.1 and 0.5) (Different values of result in different critical lengths at detachment with associated different velocities)

Source: Or and Ghezzehei, 2007.

Speed suppression of droplets, increased with droplet speed. This reduced the maximum flow rate of liquids, conveyed by capillary droplet structure processes. Capillary droplets still managed to advance liquids at velocities, exceeding film flow for the same flow rate. This further indicates, relative to film flow, increased speed of capillary droplets, holding the capacity to erode fracture surfaces (Or & Ghezzehei (2007)).

Figure 2.8 compares velocities of discrete liquid clusters with continuous film flow for two fracture apertures, over a wide range of volumetric fluxes. These indicate that discrete discontinuous liquid clusters, travel faster than continuous film flow. Disparities between the two flow processes, diminish near dry or saturation conditions, whilst close to saturation continuous film flow velocity, approaches a maximum of an infinitely extended liquid bridge (Or & Ghezzehei, 2007).

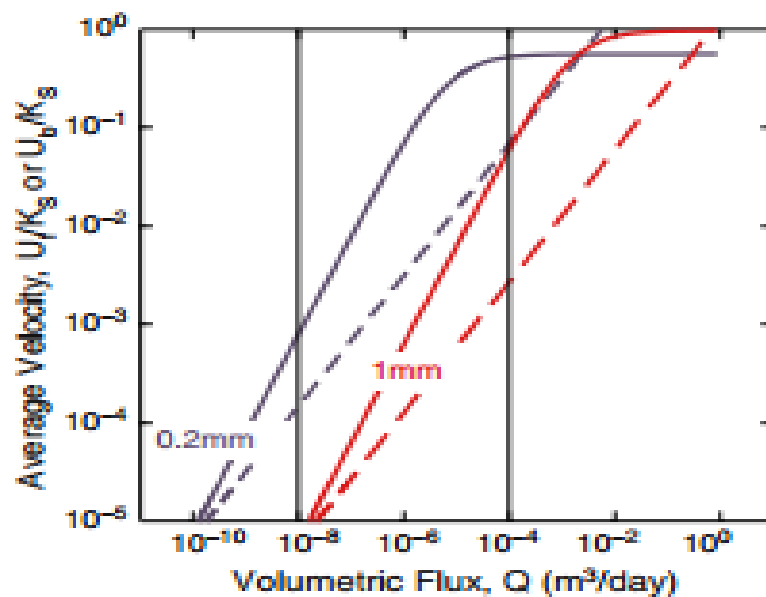


Figure 2.8: Average velocity of travelling liquid bridges (lines) and film (dashed lines) for a wide range of volumetric fluxes; fracture apertures of 0.2mm (blue lines) and 1mm (red lines). The vertical lines (at fluxes of 10^{-8} m³/day and 10^{-4} m³/day) mark values used for comparison of distance of liquid bridges and film

Source: Or and Ghezzehei, 2007.

An examination at distances travelled by liquid bridges and steady film (in a single day for two theoretical fluxes of $10^{-8} \text{ m}^3/\text{day}$ and $10^{-4} \text{ m}^3/\text{day}$) with an infinitely long vertical fracture and with a 1cm aperture, reveals that discrete liquid bridges transverse considerably higher distances than travelled by continuous film flow (Figure 2.9). This illustrates that the formation and growth discrete liquid bridges in fractured rock, result in an enhancement in travel distances and distance travelled (Or & Ghezzehei, 2007).

Rough fractures, opposed to smooth surfaces, shorten liquid bridge travel distances. These sorts of obstructions provide more areas for coalescence of following liquid bridges, travelling on a similar pathway. Consequently, relative to smooth fractures, the liquid mass growth and formation of larger liquid bridges, result in more travel distance (Or & Ghezzehei, 2006).

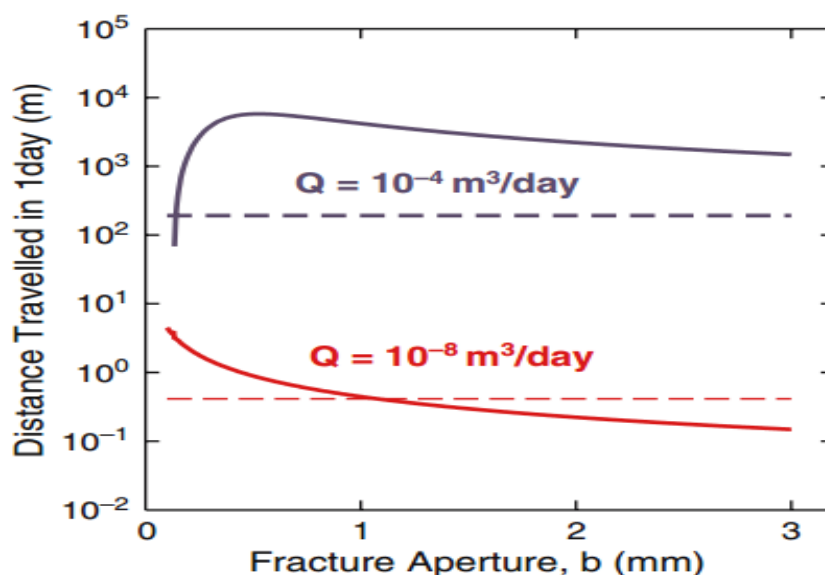


Figure 2.9: Comparison of distances travelled by liquid bridges (solid lines) and film (dashed lines) down a fracture in one day, assuming an infinitely long fracture and constant flow rates of $10^{-8} \text{ m}^3/\text{day}$ (red lines) and $10^{-4} \text{ m}^3/\text{day}$ (blue lines) along a 1cm wide fracture section

Source: Or and Ghezzehei, 2007.

Dragila and Weisbrod (2003) identified film flow and capillary droplets with snapping rivulets as the main flow structure processes, occurring in wide apertures (~1.7mm). Additional fracture properties, affecting the width of an advancing liquid rivulet and mass of detached liquid, include the contact angle and inclination.

Film flow structures display intricate wave structures on free surfaces. Changes in flow rates are balanced, by modifying the film width, resulting in equivalent velocity changes (Kapitza & Kapitza, 1949). Similarly, the mechanism was identified, contributing to accelerated flow in low permeability matrix fractures in areas of convergent flow in partially saturated fractures (Tokunaga & Wan, 1997).

Hydraulic conductivity measurements of an unconfined block of Bishop Tuff (from the Owens River, Gorge) was performed, including and excluding wax sealing of its lateral surfaces, allowing isolation of film flow effects, over areas of near-zero matric potentials (Klute, 1986 cited in Tokunaga & Wan, 1997).

Surface film measured in the unconfined block, was more significant for matric potentials exceeding 250 Pa. In these potentials, the distribution of film thickness increased proportionally with the (closer to zero) matric potential and the observed enhanced hydraulic conductivity. Similar experiments were conducted, using rough and polished surface blocks. The total water uptake between the two different surface blocks were compared. It emerged that more water exchanged in the near-zero matric potential range, associated with the rough surface blocks. Figure 2.10 illustrates a summary of the discussed flow structures.

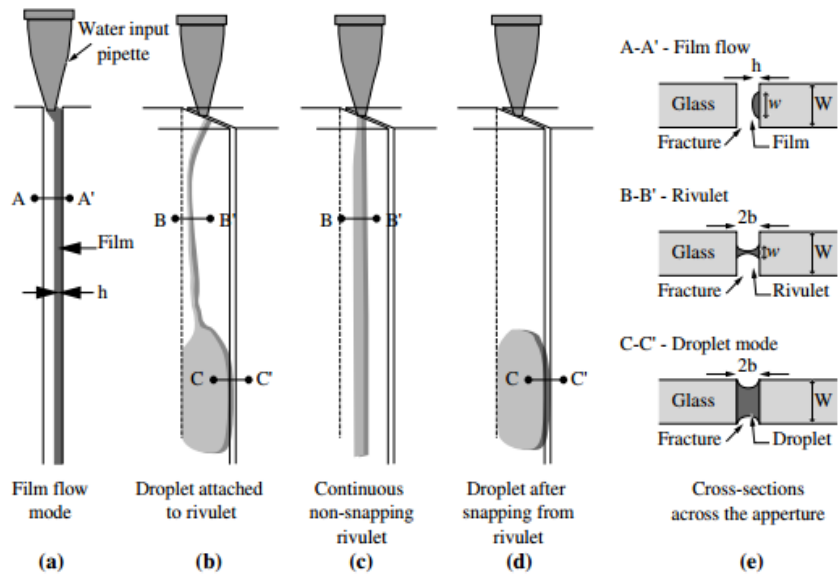


Figure 2.10: (a) Film flow does not span the aperture and only wets one wall at a time, h is the film thickness, w is the film width and W is the width of the fracture plane. (b) Droplet with rivulets span the aperture and are under capillary tension. (c) Non-snapping rivulet spans the aperture and is under capillary tension, width (w) of the rivulet depends on flow rate. (d) Droplet after rivulet has snapped has curved meniscus at the advancing and receding ends. Radius of curvature of menisci in the plane of the fracture wall is much greater than in the plane that spans the aperture. (e) Cross-sectional sketch in the plane of the fracture aperture for (A-A') film, (B-B') rivulet and (C-C') droplets

Source: Dragila and Weisbrod, 2003.

2.4. Joint descriptor

Factors affecting fracture flow, are not limited to the aforementioned, such as fracture interconnectivity, fracture permeability (or those of interest in this study) (aperture and roughness). Figure 2.11 effectively illustrates all the geometric properties affecting flow, indicating: Roughness, aperture, persistence, discontinuity spacing and orientation.

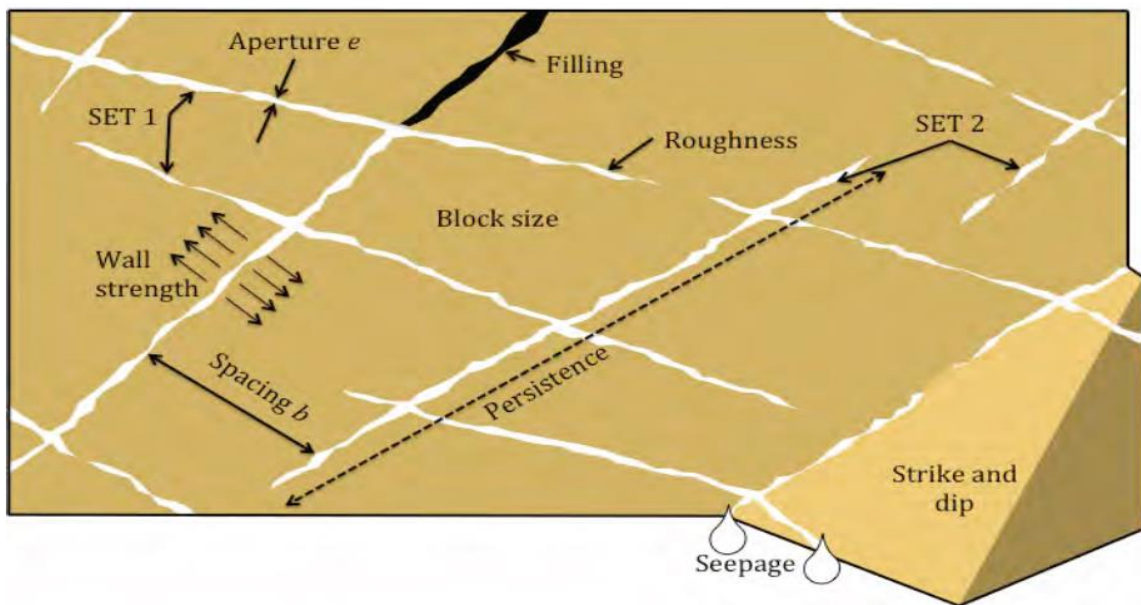


Figure 2.11: Geometric properties of discontinuities to be recorded

Source: Hudson, 1989, in González De Vallejo and Ferrer, 2011.

Literature indicate roughness and aperture as the most important factors, governing fluid flow through a single or a network of fractures (Indraratna & Ranjith, 2011). To exemplify, Qian *et al.* (2007) conducted experiments, considering the influence of scale on fracture permeability. The results indicate that fracture permeability linearly increases with scale and, showing less sensitivity to hydraulic gradients. These observations were attributed to significant 2-D tortuous flows, within rough fractures and varying apertures, opposed to the turbulent or laminar flow regimes.

The close interrelation between the two, raises a level of difficulty in completely focussing on one and ignoring the other. Literature also indicates other factors regarding fracture flow. These mostly relate to fracture void geometry, depicted in Figure 2.12.

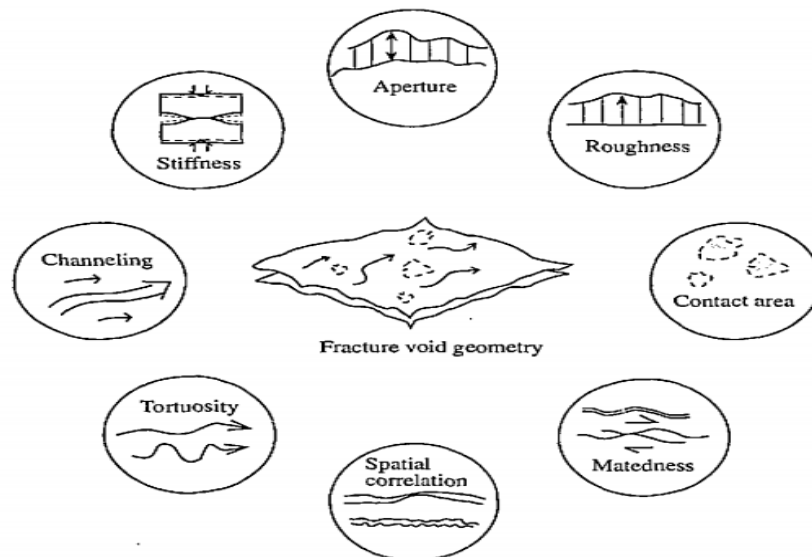


Figure 2.12: Fracture properties determined by fracture void geometry

Source: Hakami, 1995.

2.4.1. Aperture

2.4.1.1 Definition

Aperture refers to the perpendicular distance between neighbouring discontinuity rock walls, with water or air filling the space (no infill material is present). The definition illustrated in Figure 2.13, assumes that fracture surfaces are parallel concerning the x-y plane. Then b - aperture (also denoted as e) is the separation between the two adjacent fracture surfaces in the z-direction at each point. It is denoted that aperture differs from point to point along the fracture length.

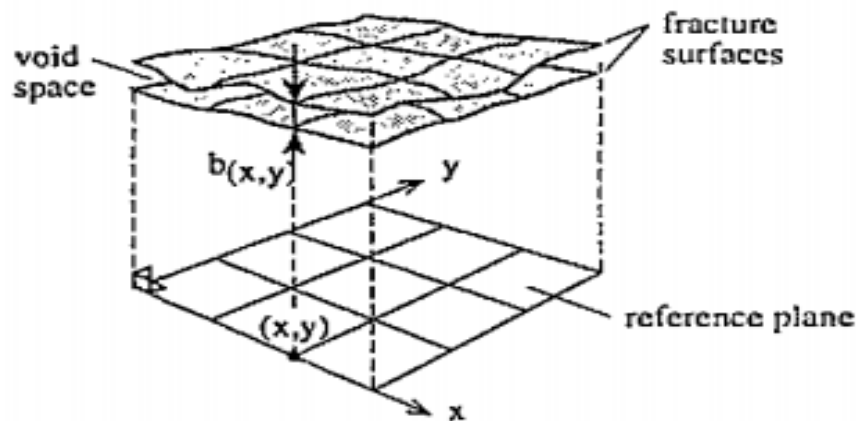


Figure 2.13: Definition of fracture aperture, $b(x,y)$

Source: Hakami, 1995.

Certain definitions consider surface roughness (Figure 2.14) Konzuk and Kueper (2004), affects the manner used to determine aperture.

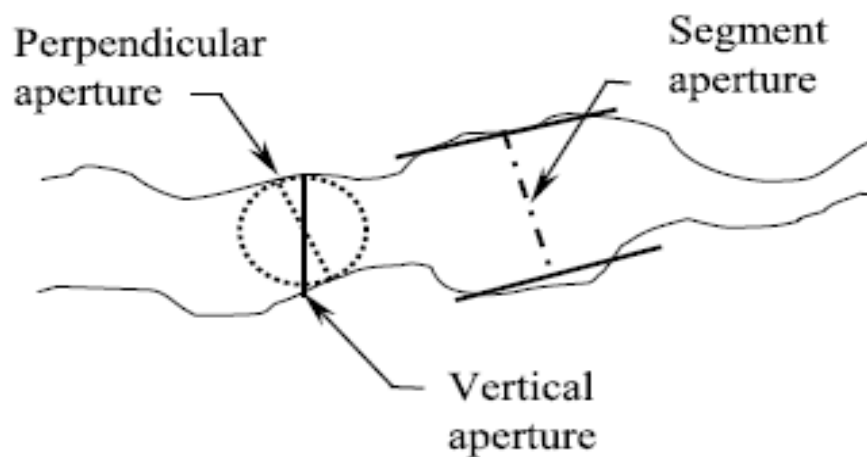


Figure 2.14: Illustration of the various aperture definitions as defined

Source: Konzuk and Kueper, 2004.

Although aperture is larger at the surface, it becomes smaller with depth and occasionally completely closes. This variation in aperture distribution arises due to

change in *in situ* stresses. Subsequently, these stresses are responsible for fracture separation, rotation, shearing and deformation (González De Vallejo & Ferrer, 2011; Hakami, 1995). Similarly, surface roughness or asperities also influence aperture distribution. Aperture implicitly affects the shear-strength of a rock discontinuity, significantly affecting the ability of a fracture to transmit water (Indraratna & Ranjith, 2001; IRSM, 1981; Sahimi, 2011).

Several concepts of aperture exist, relating to the methods used to determine aperture and the application thereof, such as mechanical or hydraulic. These include:

- Equivalent hydraulic aperture (e , a_c), which is derived from the cubic law (Equation 2.3) for flow in an SF (Indraratna and Ranjith, 2001; Qian *et al.*, 2011).

$$K_f = \frac{ge^3}{12vb} \quad \text{Equation 2.3}$$

- Where K_f = fracture conductivity (ms^{-1}), e = hydraulic aperture (m), g = acceleration due to gravity (ms^{-2}), v = kinematic viscosity, which is 1.01×10^{-6} (m^2s^{-1}) for pure water at 20°C , and b is the spacing between fractures (m). From Equation 2.3, hydraulic aperture can be computed by making it subject of the equation and solving everything on the left (Guo & Tian, 2012).
- The hydraulic aperture is frequently compared to the mean or mechanical aperture, with the mechanical aperture normally larger than the hydraulic aperture. This excludes the instance where the residual fracture aperture was attained at high stress; flow deviates from the idealised parallel plates in most natural fractures becoming unsuitable to use (Indraratna & Ranjith, 2001; Liu, 2005). Differences between the two were ascribed to surface roughness and tortuosity (Chen *et al.*, 2000).
- Various terms include ‘equivalent aperture’, introduced to justify the variation in fracture, normally approximated from tracer and hydraulic tests. The terms ‘tracer aperture’ and ‘hydraulic aperture’ are associated with aperture estimation methods used for aperture estimation (Tsang, 1992).
- Mechanical aperture (E , dm , hm , ar), develops due to shear displacement, with highly irregular fracture surfaces. It is vital in describing fracture compliance, such as determining the elastic response of fractured rock. The maximum mechanical

aperture refers to the maximum closure of adjacent fracture planes under normal stress.

- The real (or true) aperture, used interchangeably with mechanical aperture, is normally determined with a maximum level of precision. It therefore allows a detailed reproduction of hydraulic characteristics. It is normally greater than the conducting aperture in uneven fracture surfaces. In smooth and wide fractures, the mechanical aperture and the conducting aperture will be equal. The empirical relation between the mechanical aperture and the conducting aperture is expressed in Equation 2.4 (Lee *et al.*, 1996).

$$a_c = \frac{a_r^2}{JRC^{2.5}}$$

Equation 2.4

- Where a_r and a_c are in μm and JRC is Joint Roughness Coefficient, having a range from 20 (roughest surface) to zero (smoothest surface).

2.4.1.2 Joint aperture measurement techniques

Aperture predominantly controls the volume of water flowing through a rock fracture. Its determination provides a first estimate of possible flow rate, measuring the parameter paramount to create prior judgements on flow rates within a rock fracture. The presence of irregular fracture surfaces, characterised by numerous contact points, poses a challenge in estimating accurate aperture sizes (Indraratna & Ranjith, 2001).

Various methods are developed to estimate aperture sizes, divided into direct and indirect measurements (Figure 2.15). Direct measurements provide the local mechanical aperture at a specific location. They are physically recorded in the field, by observing whether the fracture is likely to open, determining its capacity to conduct water flow. Previously, but still frequently used, is the method to estimate the width of fine apertures, using rulers or 3m measuring tape and feeler gauges. During a discontinuity line survey, smaller apertures can be measured with a vernier calliper (González De Vallejo & Ferrer, 2011; ISRM, 1981).

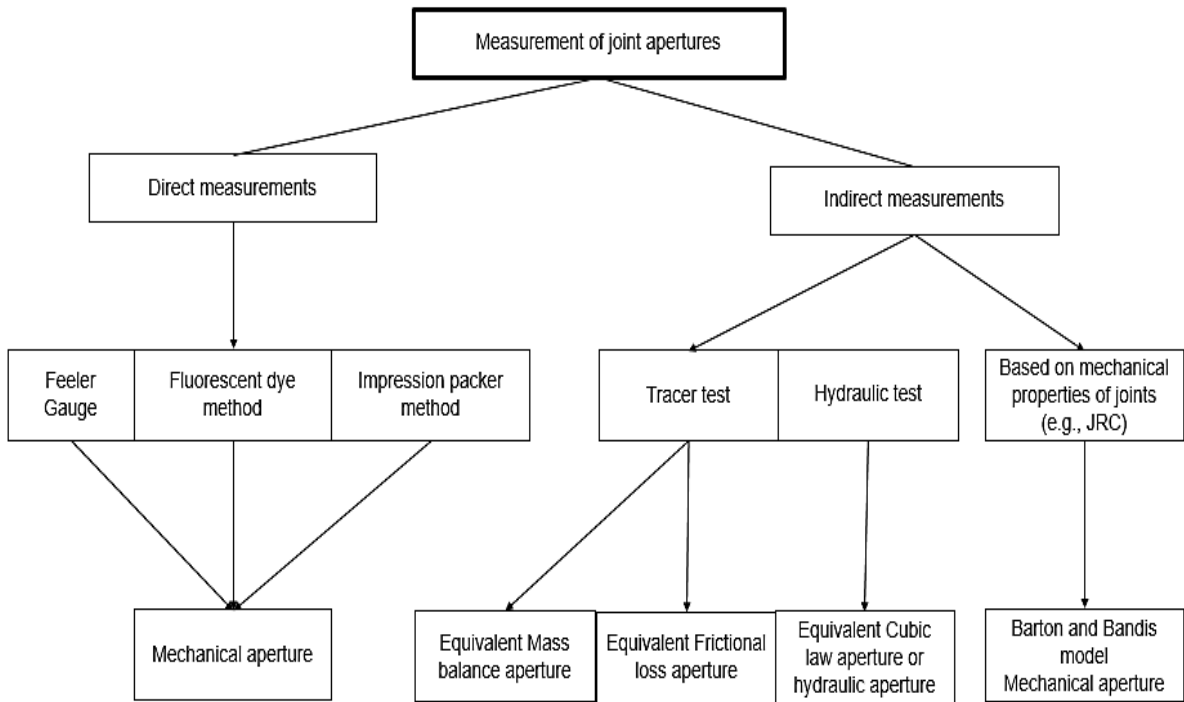


Figure 2.15: Techniques for measuring joint aperture

Source: Indraratna and Ranjith, 2001.

Measurements can further be categorised according to Tables 2.2 and 2.3.

Table 2.2: Classification of joint apertures by its magnitude

Aperture (mm)	Class
< 0.1	Very tight
0.1 - 0.25	Tight
0.25 - 0.5	Partly open
0.5 - 2.5	Open
2.5 - 10.0	Moderately wide
10	Wide

Source: Barton, 1973.

Table 2.3: Description of aperture

Aperture	Description
<0.1mm	Very tight
0.1-0.25mm	Tight
0.25-0.5mm	Partly open
0.5-2.5mm	Open
2.5-10mm	Moderately wide
>10mm	Wide
1-10 cm	Very wide
10-100 cm	Extremely wide
>1 m	Cavernous

Source: ISRM, 1981.

Figure 2.16 indicates an early classification of the various aperture measurement techniques grouped according measurement procedures: (I) Measures the topography of two fracture surfaces forming the void space. The aperture is defined as the space between the surfaces. Procedure (II) is to inject resin into fracture filling the void space. The specimen with the fracture is sliced; the aperture is subsequently

measured as the resin thickness along the fracture on each slice. The third procedure (III) is to create a copy of the void between the fracture surfaces.

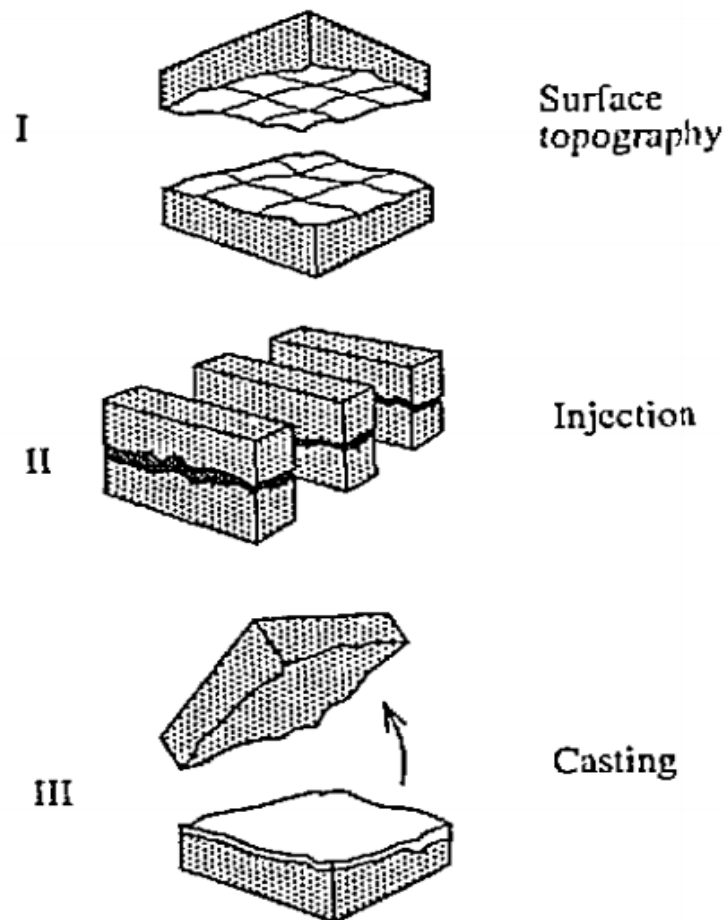


Figure 2.16: Various approaches to measure fracture void geometry

Source: Hakami, 1995.

Hakami and Larsson (1996) used fluorescent epoxy resin of a medium grained granite of Aspo Hard Rock lab, from South-Eastern Sweden. Measurements were obtained, using a stereomicroscope, directly connected to an image analysis system (Figure 2.17). Adding or using image analysis increases the level of accuracy, as details can be recorded meticulously. An added advantage is the simultaneous measurement of surface roughness; the fracture is undisturbed in the process (Konzuk & Kueper, 2004).

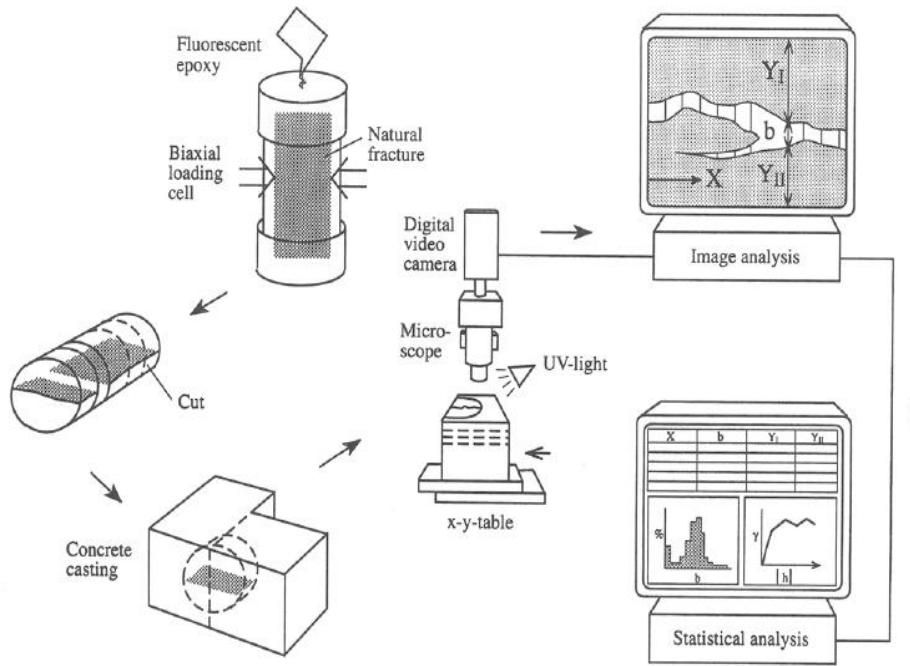


Figure 2.17: Aperture measurement technique

Source: Hakami and Larsson, 1996.

Indirect measurements estimate fracture apertures through either mechanical properties of discontinuities, or by fluid flow measurements through discontinuities (Indraratna & Ranjith, 2001). Examples of indirect measurements, include the measurements of mechanical aperture, based on derivation of empirical approaches including Joint Compressive Strength (JCS) or JRC (Bandis *et al.*, 1983; Barton *et al.*, 1985). Based on the Schmidt Hammer rebound number, an empirical relationship (Equation 2.5) determines the JCS (Indraratna & Ranjith, 2001).

$$\log_{10}(\text{JCS}) = 0.0008\gamma R + 1.01 \quad \text{Equation 2.5}$$

Where γ = unit weight of rock (kN/m^3) and R = rebound number

Further examples of indirect techniques, estimating the hydraulic aperture based on fluid flow through a rock mass, include: (a) laboratory steady-state flow measurement under triaxial test conditions for a specific confining pressure, axial stress and inlet

fluid pressure. The hydraulic aperture, under steady-state flow rates, is calculated, using Darcy's law and (b) through use of *in situ* tests (borehole pumping or tracer tests) (Indraratna & Ranjith, 2001).

2.4.1.3 Effects of joint aperture on fracture flow

According to Guo and Tian (2012), fracture surfaces frequently occur as a result of tensile, shear and compressor-shear stresses, or external stresses. Consequently, this leads to suitable mating relationships and well distributed apertures between two adjacent fracture surfaces.

If there are any morphological fracture surface changes, because of physio-chemical solutions or if their relative positions changed because of natural geological movement processes and fluid pressure changes, the two surfaces will lose their mating relation and uniform distribution. Initial aperture distribution, controlled by surface roughness, conditions the surface contact area and its generating order.

Defining surface contact area is a challenging task, because of a lack of definite contact between contact and non-contact area points, at a macro- and microscopic level (Hakami, 1995; Indraratna & Ranjith, 2001). The influence of aperture on fracture flow is limited to external stresses and fluid pressure, conditioning the existence of variable apertures (Figure 2.18).

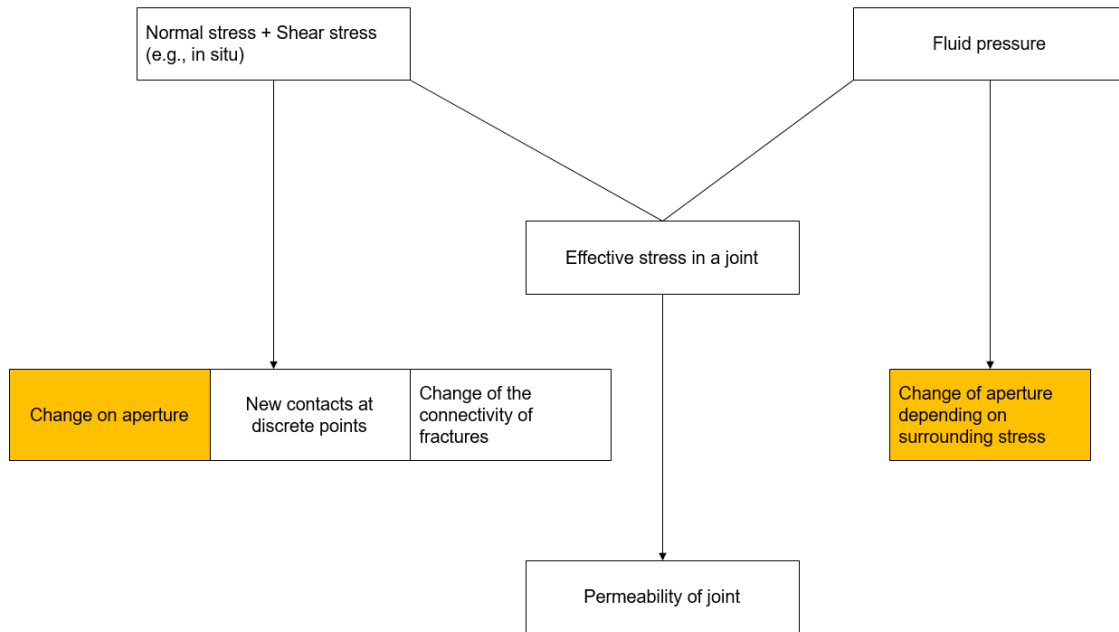


Figure 2.18: Effect of stress on a single rock

Source: Indraratna and Ranjith, 2000.

Stress within rock mass results from self-weight and externally applied forces, such as fluid pressure and seismic loading. The resulting effective stress, acting on a discontinuity comprises a fluid pressure component and a normal and shear component, influencing much of the variable fracture mechanical behaviour. Depending on the magnitude and orientation of stress (Figure 2.19), applied stress determines: Whether the fracture dilates or closes, the creation of new contact points, shearing of asperities depending on surface geometry, the magnitude of normal and shear-strength and rock deformability. Subsequently this leads to variable apertures along the fracture length (Indraratna *et al.*, 1999; Indraratna & Ranjith, 2001).

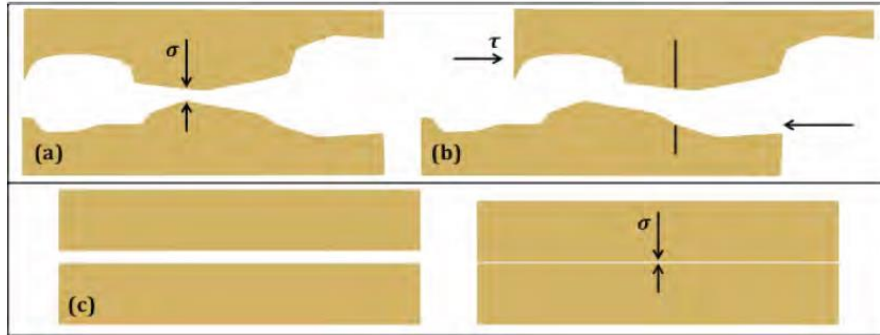


Figure 2.19: a) Normal stress (b) Shear stress on the aperture of a rough fracture (c) the influence of stress on a smooth fracture

Source: Indraratna and Ranjith, 2001.

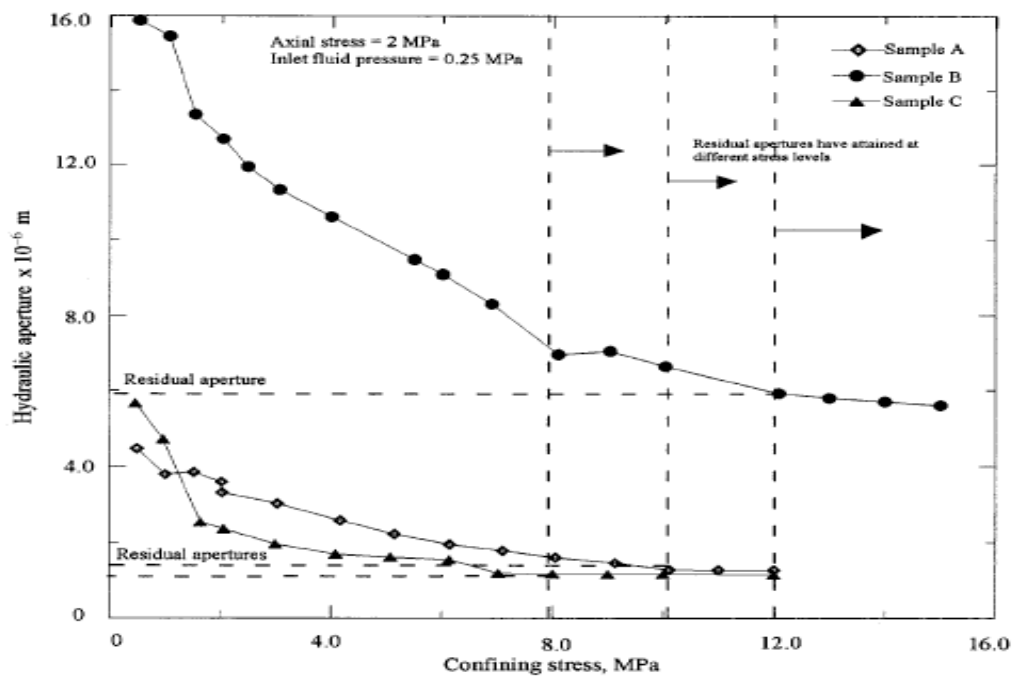


Figure 2.20: Residual apertures for different granitic rock samples with single fracture

Source: Indraratna *et al.*, 1999.

It is necessary to apply sufficiently stress during loading, to attain a residual aperture. Should this not be the case, flow rate will be invariable upon unloading. Conversely, should a residual aperture be attained, the unloading cycle would result in varying flow rates. As depicted in Figure 2.21, flow rate decreases considerably with an increase in confining stresses for the initial loading cycle. Beyond 10MPa, no further decrease in flow rate is observable. The second and third loading and unloading cycle, have an insignificant contribution on flow rate changes. Once a residual aperture is reached, any further dilation and compression is insignificant. As a result, decreased flow conductivity prevails, once the joints are loaded past a critical stress value (Indraratna *et al*, 1999).

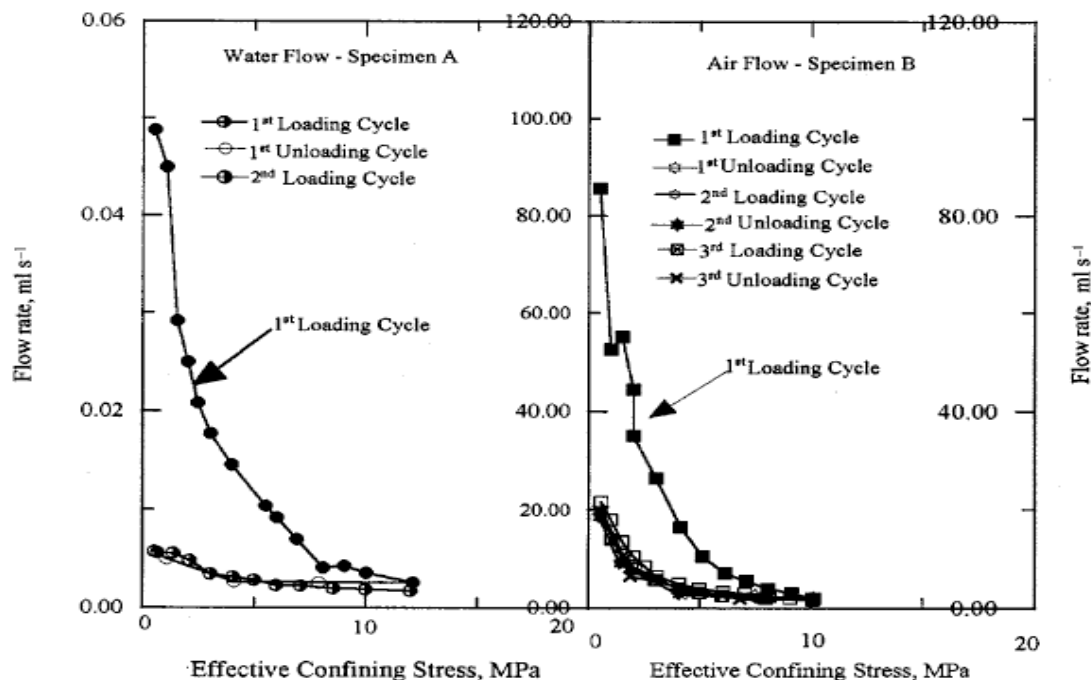


Figure 2.21: Effects of loading and unloading on flow characteristics of jointed rock

Source: Indraratna *et al.*, 1999.

Stress has a directional component, determining the relative permeability of varying fractures in rock mass. Fractures arranged parallel to the maximum stress are likely to be open, whilst those arranged perpendicular are probably closed. Any increment

in compressional stress with depth, results in smaller apertures near surface irregularities and larger between fracture openings (Azeemuddin *et al.*, 1995, Read *et al.*, 1989; Singhal & Gupta, 2010).

Stiffness or “special fracture stiffness” is a term used to express the deformability of rock. It is similarly presumed to condition aperture variability. For instance, little or no variability exists when fracture stiffness is sufficiently high, indicating a significantly low normal stress, whilst an increment in variability is likely to occur when the frequency of aperture distribution is scattered or when a large contact area is present. This will cause several main conduits. Subsequently, this will simplify fracture deformation. Similarly, when frequency of aperture distribution is concerted, fracture susceptibility to deformation, increases. In the aforementioned scenario, normal stress has a significant effect on fracture flow. In the latter incidence, little effect exists (Guo & Tian, 2012; Pyrak-Nolte *et al.*, 1988).

Pyrak-Nolte and Morris (2000) established the following relationship, illustrated in Figure 2.22. Fluid flow and fracture specific stiffness depend on the number and spatial distribution of contact points and aperture distribution. This allows for the assumption that fluid flow and specific stiffness could be related indirectly.

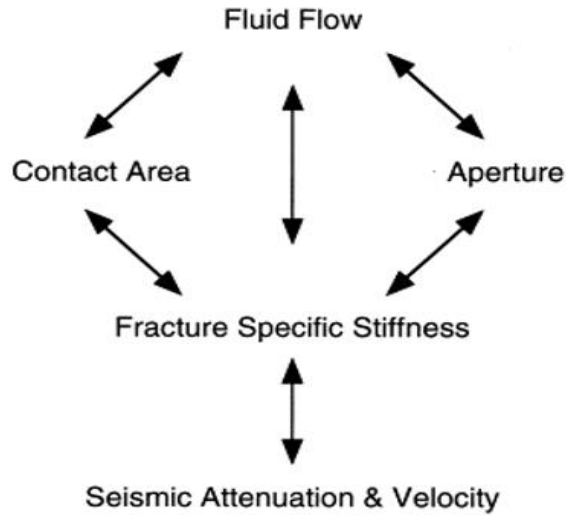


Figure 2.22: Fracture specific stiffness and fluid flow through a fracture are implicitly related through the geometry of the fracture

Source: Pyrak-Nolte, 1996; Pyrak-Nolte and Morris, 2000, adapted from Pyrak-Nolte *et al.*, 1997.

Using 13 samples, Pyrak-Nolte and Morris (2000) numerically examined the relationship between fluid flow and fracture specific stiffness of an SF subjected to normal stress, using spatially correlated and uncorrelated aperture distributions. Although flow rates for each sample (Figure 2.23), demonstrate a decrease with an increase in normal stress, variations exist that can be linked to fracture geometry and the response of each sample under stress.

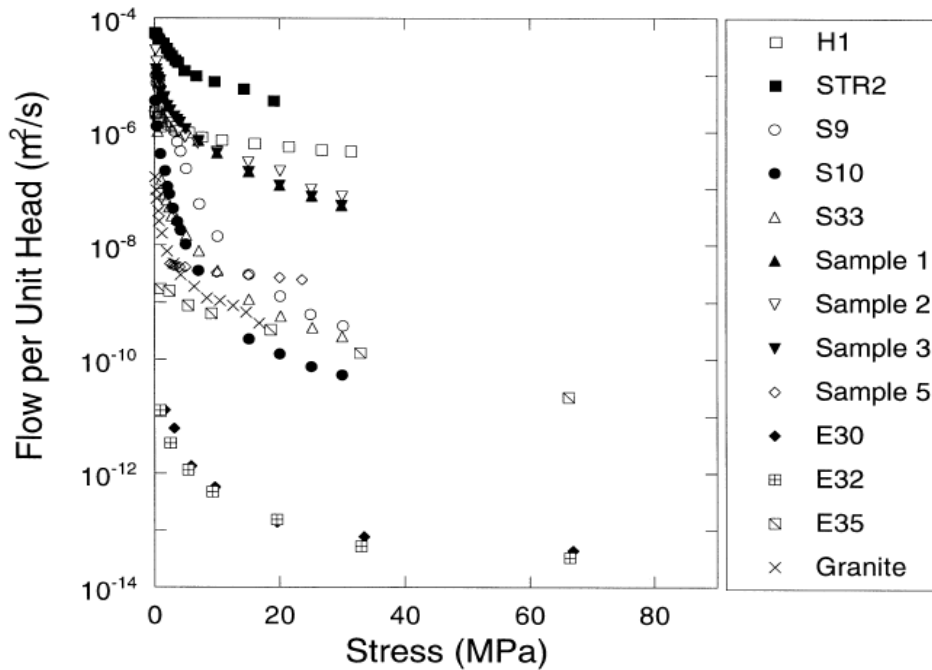


Figure 2.23: Flow per unit head as a function of normal stress for thirteen different samples, each containing a single fracture

Pyrak-Nolte and Morris, 2000.

Two classes of fracture stiffness-fluid flow relationships are established from the results. Firstly, fluid flow in fractures with spatially uncorrelated aperture distributions displayed a weak dependence on fracture specific stiffness. Although an increase in stress results in an increase in stiffness, the flow volume is insignificantly reduced. These fractures develop several connected pathways throughout the sample surface, promoting flow with uniformly distributed contact points. Second, spatially correlated apertures on the other end, develop either one or two pathways, with the contact area limited to certain regions of the fracture. An increase in normal stress would result in a rapid decrease in fluid flow (Pyrak-Nolte & Morris, 2000).

2.4.2. Roughness (Asperities)

2.4.2.1 Definition

Indraratna and Ranjith (2001) define roughness as the surface waviness and unevenness on a discontinuity, relative to its mean plane (Figure 2.24). Surface waviness refers to large-scale undulations. Unevenness refers to small-scale undulations.

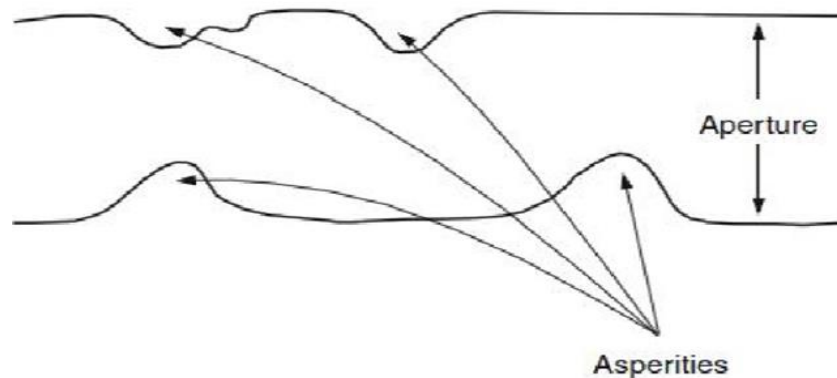


Figure 2.24: Asperities in fracture walls

Singhal and Gupta, 2010.

Table 2.4 and Figure 2.25 illustrate the various scales of roughness.

Table 2.4: Roughness scale

Scale	Order of roughness	Description of surface
Decimetric and metric scale	First order or large-scale undulation	Planar, undulating surface
Millimetric or centimetric	Second order or small-scale	Slickensides, smooth or rough surfaces

Source: Adapted from Barton and Choubey, 1977.

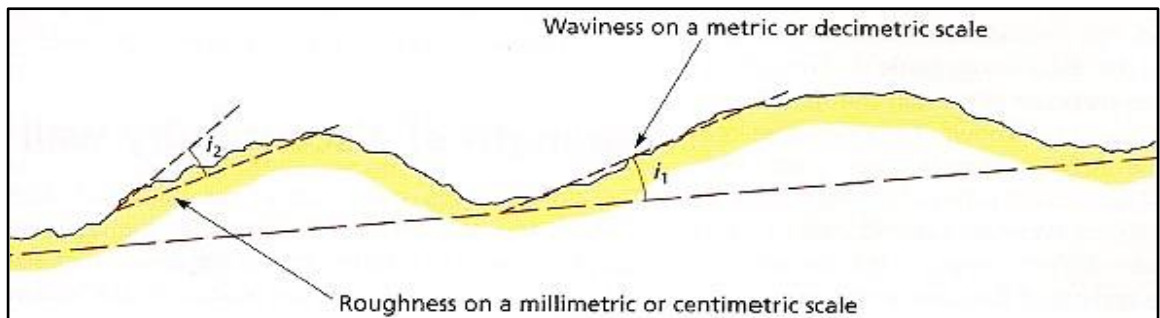


Figure 2.25: Roughness of a discontinuity surface

Source: Barton, 1973; Hoek and Bray, 1981.

Surface roughness can be further characterised by degree fluctuation and fluctuation difference. The former is frequently represented by a fluctuation angle. The latter refers to the perpendicular distance between wave crest and trough of a fracture surface (Guo & Tian, 2012).

Figure 2.26 depicts an additional classification of roughness; micro- and macro-roughness respectively refer to minor variations on fracture surface and large variations on flow conduit. If the aperture is relatively large, micro-roughness has little effect on flow, whilst macro-roughness influences flow through altering flow conduits (Guo & Tian, 2012).

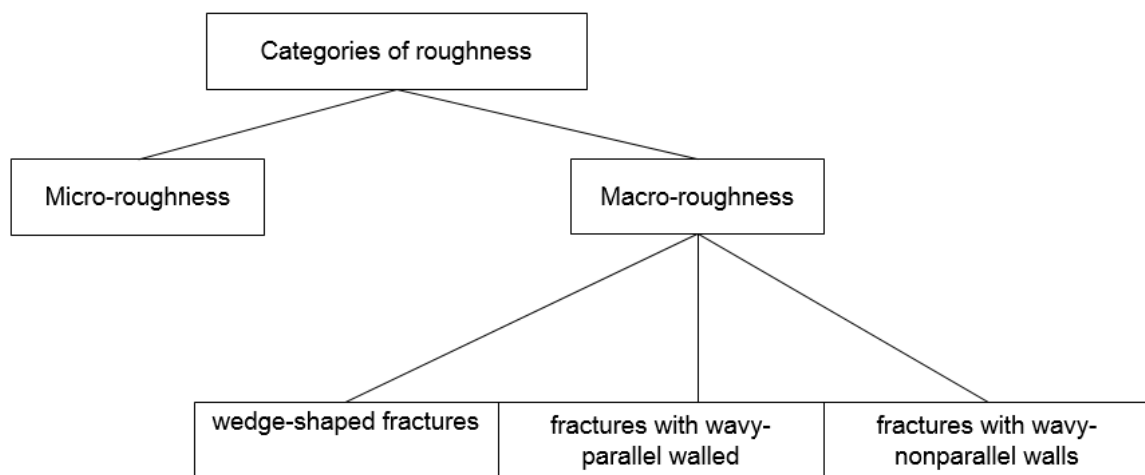


Figure 2.26: Categories of roughness

Source: Modified from Guo and Tian, 2012.

2.4.2.2 Measurement and characterisation of joint roughness

Numerous methods exist, measuring and describing roughness in the field. Their selection depends on the level of accuracy, scale of measurement required and the outcrop accessibility. A well-known application of these measurements, is to predict the shear-strength behaviour rock mass. From a hydrological viewpoint, the primary

aim of describing discontinuity surface roughness, is to formulate correlations with aperture, channelling and tortuosity in fracture flow (Guo & Tian, 2012).

Characterisation methods comprise the use of descriptive methods, such as: The standard roughness profile (also known as the JRC representation method), the asperity height and fracture dimension representation method (IRSM, 1981).

The JRC method is a simple and quick method where a chart, exemplified by Figure 2.27, with various roughness diagrams is used to estimate roughness through matching the chart and the observed surface profile (IRSM, 1981).

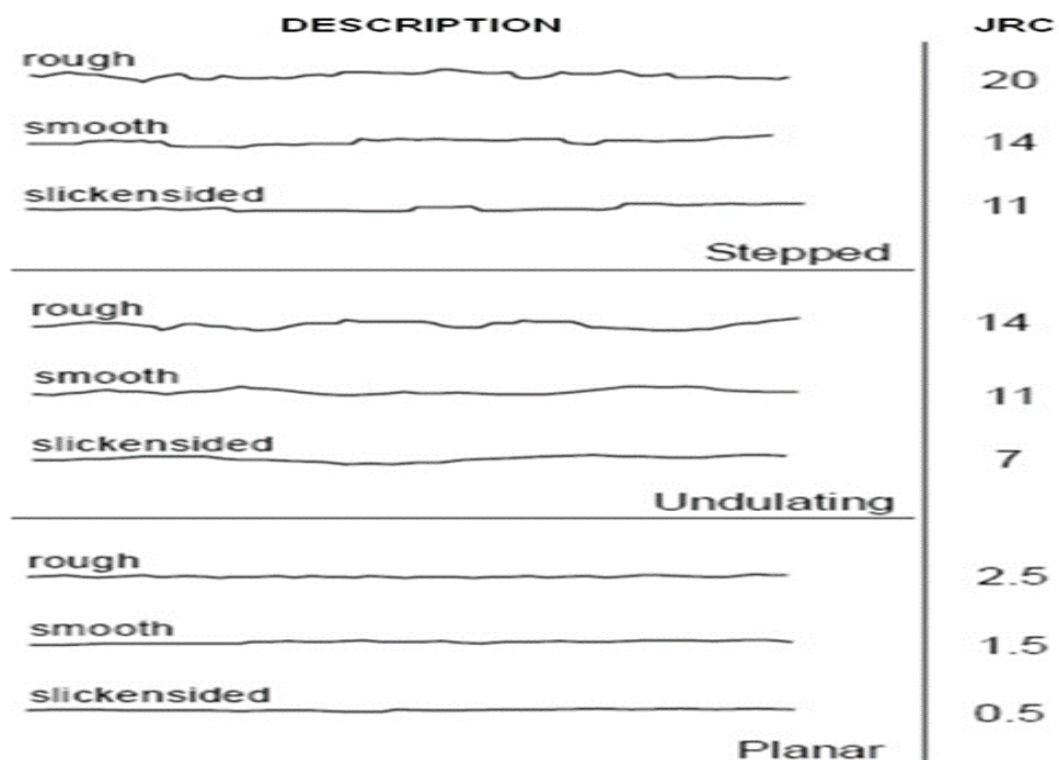


Figure 2.27: Roughness profile

Source: IRSM, 1981.

The asperity height method describes fracture roughness through an asperity height function $h(x,y)$ and the probability density function by $n(h)$. The method can precisely determine the asperity height of each measuring point. The method is only suitable to determine fracture surface topography that cannot be incorporated in the engineering practice (Guo & Tian, 2012).

The fracture dimension method was established during the conception of the fractal geometry theory. The dimension of a smooth fracture is two-dimensional, whereas, a rough fracture is almost three-dimensional. The method is mostly used to describe roughness of a fracture on a single straight line, and not the roughness of an entire fracture surface (Guo & Tian, 2012).

Additional measuring techniques, include using linear profiles and plate methods. Both indicate numerical measurements of roughness. Linear profiles are used when the direction of potential sliding is known. Measurements are captured, parallel to the direction where a straight edge, closely resembling the maximum roughness amplitude (ra), where a 10m wire is placed above the discontinuity plane, parallel to the direction of potential sliding. Similarly, the technique can be used to record the maximum amplitude (ra) for a measured profile length (L) as indicated in Figure 2.29 (Barton, 1982). The distance measured is conditioned by the roughness scale (González De Vallejo & Ferrer, 2011).

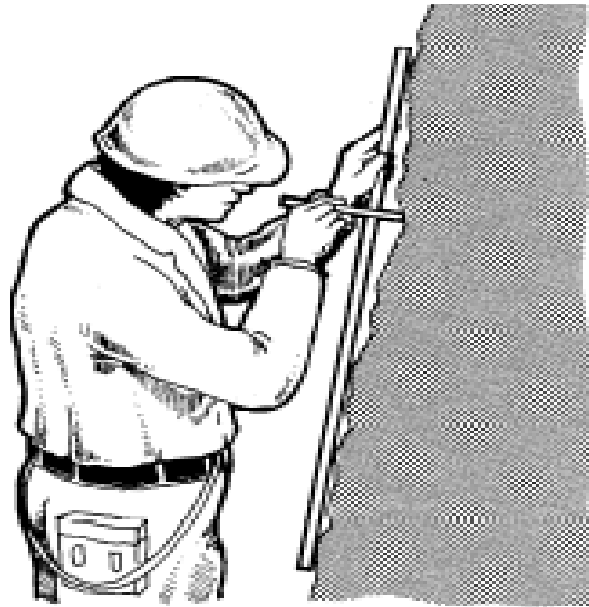


Figure 2.28: Example of straight edge method used to measure the waviness of a rock discontinuity

Source: Milne *et al.*, 1992, adapted from Tatone, 2009.

At 100mm scale:

$$JRC = 400 \frac{a}{L}$$

Equation 2.6

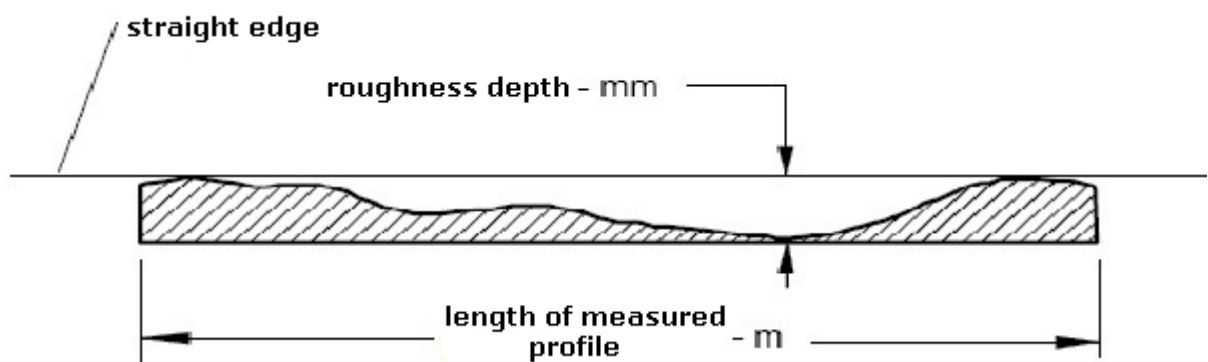


Figure 2.29: Measured profile used to estimate JRC value

Source: Barton and Choubey 1977.

The plate method (Figure 2.30) measures roughness angles of discontinuity planes 3-D, instead of two. It is particularly used when the direction of potential movement is unknown. The results provide localised variations in the discontinuity surface concerning the general dip. A series of plates of various diameters are used, depending on the scale of work. These are placed over various areas of the discontinuity. The strike and dip of the plate are measured with a geological compass.

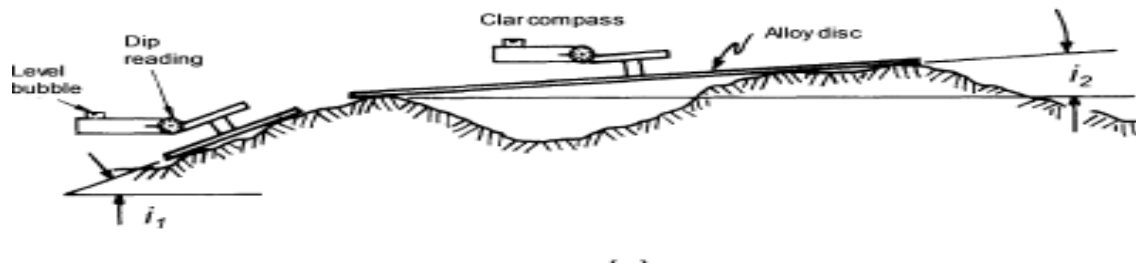


Figure 2.30: Measurement of local surface orientation with circular discs of varying sizes, fixed to clar-type compass

Source: ISRM, 1978, adapted from Tatone, 2009.

If JRC values cannot be directly obtained from the roughness profiles, they can be determined from Figure 0.31. The JRC is indicated as a function of roughness depth and length of profile (Barton & Choubey, 1977).

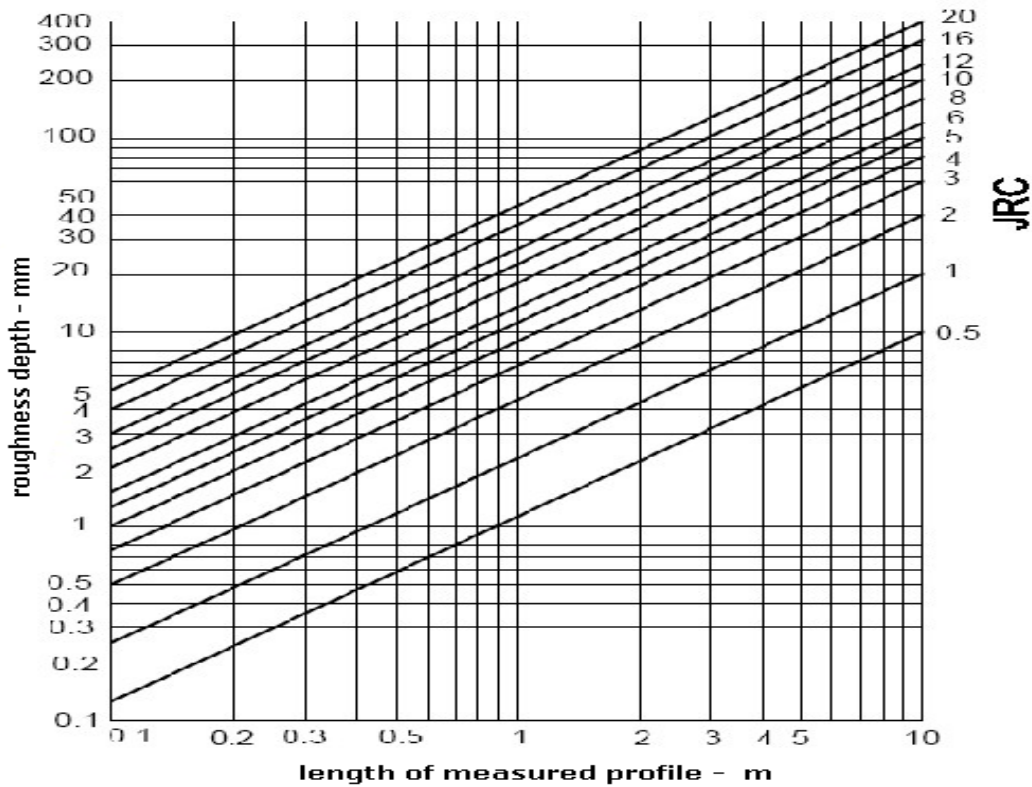


Figure 2.31: Graph used to determine JRC value

Source: Barton and Choubey, 1977.

Additional methods, include calibration methods, such as hydraulic and mechanical joint apertures. Theoretically, these are sound, though their practical applications are limited (Indraratna & Ranjith, 2001).

If critical surfaces are inaccessible, discontinuity surfaces can be described concerning their average planes, using photogrammetric methods. It is a mapping technique, using photogrammetry to determine the coordinates of a minimum of four points on each visible discontinuity plane, determining the orientation of the specified plane. It is normally used when the orientation of a large volume of discontinuities needs to be determined. The data allow, calculating contour maps or profiles of the surface roughness. It is recommended that profiles should be calculated for the direction of the potential sliding (ISRM, 1981).

In the event where time limitations prevent using the above roughness measuring techniques, roughness description will be limited to descriptive terms, based on the observation of two scales, indicating small-scale and intermediate scale. Table 2.5 provides the terms that can be used in this instance.

Table 2.5: Description of roughness

Class	Description
I	Rough or irregular, stepped
II	Smooth, stepped
III	Slickensided, stepped
IV	Rough or irregular, undulating
V	Smooth, undulating
VI	Slickensides, undulating
VII	Rough or irregular, planar
VIII	Smooth, planar
IX	Slickensides, planar

Source: ISRM, 1978c.

The use, authenticity and reliability of the aforementioned techniques are questioned. Arising questions include, whether such idealised profiles can behave as natural joints. Should they not, how accurate will the subsequent analysis be? (Indraratna and Ranjith, 2001).

The aforementioned became a basis for developing “Mapping Surface Profile”. In the context of mining and rock engineering as surface roughness influences fluid flow through discontinuities, jointed slopes and mine roofs. Modelling joint techniques assume one or more of the following options (Indraratna & Ranjith, 2001):

- Graphical representation of the surface profile.
- Mathematical representation of the mapped surface profile.
- Statistical features.

Various techniques were previously used to obtain the graphical representation of surface profiles at macro- and microscopic levels. Based on the principle modes of measurement options, methods are divided into four categories: (a) Mechanical, (b) hydraulic, (c) optical and (d) laser techniques (Figure 2.32) (Indraratna and Ranjith, 2001).

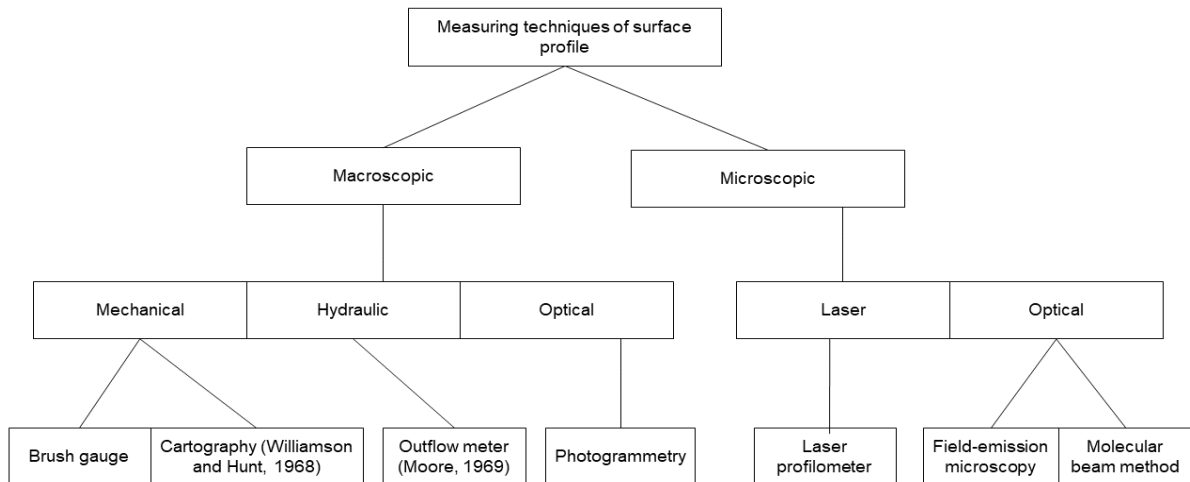


Figure 2.32: Available profilometers based on modes of measurement

Source: Modified from Indraratna and Ranjith, 2001.

2.4.3. Effects of roughness on fracture flow

Roughness increases the path length of fluid flow movement between any two points, leading into increased fluid flow resistance, thus reducing fracture conductivity. A more pronounced effect occurs in particularly smaller aperture fractures, translating to a greater resistance on fluid flow (Develi & Babadagli, 2015; Li *et al.*, 2008; Oron & Berkowitz, 1998; Zimmerman & Yeo, 2000).

Research focusses on the validity of the “cubic law” (also referred to as Local Cubic Law - LCL), applied to natural fractures. It reveals that it immensely varies regarding the surface morphology, void geometry and aperture. Its simplicity resulted in its widespread use in experimental fracture flow studies. It therefore considered the principle law that governs fluid flow in SFs (Brown, 1987; Indraratna & Ranjith, 2001; Lomize, 1951; Louis, 1969; Qian *et al.*, 2011).

The law assumes an ideal SF that is parallel and smooth. The assumption is inadequate as it does not reflect the natural fracture surface environment, characterised by irregularities and random contact points (Figure 2.33). The law is further limited by its application to laminar flow type conditions only (also referred to as Darcian flow).

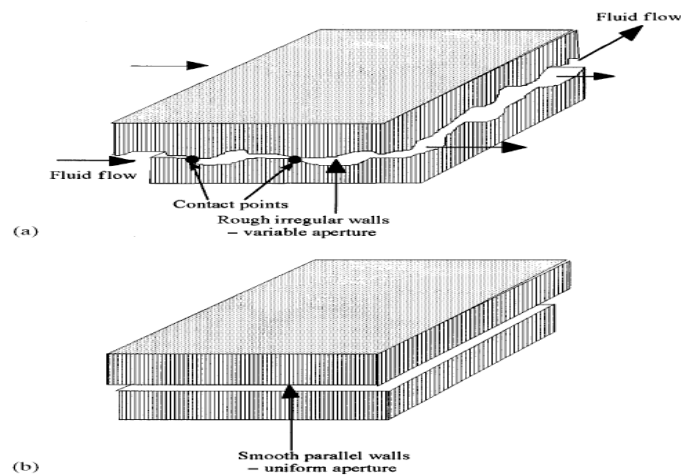


Figure 2.33: Flow through a single fracture: (a) Natural fracture; (b) Idealised fracture

Source: Indrarantna *et al.* 1999.

Forchheimer (1901, cited in Ranjith & Viete, 2011) concurs with these observations. They noticed that as flow velocity increases, additional influences are introduced, such as frictional losses, due to increasing turbulence in flow- inertial effects. These become considerably significant with an increment in permeability, flow velocity and flow pressure conditions. The concern is raised in assuming cubic law in non-Darcian flow conditions with the lack of considering influences of inertial effects. Should these be considered (Qian *et al.*, 2011), they would be provided appreciable merits and benefits in hydrology, petroleum, environmental, geotechnical and chemical engineering.

Similarly, Qian *et al.* (2005, 2007, 2011) and Zimmerman and Bodvarsson (1996), demonstrate that the LCL is unsuitable when flow velocity is high or where pronounced fracture roughness is present, leading to greater tortuosity under flow conditions where

they may usually would not be anticipated. This allow for inertial effects at low values of Reynolds (Re) numbers.

Kohl *et al.* (1997) (including Kolditz, 2001 & Berkowitz, 2002) provide evidence of non-Darcian flow in natural rocks in two independent multi-rate flow experiments in the hot dry rock (HDR) test site in France, Scoutt.

In their SF, experimental investigation below various roughness and aperture conditions, Qian *et al.* (2011) established that the relationship between linear velocity and hydraulic gradient, indicated a non-Darcian turbulent flow, although the Reynolds number was low. Similarly, for the same hydraulic gradient, the linear velocity is directly proportional to aperture at a constant surface roughness. When the surface roughness increases, the linear velocity decreases, as the aperture is kept constant.

Table 2.6 summaries the conditions under which the law is either valid or invalid (Ge, 1997; Konzuk & Keuper, 2004; Méheust & Schmittbuhl, 2001).

Table 2.6: Validity of cubic law to different types of fractures under varying stress conditions

Fracture distribution	Normal conditions	Increased stress
Smooth parallel joint	Valid	Reduced aperture; still valid
Open parallel joint	Valid with some deviation	Creates contact points; invalid
Joint with contact points	Invalid	More contcat point or gouge deposition; invalid

Source: Indraratna and Ranjith, 2001, cited in Dippenaar *et al.* 2015.

Deviations are not limited to irregular joint surface roughness conditions, but further include non-uniform aperture, similarly characteristic of natural fracture conditions. For instance, Dimadis *et al.* (2014) realise that the conducting aperture e (equal to the hydraulic aperture b_h) and the induced aperture E_m were not acquiescent except when $E_m = 1000 \mu\text{m}$. Experiments revealed an existence of flow for induced $E_{m1} = 0 \mu\text{m}$, when the fracture is closed under gravity. The calculated hydraulic aperture was $b_h = 122 \mu\text{m}$, proving to be discordant with the closed fracture. This was indicative of the existence of void spaces, amid the two fracture walls, due to roughness. As a consequence, the cubic law is invalid for apertures less than $1000 \mu\text{m}$, as illustrated in Figure 2.34. The conducting aperture e is identical to the real aperture E .

Table 2.7: Estimated real apertures and induced apertures

Induced aperture E_{mi} (μm)	0	200	250	500	750	1000
Back calculated b_h (equal to e) (μm)	122	250	290	490	700	992
Real Aperture E (μm)	363	521	562	730	875	1000

Source: Dimadis *et al.* 2014.

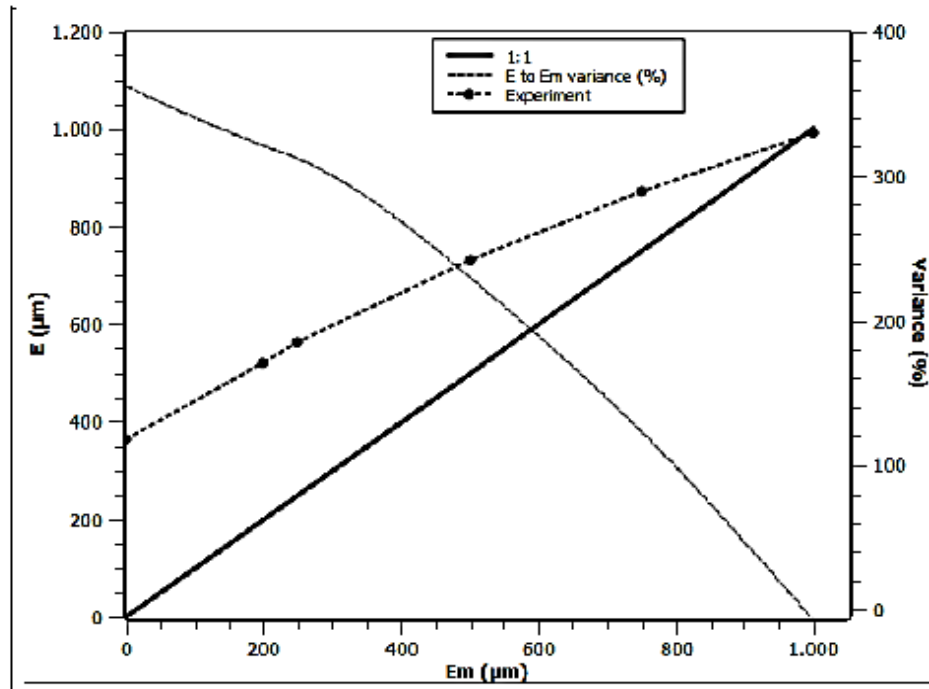


Figure 2.34: Real aperture E to Induced aperture Em variation

Dimadis *et al.* 2014.

To overcome the limitations posed by the cubic law, numerous attempts were made to modify and improve the equation, such as modifying the definition of aperture, incorporating additional information, indicating contact area (Walsh, 1981 cited in Konzuk & Kueper, 2004), tortuosity and or velocity variations (Walsh & Brace, 1984 cited in Konzuk & Kueper, 2004; Ge, 1997), and or losses due to surface roughness (Lomize, 1951; Witherspoon *et al.*, 1980 cited in Konzuk & Kueper, 2004).

The Reynolds (Re) number (Equation 2.7) were used to calculate the influence of inertial effects in a flow system (Fitts, 2002; Ranjith & Indraratna, 2001; Reynold, 1883) Bear (1979), reported that flow becomes non-Darcian for Re greater than one. A transitional flow regime that might show characteristics of Darcian behaviour, governs for Re between one and ten. The number is predominantly used to differentiate between laminar and turbulent (non-Darcian) flow, based on the geometry of flowing system and fluid properties:

$$Re = \frac{VD_h}{\nu}$$

Equation

2.7

Where V = average velocity, D_h is the hydraulic diameter of a fracture of aperture e and ν is the kinematic viscosity of permeant.

According to Zimmerman *et al.* (2004), an increase in Reynolds number results in three distinct flow regimes in porous media. Similarly, assuming the same occurs in fracture flow, these are:

- Small Re values, flow is described by a linear relationship between flow rate and pressure drop (Darcy's law).
- Slightly higher values of Re , indicates a transitional regime where an additional pressure drop occurs, equivalent to the cube of flowrate (referred to as "weak inertia regime").
- Higher Re values, an additional non-Darcy pressure drop is proportional to the square of flowrate - also known as "strong inertia regime".

Surface roughness results in contact areas between fracture walls, correspondingly variable apertures, generating flow channelling through active fracture pathways. Field evidence suggests that flow is predominantly focussed along preferential flow paths, covering < 25% of the fracture plane. At high normal stress levels, flow coverage becomes even less. There is a nominal aperture (residual aperture), corresponding to this minimum flow, characterising every rough joint (Weisbrod *et al.*, 2000).

Thompson and Brown (1991) illustrated that directional characteristics need to be considered and could perform a more determining part than the degree of roughness. According to their study, roughness oriented parallel to the primary direction of flow, results in enhanced flow and solute transport rates with the effect more noticeable in increased surface contact areas. Roughness oriented diagonal to flow, prevents flow rates, resulting in deferrals in flow movement through fracture.

Concerning the reliance of path tortuosity on fracture roughness characteristics, Tsang's (1984) calculations revealed the presence of more small apertures in the aperture distribution, leading to an increased effect of tortuosity. In addition, fracture surfaces with contact areas above 30%, result in invariably larger aperture distributions than the smaller apertures. The effect of fracture roughness and flow path tortuosity, reduces fluid flow rate from the value predicted by the parallel-plate with three or more orders of magnitude.

In a study by Boutt *et al.* (2006), the authors describe the effects of the latter on flow rate, stating that surface roughness generates a geometric boundary, determining advancement and fluid flow response. These recirculation zones serve as "trapping zones", thus affecting transport of dissolved and solid materials. In their study, similar instances reveal that an increase in the average aperture, reduces surface roughness effects. A greater influence is expected on fluid flow and transport through tight rough-walled fractures.

Roy and Singh (2015) established a similar occurrence, referred to as "the wall effect". The subsequent diagrams depict some of the results from the research. Figure 2.35 depicts the velocity components in the x- and y- direction, oriented parallel and perpendicular to the fracture respectively. Surface roughness has the least effect on fluid flow occurring parallel to the fractures. It significantly affects fluid flow, occurring perpendicular. From the diagrams, the effects become more pronounced with an increase in JRC.

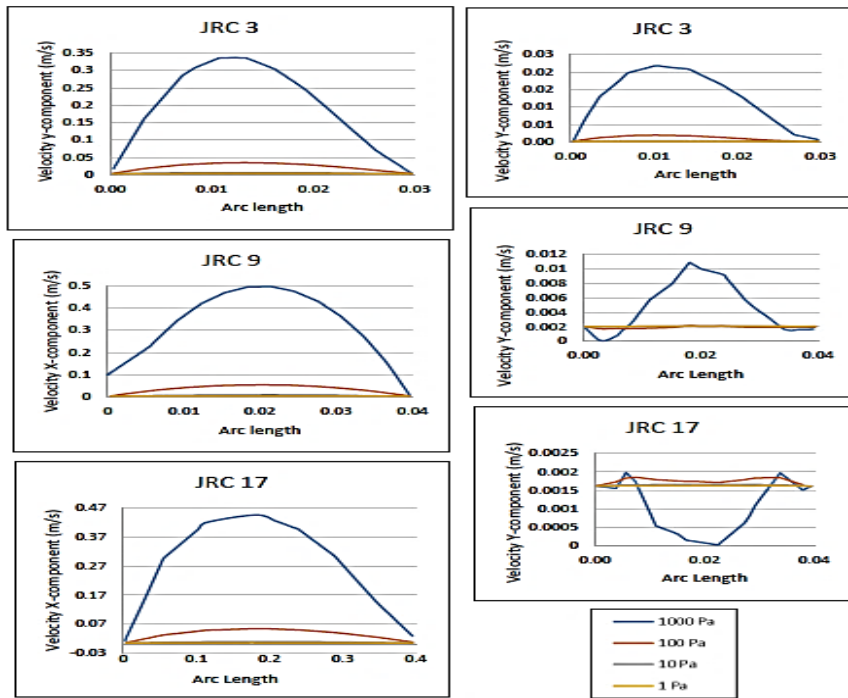


Figure 2.35: X- and Y- velocity components across the fracture aperture

Source: Roy and Singh, 2015.

Figure 2.36 illustrates the shear distribution at various inlet pressures. The figure indicates an increase in inlet pressure results in a strongly asymmetric shear rate distribution, resulting in more turbulent and chaotic flow conditions. This further escalates with an increase in JRC values (Roy & Singh, 2015). Similarly, increased particle transport times with increasing JRC were observed, indicating that particles get confined in non-uniform surfaces. The saddles and undulations on the surface translate to increased fluid flow pathway and consequent increased travel times (Roy & Singh, 2015).

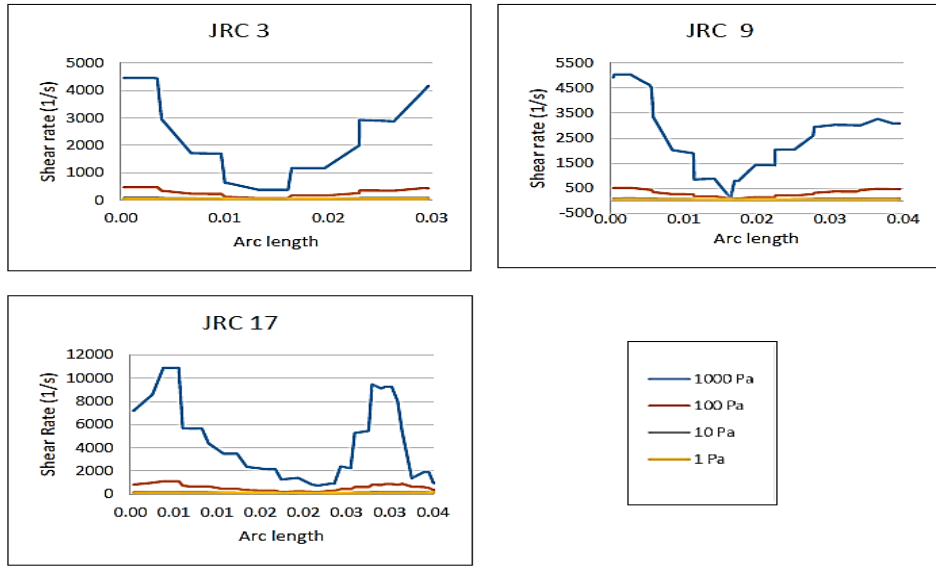


Figure 2.36: Shear rate distribution across the fracture aperture

(Roy and Singh, 2015).

CHAPTER 3 : MATHEMATICAL AND NUMERICAL MODELLING

A judicious understanding of fluid flow in an SF is crucial, prior to examining complex fracture networks. In particular, flow properties through an SF are a basis for researching fluid flow behaviour in jointed rock mass (Guo & Tian, 2012). Research illustrates that flow properties of the most prominent (single) fracture control flow capacity of fractured rock mass (Lomize, 1951; Ranjith, 2000; Ranjith, 2010).

Effective fluid flow behaviour models rely on determining flow properties of an SF, the fracture distribution of rock mass, the aperture distribution of each fracture and the correct prediction of single-phase fluid flow behaviour. Once these are validated for a specific hydrogeological setting, they allow for safe and sustainable engineering solutions that may subsequently be used for studying various hydrogeological settings (Signal & Gupta, 2010). This chapter comprises the various flow modelling techniques examined, further comparing the pros and limitations thereof.

3.1. Mathematical modelling

3.1.1. Navier-Stokes and Reynolds number

Theoretically, flow in SFs is investigated by Navier-Stokes (NS) equations (Equation 3.1) comprising a set of non-linear partial equations. These can efficiently describe the 3-D flow behaviour in an SF (Zimmerman and Bodvarsson, 1994).

$$\rho \frac{\partial v}{\partial t} + \rho v \nabla v = \rho g - \nabla P_T + \mu \nabla^2 v \quad \text{Equation 3.1}$$

Where ρ is fluid density, μ is viscosity of fluid, v is groundwater flow velocity, P_T is total pressure, t is time, and g is the acceleration due to gravity. The term on the left represents the acceleration of a fluid particle. Under the consideration that, at a fixed point in space, fluid particle velocity may vary with time. The second term refers to advective acceleration and accounts for change in fluid particle velocity, even under steady-state conditions, by virtue of advancing to a position at which there is a different velocity. The sum of the two terms denotes the acceleration of a fluid particle

calculated by “following the particle” along its path. The right-hand side of Equation 3.1 denotes forcing terms, representing the applied body force, pressure gradient and viscous forces (Zimmerman & Bodvarsson, 1996).

The equations are preferably used to simulate flow in fractures with ideal geometries. These provide information on pressure and distribution of flow velocity. NS equations are normally too hard to solve, analytically and numerically, particularly in a rough-walled fracture (Brush & Thompson, 2003; Ge, 1997; Guo & Tian, 2012; Zimmerman & Yeo, 2000).

Similarly, the two-dimensional version of the NS equations was used for two-dimensional fractures. These indicated to successfully depict some effects of fluid transport, due to asperities (Sun & Zhao, 2011).

The Stokes equations are an essential subset of NS equations. These are a set of linear partial differential equations where inertial force terms are ignored, making them easier to solve, though still difficult (Guo & Tian, 2012; Zimmerman & Bodvarsson, 1996). Solving the equations comes with a significant burden.

Consequently, NS equations can easily be reduced to the Lubrication or LCL (Local Cubic Law, Equation 3.2), also known as Reynolds (Re) number, to avoid challenges posed by NSE and SE equations (Brown, 1987; Iwai, 1976).

$$Re = \frac{\rho l_v U_i}{\mu} = \frac{p(b)Q}{\mu(b)W} = \frac{\rho Q}{\mu W} \quad \text{Equation 3.2}$$

Where l_v is the characteristic length of the viscous forces and U_i is the characteristic velocity from the inertial forces.

The Reynolds equation is a two-dimensional estimate of Stokes equations for fluid flow occurring through slightly non-parallel plates. The solution thereof yields to a parabolic velocity profile associated with the local head gradient. It is typically used to assess relative strength of inertial to viscose forces, allowing direct incorporation of simple surface features. With simplification though, the effect of roughness and tortuosity on the validity of the cubic law can only be examined after the solution of the Re equation, using various statistical averaging schemes (Brown, 1987; Zimmerman & Bordvarsson, 1991).

For the equation to hold, two conditions must be satisfied. First, the mean value and the variance of aperture must be less than the aperture distribution of a certain length scale. Secondly, fluid flow through the fracture must be steady and velocity must be sufficiently low to ignore inertial forces (Guo & Tian, 2012).

When $Re < 1$, inertial forces have little effect, whereas, more significant effects are expected for Re between 1 and 10. Should Re range between 1 and 100, the direct relation between pressure drop and flow velocity ceases to exist, overestimating conductivity by 100%. When Reynolds number is 333.26-1413.62, non-Darcy flow occurs, contravening the cubic law and LCL (Guo & Tian, 2010).

Caution should be exercised when using the LCL. It does not hold when not fulfilling either of the two conditions yielding the NSE, SE and lubrication equation. This occurs when Re is greater than 10, or the wavelength is less than three times the mean aperture (Lomize, 1951; Louis, 1969).

Brown (1987) calculated velocity gradients in various fractures, using LCL simulations. He proposes that the wall surface roughness length scale must be at least 50 times larger than the σ_u (standard deviation of the upper surface fracture wall) for the LCL to serve as an effective estimate of the Stokes equation. Ignoring the plane velocity, presents an error; the relative roughness is increased in ranges between 10-100% of the NS value (Zimmerman *et al.*, 2004). Variations noted between experimental and numerical results, primarily occur at low velocities as the cubic law does not account

for the existence of rough walls and tortuous flow paths. These are generated because of asperity contacts (Brown, 1987).

Several other laws quantify flow. These depend on laminar, turbulent or transitional flow conditions, including the relative height of the asperities or shape of the depicted roughness. Table 3.1 illustrates that the hydraulic conductivity of any single joint is conditioned by the joint aperture (e) and the joint roughness (ε/D_h). Where ε (sometimes indicated as k) is the height of the asperities or maximum amplitude of the roughness. D_h represents the hydraulic diameter (Louis, 1968; Scesi & Gattinoni, 2007).

Table 3.1: Flow laws concerning water flow in a joint (frequency is equal to 1)

	Condition		Flow Law	Hydraulic conductivity
$\frac{\varepsilon}{D_h} < 0,333$ (<i>superficial roughness</i>)	Laminar	I	$\lambda = \frac{96}{Re}$ (<i>Poiseuille 1839</i>)	$k_i = \frac{e_i^2}{12\nu}$ (<i>Snow 1970</i>)
	Turbulent (smooth walls)	II	$\lambda = 0.316Re^{-\frac{1}{4}}$ (<i>Blasius</i>)	$k_i = \left[\frac{g}{0.079} \left(\frac{2}{\nu} \right)^{1/4} e_i^3 \right]^{4/7}$
	Turbulent (rough walls)	III	$\frac{1}{\sqrt{\lambda}}$ $= -2 \log \frac{\varepsilon}{3.7 D_h}$ (<i>Nikuradse 1930</i>)	$k_i = 4\sqrt{g} \left(\log \frac{3.7}{\frac{\varepsilon}{D_h}} \right) e_i^{1.5}$
$\frac{\varepsilon}{D_h} > 0,333$ (<i>shape roughness</i>)	Inertial	IV	$\lambda = \frac{96}{Re} \left[1 + 8.8 \left(\frac{\varepsilon}{D_h} \right)^{15} \right]$ (<i>Louis 1967</i>)	$k_i = \frac{g e_i^2}{12\nu \left(1 + 8.8 \left(\frac{\varepsilon}{D_h} \right)^{15} \right)}$
	Turbulent	V	$\frac{1}{\sqrt{\lambda}} = -2 \log \frac{\varepsilon}{1.9 D_h}$ (<i>Louis 1967</i>)	$k_i = 4\sqrt{g} \left[\left(\log \frac{1.9}{\varepsilon/D_h} \right) \right] e_i^{1.5}$

Source: Scesi and Gattinoni, 2007.

Each of these laws refers to a specific applicability range.

g Standard gravity acceleration (9.81m/s^2); ν fluid's kinematic viscosity ($10^{-6}\text{ m}^2/\text{s}$); k_i hydraulic conductivity of the n-fracture (m/s); e_i aperture of the n-fracture (m); ε asperity height (m); D_h hydraulic diameter (for discontinuities at a "e" distance: $D_h \equiv 2e$) (m); λ load-loss coefficient; Reynolds number $Re = D_h V_m / \nu$ ($V_m = \text{average velocity}$).

Equations 3.3-3.5 provides additional relationships between relative roughness (ε/D_h), pressure drop coefficient, Re and unit flow for laminar, transitional and turbulent flow. This followed the establishment of a critical Reynold's number (Re_k), for laminar flow type conditions, of 2300, whilst the commencement of turbulent conditions occurs at Re_k of 100 with intensified fracture roughness (Louis, 1968; Wittke, 1990).

$\lambda = f(Re)$	Hydraulically smooth flow	Equation 3.3
-------------------	----------------------------------	---------------------

$\lambda = f\left(Re, \frac{\varepsilon}{D_h}\right)$	Transition flow	Equation 3.4
---	------------------------	---------------------

$\lambda = f\left(\frac{\varepsilon}{D_h}\right)$	Completely rough flow	Equation 3.5
---	------------------------------	---------------------

The algebraic expressions in Table 3.2 construct the subsequent figures, instituting relationships between relative roughness and pressure drop with Reynolds numbers, for the range of identified flow types (Indraratna & Ranjith, 2001).

Table 3.2: The unit flow rate and pressure drop coefficient for a single fracture

	Flow Type	Pressure drop coefficient	Flow rate	Comments
Relative roughness, $k/D_h \leq 0.033$ (Parallel flow)	Laminar	$\lambda = \frac{96}{Re}$ Poiseuille	$q = \frac{g}{12\nu} e^3 J$	Overestimates flow volume Widely used in numerical models
	Turbulent	$\lambda = 0.316 Re^{-0.25}$ Blasius	$q = \left[\frac{g}{0.079} \left(\frac{2}{\nu} \right)^{0.25} e^3 J \right]^{4/7}$	
		$\frac{1}{\sqrt{\lambda}} = -2 \log \frac{\frac{\varepsilon}{D_h}}{3.7}$ Nikuradse	$q = 4\sqrt{g} \left(\log \frac{3.7 D_h}{k} \right) e^3 \sqrt{J}$	Need to know roughness of each joint
Relative roughness, $k/D_h \leq 0.033$ (Non-parallel flow)	Laminar	$\lambda = \frac{96}{Re} \left[1 + 8.8 \left(\frac{\varepsilon}{D_h} \right)^{1.5} \right]$ Louis	$q = \frac{g e^3 J}{12\nu [1 + 8.8 (k/D_h)^{1.5}]}$	Results may be better than flow than flow rate values computed by cubic law, if correct roughness is used.
	Turbulent	$\frac{1}{\sqrt{\lambda}} = -2 \log \frac{\frac{\varepsilon}{D_h}}{1.9}$ Louis	$q = 4\sqrt{g} \left(\log \frac{1.9 D_h}{k} \right) e^{1.5} \sqrt{J}$	Yields low magnitude of flow rate than cubic law

Source: Thiel, 1989.

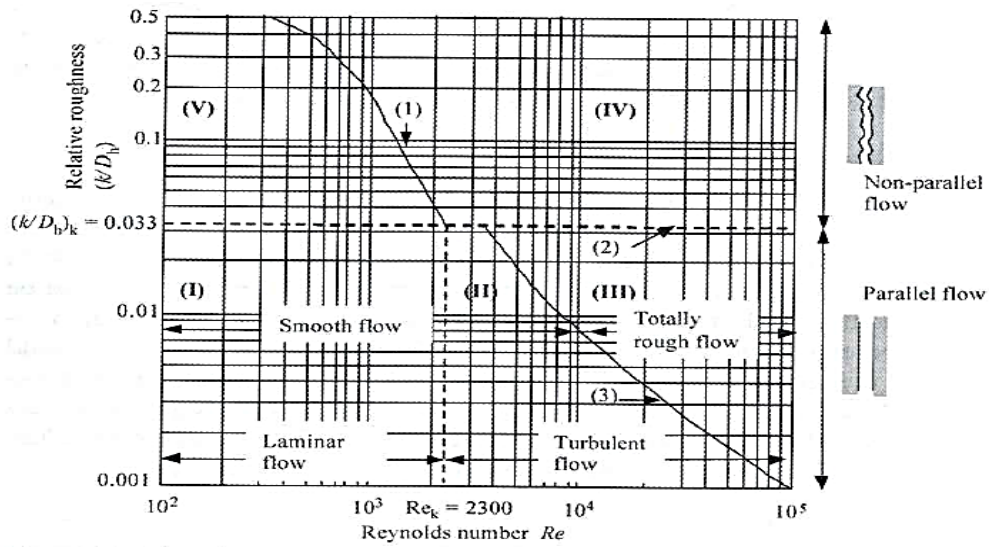


Figure 3.1: Relationship of flow behaviour to relative roughness and Reynolds Number

Source: Louis (1968) and Thiel (1989).

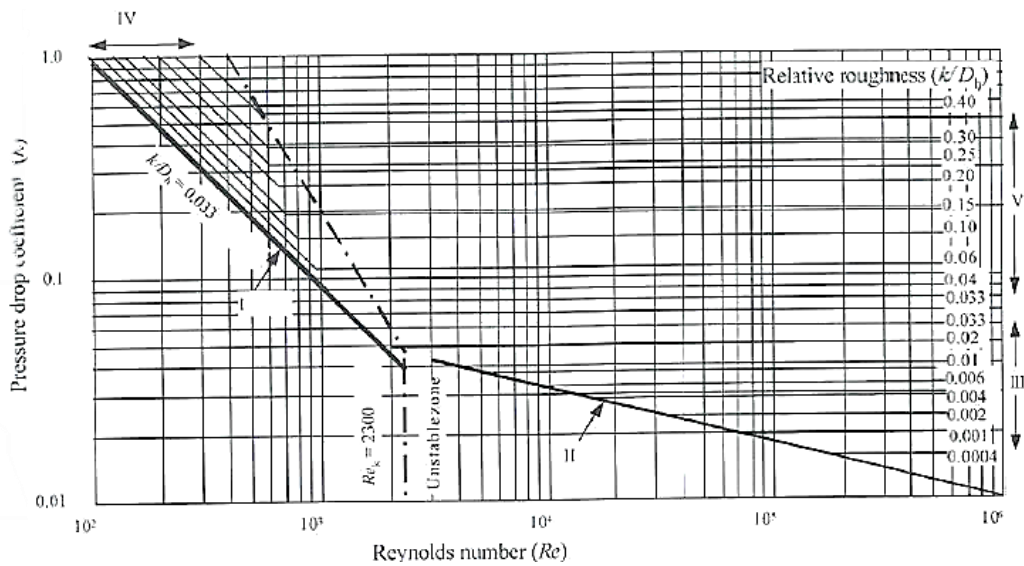


Figure 3.2: Joint flow relationship based on pressure drop coefficient, Reynolds number and relative roughness

Source: Louis, 1976.

3.1.2. Parallel-plate model

SFs are typically envisioned or modelled as parallel plates, allowing fluid flow, described mathematically, using what is known as ‘the cubic law’ (Brush & Thompson, 2003; Singhal & Gupta, 2002; Witherspoon *et al.*, 1980).

Where Equation 3.1 is easily simplified into a one-dimensional equation. The assumption that the aperture is infinitely perpendicular to flow, yields the cubic law equation. This enables the equation to describe fluid flow successfully, provided the following assumptions are observed:

- The fracture plates are smooth, parallel and wide enough to disregard boundary effects.
- Flow velocity is uniform and one-dimensional.
- Unsignifying to maintain a linear flow state (the sectional gradient shape provides rise to parabola).

The relationship between hydraulic conductivity (K_f) of a single plane fracture with aperture (a) is provided by Equation 3.6 (Singhal & Gupta, 2010).

$$K_f = \frac{\gamma_w a^2}{12\mu} \quad \text{Equation 3.6}$$

Equation 3.7 expresses the equivalent hydraulic conductivity of a rock mass, (K_s), with one parallel set of fractures (Singhal & Gupta, 2010):

$$K_s = \frac{a}{s} K_f + K_m = \frac{\gamma a^3}{12 s \mu} + K_m \quad \text{Equation 3.7}$$

Where S is fracture spacing.

Typically, K_m is low, except when the rock-matrix is porous or fractures are filled with impervious fill material. Equation 3.8 expresses the equivalent hydraulic conductivity of a rock mass (Singhal & Gupta, 2010):

$$K_s = \frac{\gamma a^3}{12 \nu \mu} = \frac{g a^3}{12 \nu s}$$

Equation 3.8

Where g is gravitational acceleration (981 cm sec^{-2}) and ν is the coefficient of kinematic viscosity, presenting $1.0 \times 10^{-6} \text{ m}^2\text{s}^{-1}$ for pure water at 20°C .

Equation 3.9 represents the total flow rate (Q_f) per unit plate (fracture) width (Singhal & Gupta, 2010; Witherspoon *et al.*, 1980;):

$$Q_f = \left(\frac{\gamma a^3}{12 \mu} \right) I$$

Equation 3.9

Section 2.4.1.5 of Chapter 2, briefly discussed the validity of the cubic law. The model is continually used for fracture flow modelling, notwithstanding the assumption of an over simplified fracture geometry.

3.2. Numerical modelling techniques

Numerical simulation require establishing methods to acquire distinctive parameters from analysing fractures or collecting field data. Thereafter artificial fractures are created. A physical reality from filed data is reconstructed by numerically simulating the progression of the physical system under various initial settings and exterior load. These methods are required to meet appropriate criteria to ensure efficiency, accuracy, stability and convergence, yielding satisfactory results. The method has limitations. The three major errors include:

- Modelling error: Mathematical theory is used to substitute the representation of natural conditions.
- Discretisation error: Mathematical theory performed a piecewise manner or various equations for field quantities.
- Numerical error: This is because of the limited accuracy of computer arithmetic (Singhal & Gupta, 2010).

Advances in mathematics and experimental research, specifically the use of computers for numerical simulations, deliver forceful and soundly-based options to physical modelling. Numerous computer software for numerical applications exist. These software are easily available; with the successful application thereof, accurate and reliable results can be generated (Singhal & Gupta, 2010).

It is unconceivably easy to be deceived, by merely choosing unsuitable options or pushing a numerical analysis method outside its limits of application. It is essential to understand the analytical tool, including the natural fracture environment, to acquire the necessary fracture parameters to create artificial fractures, using the numerical simulation tool. This includes appreciating the limitations thereof, to assess and contrast the results with the physical reality on a valuable standard. Laboratory experiments might also be necessary, despite entering the field to collect data and conduct field tests (Guo & Tian, 2010). Table 3.1 lists examples of typical numerical modelling methods for fluid flow through fractured rock.

Table 3.3 Typical numerical modelling methods for fluid flow through fractured rock

Modelling Approach	Application	Assumptions
Continuum Approach (model)	Porous rocks such as, sedimentary rocks (where fluid flow occurs through interconnected pores)	Cross-sectional area remains constant; Darcy's law is applied to model fluid flow through porous media
Stochastic Continuum (SC) model/ Geostatistical Approach	Large-scale groundwater flow in heterogeneous rocks	Describes aquifer physical parameters according to spatially varying random functions
Equivalent porous Medium (EPM) / Equivalent Continuum Model (ECM)	Estimate regional groundwater	Behaviour of rock mass system comprising of intensely interconnected fractures is comparable to that continuous porous medium on a sizeable scale

Modelling Approach	Application	Assumptions
Dual porosity (DP)/Double porosity model	Analyses of regional groundwater for fractured aquifers	There is an exchange of water to and from the surrounding porous rock-matrix. Therefore, considers flow occurring in both the rock-matrix and fracture network or discontinuities
Triple porosity (TP) medium model	Karts regions	Flow dynamics vary in inter-granular, flow along fractures, caves and cavern; requires representation of combined effects of the different three porosities
Discrete fracture network (DFN) approach	Fluid flow through hard crystalline rocks/ small-scale fractured rock masses	Flow exclusively occurs through fractures

Source: Indraratna and Ranjith, 2001; Singhal and Gupta, 2010, Zhang and Sanderson, 2002.

CHAPTER 4 : BACKGROUND OF DE HOOP DAM

De Hoop Dam, in the Steelpoort River, was constructed between 2010 and 2014, as part of the second phase of the Olifants River Water Resources Development Project (ORWRDP). Construction was conducted by the Department of Water and Sanitation (DWS). The dam supplies bulk water to the Sekhukhune district of the Limpopo province with a population of 1 169 762. It also supplies water to the mines (Davies, 2006; Van Vuuren, 2008; Yes Media, 2018).

The constructed Roller Compacted Concrete (RCC) dam wall (Table 4.1) has a crest length of 1 016m and a height of 81m. The reservoir has a capacity of $346 \times 10^6 \text{ m}^3$ (Van Der Merwe, 2013).



Figure 4.1: De Hoop Dam (Labuschagne, 2013).

The DWS appointed a consortium, referred to as De Hoop Dam Consultants (DHDC), to supervise the construction of the dam, connected to the Steelpoort River. Knight Piesold Consulting (KPC) was part of DHDC, with the task of mainly managing the geological engineering aspects, such as geological foundation mapping and monitoring of geotechnical processes on site during the construction. Subsequently, KPC provided recommendations concerning the existent founding conditions of the dam wall (Van Der Merwe, 2013). The data presented, serves as a basis for the current research and was obtained from KPC. DWS granted permission to use the data.

4.1. Site location and description

The study is located on the farm, De Hoop 886 KS, 27 km southwest of Steelpoort and 26 km north of Roosenekal in Limpopo (Figure 2.2).

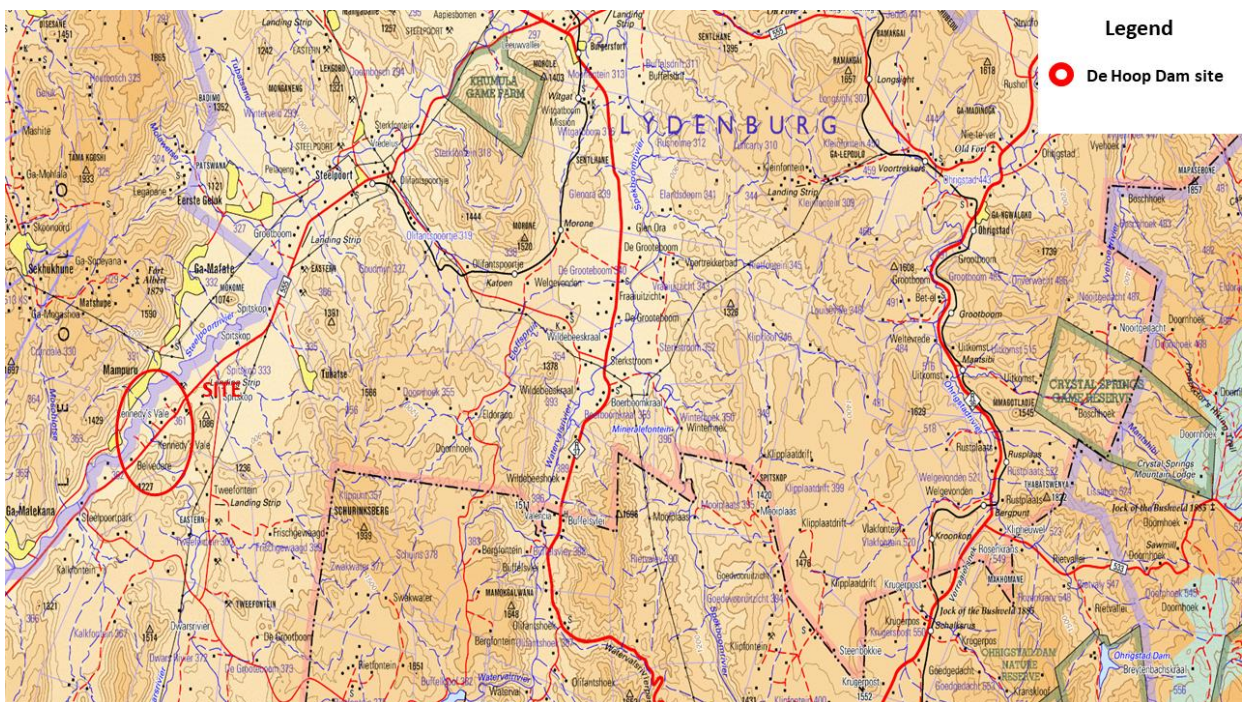


Figure 4.2: Extract from the 1:250 000 topocadastral sheet, 2430 Pilgrim’s Rest (2000), indicating the locality of the De Hoop farm

The dam wall is divided into three zones, indicating the right flank, the river section or spillway and the left flank. These zones are further subdivided into 10m foundation

blocks. Each block is assigned a specific number, depending on the location. Odd numbers are assigned to the right flank (western side of dam wall) and even numbers to the left flank blocks (eastern side of dam wall). The centre of the spillway serves as the starting point - Block 1 (Figure 4.3), initiating numbering. The Chainage (Ch) indicates the length of the dam wall in metres on a reference line from a fixed point “A”.

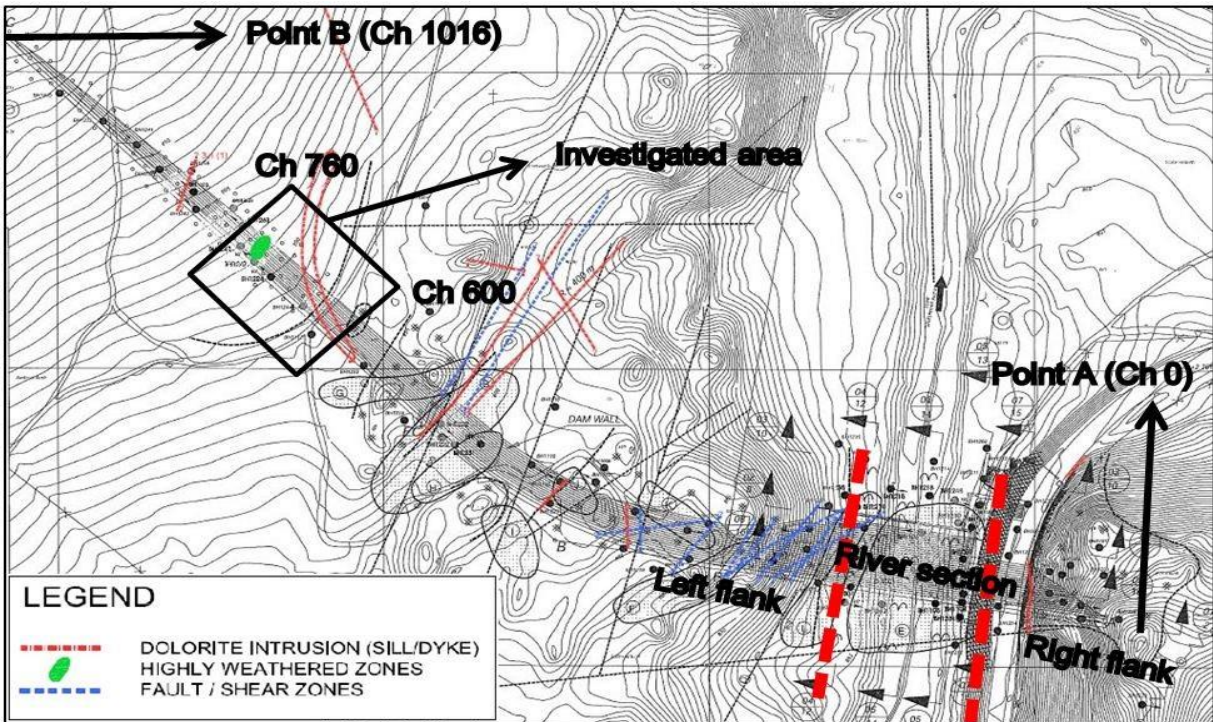


Figure 4.3: Plan view of De Hoop Dam and investigated area

Source: Van Der Merwe, 2013.

For the study, the Chainage (Ch) commences from the right flank of the dam, measured on the dam reference line from east point A (Ch 0) to west point B of the dam wall (Ch 1016). Table 4.1 provides a summary of the chainage, number of blocks and the block numbers for the three zones of the dam wall.

Table 4.1: Summary of the three dam wall zones

Zones	Left Flank	River Section	Right Flank
Chainage	220 to 1016	220 to 110	110 to 0
Blocks	170 to 12	10 to 2 and 1 to 11	13 to 33
Number of blocks	79	11	11

Source: Van Der Merwe, 2013.

4.2. Regional geology

The dam site is located on rocks of the eastern limb of the layered intrusive igneous rocks of the Rustenburg Layered Suite (RLS) of the bushveld igneous complex as depicted in Figure 4.4. The dam basin is underlain by magnetite gabbro-norite of the Upper Zone of the RLS, whilst the dam wall foundation is underlain by uniform gabbro rocks of the main zone in the RLS. The layered intrusive igneous rocks of the RLS obliquely dip in a north-westerly direction with a gradual dip of 8° to 13° (Brink, 1979).

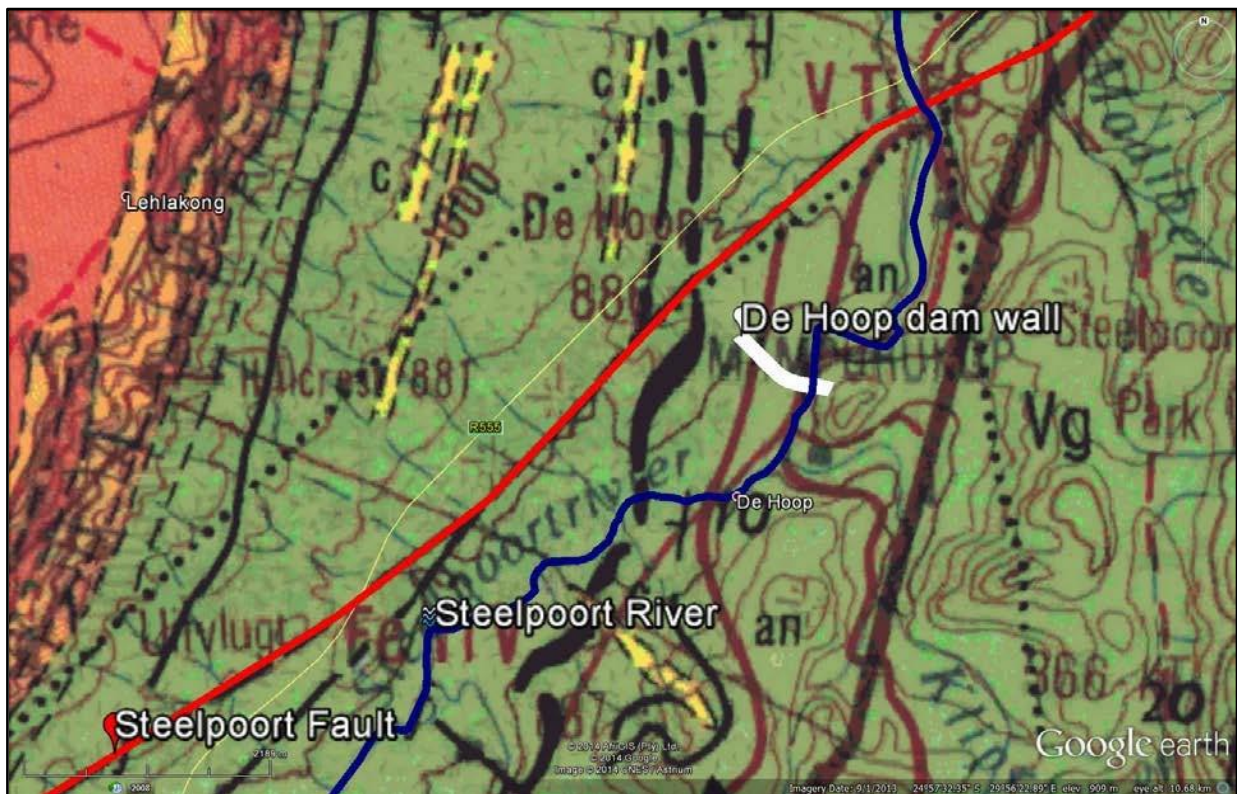


Figure 4.4: Extract from the 1: 250 00 sheet, 2428 Nylstroom (1978), indicating regional geology of the study area

The major northeast-striking Steelpoort fault (Figure 4.4), occurs approximately 600m west of the left flank. The fault's strike length exceeds 100 km with a maximum measured displacement of 750m near the dam site. Although the Steelpoort fault is not easily traceable on either satellite images or aerial photographs on surface expressions, it can be traced through minor streams, occurring on the flatter slopes of the western escarpment. The fault is regarded as inactive, resulting from a lack of anticipated future disturbances on the drainage patterns of the dam site (Brink, 1979).

4.2.1. Left flank geology

The underlying bedrock between Block 90 and 130 comprises gabbro rocks from the main zone of the RLS. The joints strike predominantly north-west and north-east with dips ranging from 15° to 87°. The area also comprises numerous minor faults, pegmatite veins, dolerite intrusions and anorthosite zones, resulting in widespread

structural complexities. These structural features are considered to be initiated by the Steelpoort fault (Van Der Merwe, 2013).

The minor faults normally strike in a north to north-east direction in consort with varying dip angles of between 44° to 80°, whilst a few small-scale minor faults strike in an east to west direction. Some of the minor faults are filled with sandy clay. The faults' aperture thicknesses are largely between 2mm to 50mm (Van Der Merwe, 2013).

Dolerite intrusions, likewise encountered in the area, possess varying thicknesses of between 0.4m to 4m. Some of the inferior geological zones encountered are associated with these dolerite intrusions and often are related to the gabbro (dolerite) contact zones, whilst the few anorthosite zones, are generally closely jointed near fault contacts and moderately weathered (Van Der Merwe, 2013).

4.2.2. Pegmatite vein in the left flank

The aforementioned feature was identified in Blocks 92, 108 and 110 with a prominent northerly strike direction and dip angles of between 55° and 80°. The feature is thought to be associated with fault and shear zones in the dam foundation footprint. Furthermore, it has varying thicknesses from 20mm to 200mm and infilled with loosely packed pegmatite gravel (Van Der Merwe, 2013).

Figure 4.5 illustrates the pegmatite vein, 250mm wide, identified during a site visit. The feature terminates in the highly weathered adjacent gabbroic rock at both the top and bottom. The *in situ* description thereof is found in Appendix I.



Figure 4.5: Approximate location of pegmatite vein, with an approximate width of 250mm



Figure 4.6: Exploded view of the highly weathered and jointed pegmatite vein

Wagner (1925, 1929 cited in Viljoen & Scoon, 1985) was one of the first researchers to describe these transgressive bodies. He referred to them as hortonolite dunite. Wagner further established that the aforementioned bodies can occur as two distinct features indicating platiniferous and nonplatiniferous. Platiniferous is characterised by a well-defined invariable platiniferous core, enclosed in a larger composite body of magnesian dunite. Nonplatiniferous does not have magnesian dunite. It is closely associated with pegmatitic wehrlites and pyroxenites with Ti magnetite and ilmenite as the major constituents.

Viljoen and Scoon (1985) referred to the discordant features as iron-rich ultramafic pegmatite, stating that they are ubiquitous throughout the upper critical and main zones of the Bushveld Complex. Appendix III illustrates the various foundation blocks where the pegmatite occurred. The following classification was established for the various discordant and post cumulus ultramafic rocks that occur in the Bushveld Complex (Viljoen & Scoon, 1985):

- Iron-rich ultramafic pegmatite with two subgroups: A silicate-rich variety where these are lesser Fe-Ti oxides, compared to olivine and clinopyroxene; and Fe-Ti oxide pegmatite.
- Nonplatiniferous magnesian dunite.
- Platiniferous ultramafic pipes.
- Other bodies, such as Vlakkfontein nickel pipes, orthopyroxenite pegmatite, anorthosite pegmatite and vermiculite-bearing pegmatite.

Alternatively, the pegmatite bodies may be classed as simple or complex. Simple pegmatites comprise simple mineralogy with no internal zoning and conversely, complex pegmatites comprise complex mineralogy, numerous rare minerals and conspicuously distinctive zonal sequences (Evans, 1993).

Figure 4.7 and Figure 4.8 respectively, illustrate the distribution and occurrence of these iron-rich ultramafic pegmatites in the eastern limb of the Bushveld Complex. They are further abundant in the areas adjacent to the Steelpoort River. A few occur in the extreme northern and southern directions of the eastern Bushveld Complex.

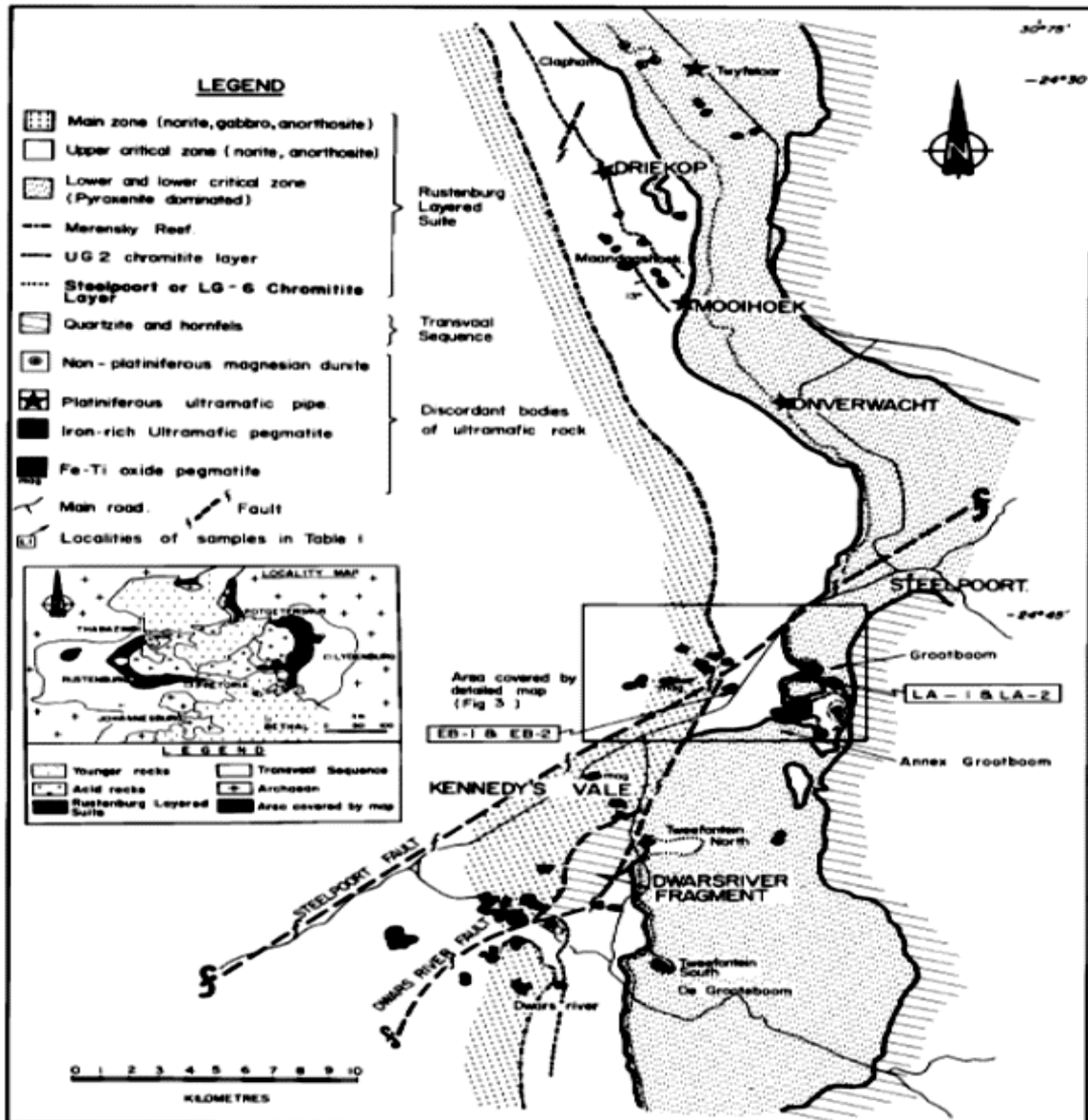


Figure 4.7: Geologic setting of some of the discordant bodies of ultramafic rock in part of the eastern Bushveld Complex

Source: Viljoen and Scoon, 1985.

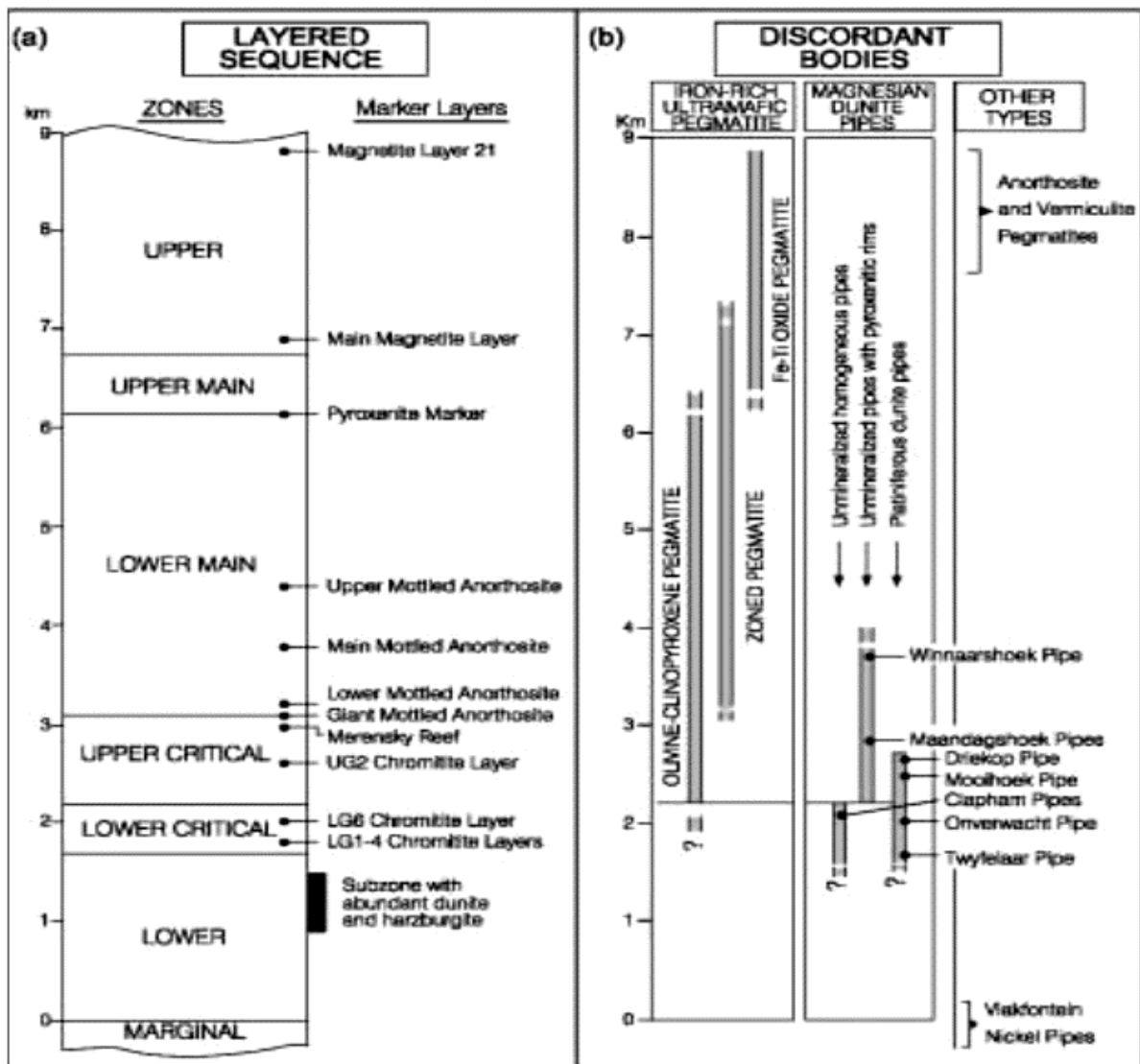


Figure 4.8: (A) Zonal subdivision of the layered sequence in the eastern limb of the Bushveld Complex concerning important marker layers. (B) Vertical distribution of the different types of discordant ultramafic body

Source: Scoon and Mitchell, 2004, adapted from Scoon and Mitchell, 1994.

The iron-rich transgressive bodies are highly fractionated and characterised by textured variability and high specific gravity. They mainly comprise varying proportions of hortonolite, ilmenite, clinopyroxene and Ti magnetite. In addition, they may occur in a variety of forms such as, small, podlike bodies and veins to large,

pipe like masses with diameters, exceeding one kilometre. Individual bodies are significantly discordant, whilst locally, they form sheet like bodies, dislodging specific cumulate layers (Viljoen and Scoon, 1985). Similarly, Viljoen and Scoon (1985) observe that the discordant bodies occur in disturbed areas, marked by extensive faulting and post-bushveld dykes.

In this study, no distinct zoning is identified from the observed pegmatite veins. The XRD and XRF (Figure 4.9 and Figure 4.10), conducted on samples collected from the site, indicate a simple mineralogy with the samples predominantly rich in calcium and aluminium. The pegmatite in this study may be classified as a simple pegmatite.

Pegmatite material 1 and 2 are samples collected from pegmatite veins, occurring in various areas along a similar outcrop, whilst the surrounding rock material refers to the host rock, particularly taken, adjacent to Pegmatite 1 material.

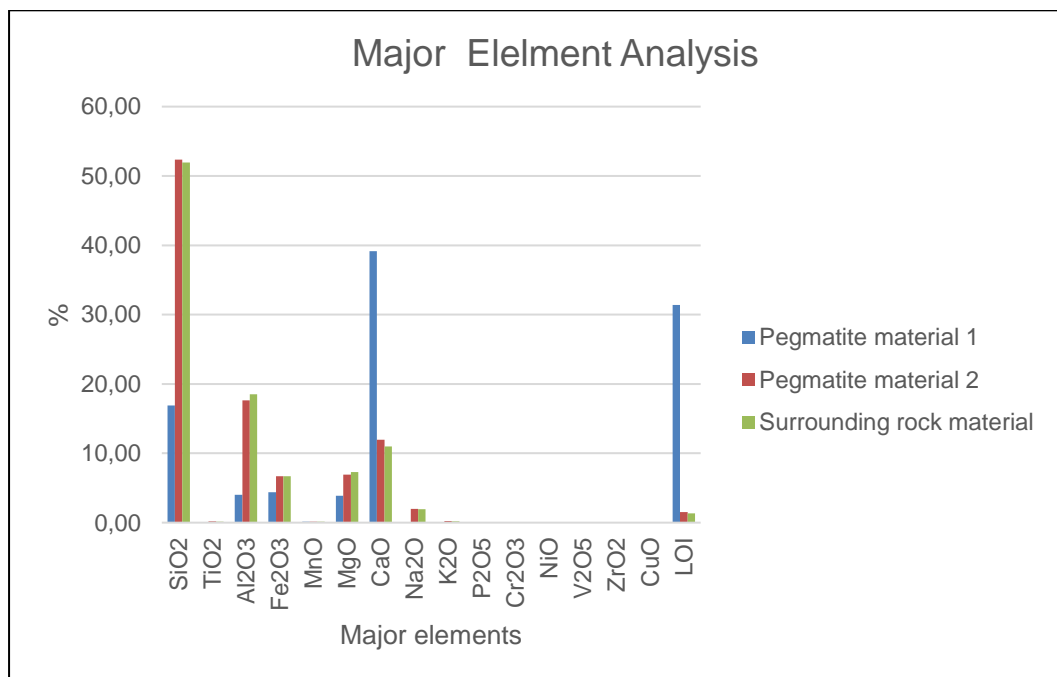


Figure 4.9: Major element analysis of three samples

Figure 4.10 illustrates the typical composition expected in gabbro-norites. Whilst the occurrence of secondary minerals, such as calcite smectite, identified as montmorillonite, talc and chlorite (although in lesser amounts), is indicative of the nature of weathering that the rocks experienced. This is illustrated in Figure 0.11. The figure was initially used to determine the type of weathering rocks used in various regions that roads would undergo, using what is referred to as “Weinert N-value”. According to Weinert (1980), mechanical weathering as expected in areas with an N-value greater than five. Chemical decomposition is expected where an N-value is less than five. This value is determined by Equation 4.1 (Weinert, 1980):

$$N = \frac{12E_j}{P} \quad \text{Equation 4.1}$$

Where E_j = average January evaporation, P = annual precipitation.

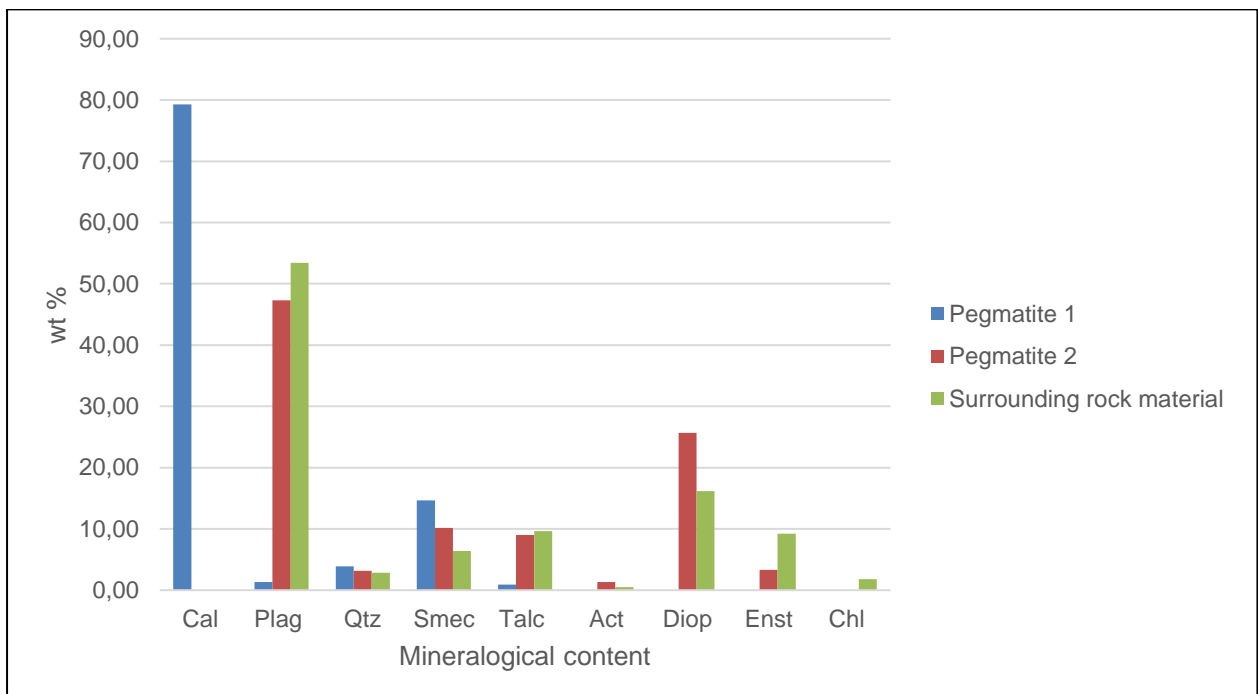


Figure 4.10: Mineralogical content of three samples

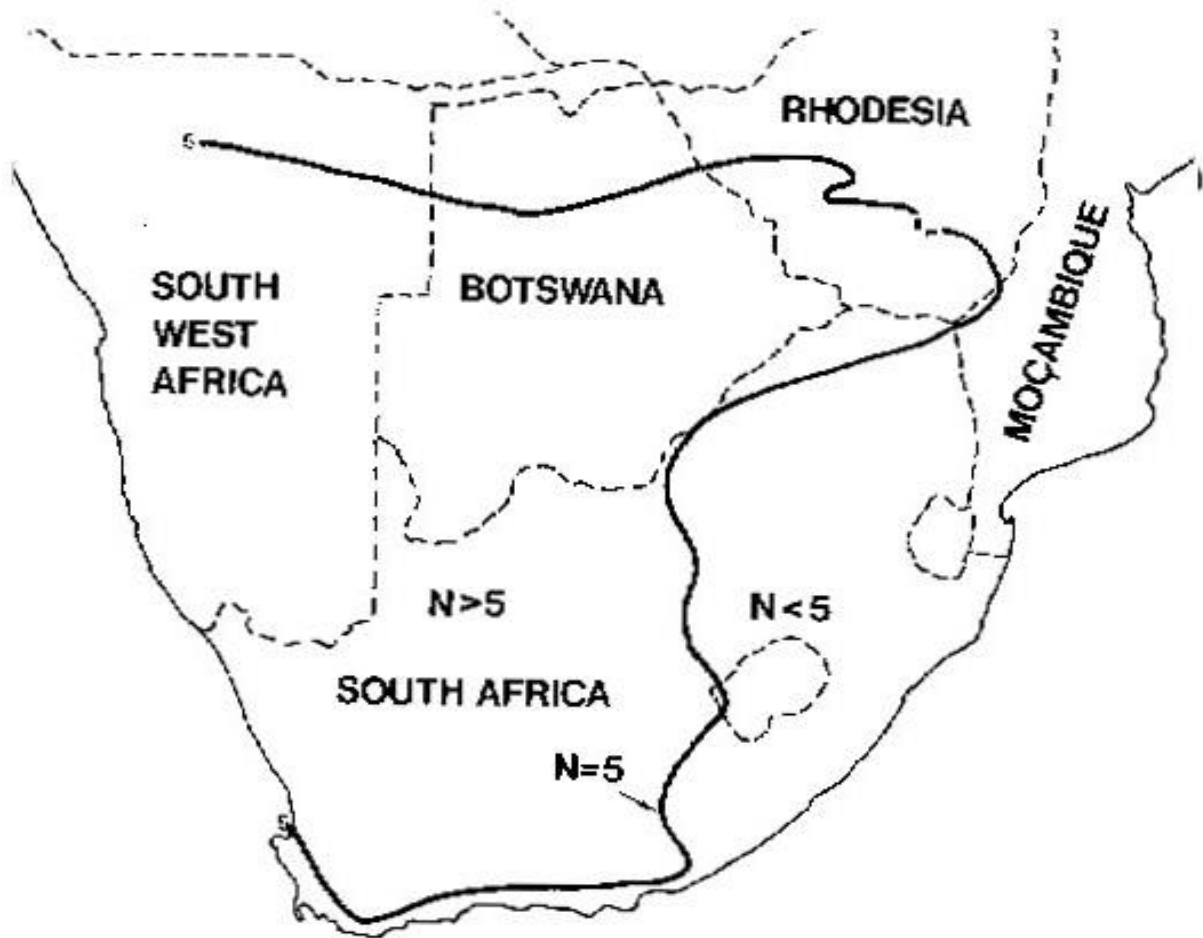


Figure 4.11: Climatic N-value = 5 plotted for southern Africa (From Weinert, 1980)

4.3. Statistical and comparative analysis of left flank joint line surveys dam data

Ample of the geological foundation mapping data collected by KPC, entailed recording major geological features, including the orientation of each foundation block. Subsequently, digital photographs of each block foundation were taken in the upstream and downstream direction. JLS was performed for each foundation block in two directions. First, in the direction parallel to the dam reference line. Secondly, in the direction perpendicular to the reference line. Thereafter, display sheets of each block were generated, containing the geological foundation mapping, rock

mass descriptions and foundation photographs. This created stereo plots of surveys in each block (Van Der Merwe, 2013).

From the JLS and packer testing data, Roux (2014) conducted a statistical and comparative analysis, to examine whether a correlation exists between essential discontinuity parameters (roughness, aperture and infill) and Lugeon values. The JLS data were thoroughly checked and filtered to identify incomplete and erroneous recordings. This included (discarding JLS data entries) recorded parameters. Data from parallel and perpendicular JLS recordings, were combined into a single sheet and assigned a specific block number (Figure 4.12).

Dip	Dip Direction	Block No.	Ref line	Distance	Type	Hardness	Weathering	Structure	Dip Length	Dip Ends	Strike Length	Strike Lengths	Roughness	Discontinuity Hardness	Amplitude	Base	Aperture	Fill Type	Fill Consistency
13	291	88	Parallel	0,2	G	R4	S-U	T	1	1	0,7	2	10		40	0,6	0		
13	291	88	Parallel	0,6	G	R4	S-U	T	1	1	0,7	2	10		40	0,6	0		
88	185	88	Parallel	1	G	R4	S-U	T	0,1	0	0,6	2	11		10	0,2	0	Ss	
88	185	88	Parallel	1,3	G	R4	S-U	T	0,1	0	0,6	2	11		10	0,2	0	Ss	
86	54	88	Parallel	1,8	G	R4	S-U	T	0,1	0	0,7	2	10				0	Sd	
74	176	88	Parallel	2,3	G	R4	S-U	T	0,1	0	0,9	2	10				0	Sd	
74	176	88	Parallel	2,5	G	R4	S-U	T	0,1	0	0,9	2	10				0	Sd	
20	242	88	Parallel	3	G	R4	S-U	T	1,7	1	2,1	2	13		40	0,9	0	Sd	
87	327	88	Parallel	4,4	G	R4	S-U	T	0,1	0	1,5	2	12				1	Wr	
87	327	88	Parallel	4,6	G	R4	S-U	T	0,1	0	1,5	2	12				1	Wr	
87	327	88	Parallel	5	G	R4	S-U	T	0,1	0	1,5	2	12				1	Wr	
20	245	88	Parallel	0	G	R4	S-U	T	2,5	1	2,4	2	12		20	0,4	5	Sd	
85	15	88	Perpendicular	1,3	G	R4	S-U	T	0,2	0	0,3	2	10				0	Sd	
25	355	88	Perpendicular	1,6	G	R4	S-U	T	0,7	1	0,7	2	12		30	0,5	0		
70	30	88	Perpendicular	2,1	G	R4	S-U	T	0,2	0	1	2	11				0	Sd	
60	232	88	Perpendicular	2,3	G	R4	S-U	T	0,1	0	0,4	2	10				0	Sd	
21	294	88	Perpendicular	2,7	G	R4	S-U	T	0,5	1	1,5	2	12		10	0,3	0	Sd	
76	193	88	Perpendicular	3,8	G	R4	S-U	T	0,1	0	0,2	2	10				0	Sd	
77	54	88	Perpendicular	4	G	R4	S	T	0,2	0	0,5	2	11				1	Sd/Ss	

Figure 4.12: Illustration of the final combined JLS data sheet

Source: Roux, 2014.

There were 1153 data entries for the 16 blocks of the left flank foundation between Ch600m and Ch760m where water leakage occurred. To simplify the large quantity of JLS data; the data was grouped into three main discontinuity groups indicating tension, faults and stress relief joints. All the blocks were combined to calculate the averages of each group. The discontinuity group with the greatest influence on

permeability, were analysed, to find a possible correlation between a discontinuity parameter or a set of parameters that may influence the permeability. Table 4.2 provides a summary of average parameter values between the three considered discontinuity types.

Table 4.2: A summary for s the average parameter values for three discontinuity types

Data Entries (1151)	Rock Description				Continuity		Surface		
	Structure	Hardness	Weathering	Type	Dip	Strike	Roughness (JRC)	Waviness	
					Length (m)	Length (m)		Amplitude (mm)	Base (m)
1004	Tension joints	Strong rock (R ₄)	40% Unweathered to slightly 39% Slightly 13% Unweathered	86% Gabbro 10% Dolerite 4% Anorthosite	0,34	1,18	9,9	24	0,57
132	Fault fractures		46% Unweathered to slightly 24% Moderately 14% Slightly	90% Gabbro 10% Anorthosite	0,31	5,23	11,31	146,27	2,25
15	Stress relief joints		47% Unweathered to slightly 33% Slightly 13% Moderately	100% Gabbro	0,32	0,69	10,86	35,71	0,51

Source: Roux, 2014.

Stereographic projections were constructed for each major structural group, to primarily identify any possible relationship between discontinuity groups, leading to greater or lesser permeability. Projections the following conclusions were made, from the JLS and stereographic:

- Tension joints possessed two major joint sets, Figure 4.13a, with the orientations J1 - 298/18 and J2 - 233/87.
- The fracture faults exhibited three prominent fracture sets, Figure 4.13b, with the orientations S1 - 140/58, S2 - 253/85 and S3 - 216/80. These fracture faults predominantly strike perpendicular to sub-perpendicular to the dam wall. Other than the aforementioned, a few small parallel-striking fracture faults exist.
- The 15 stress relief joints (Figure 4.13c), exhibit no particular orientation. This is further illustrated by the scattered poles.

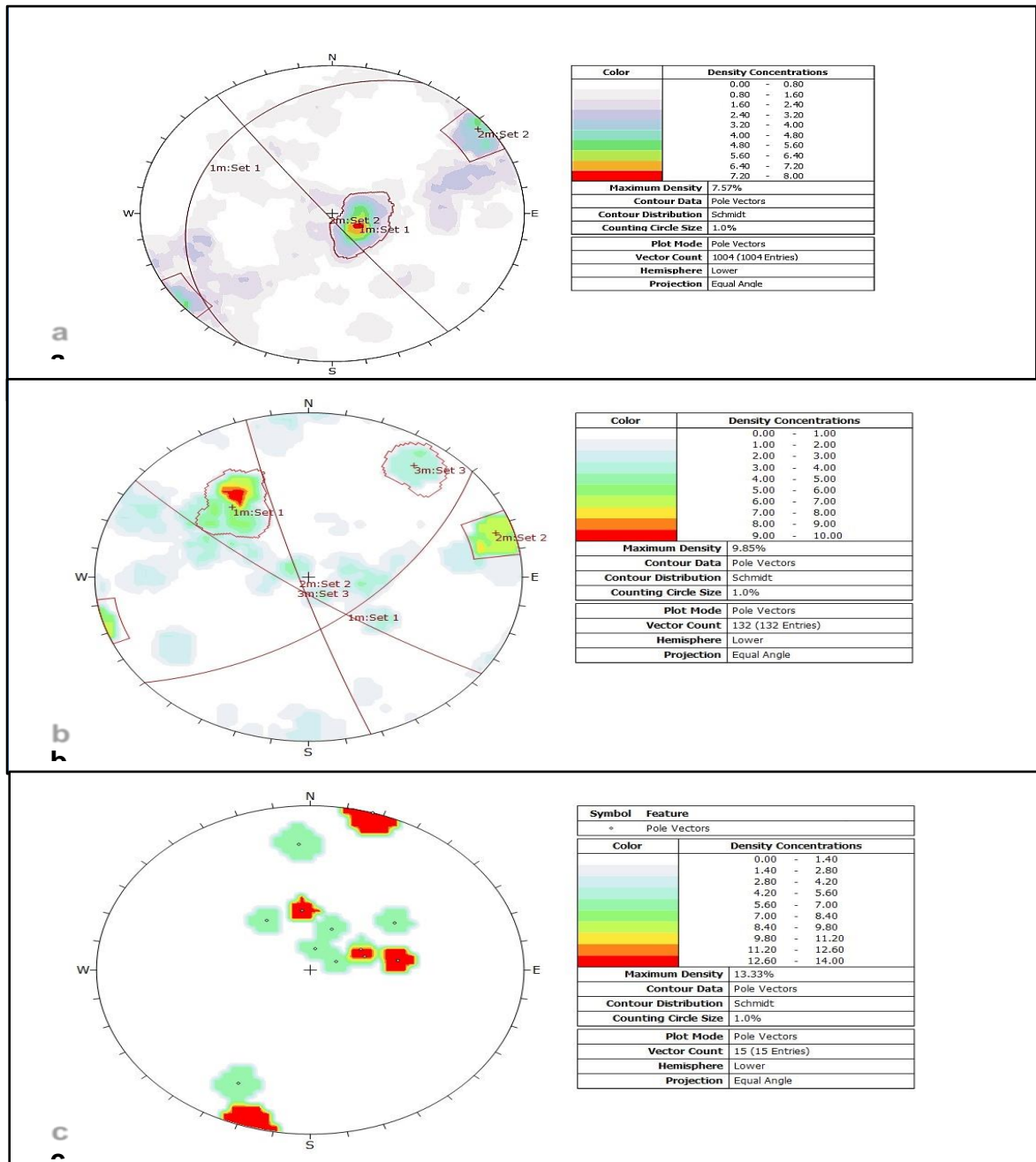


Figure 4.13: a) Stereographic projections of the tension joints with two prominent sets. b) Stereographic projections of the fracture faults with fracture sets. c) Stereographic projections of the stress relief joints

Source: Roux, 2014.

Much emphasis was placed on fault fractures, since stress relief joints and tension joints performed little or no part, in rock mass permeability. Subsequently, joint parameters leading to low and high permeability fault fracture zones, were considered (Table 4.3). Averages for roughness and aperture are respectively provided, including weathering and fill type.

Table 4.3: A summary for the average values obtained for high and low permeability fault fractures zones

Fracture faults	Weathering	Roughness (JRC)	Aperture (mm)	Fill type	Blocks
High permeability zones	<ul style="list-style-type: none"> Moderately weathered rock (40%) Unweathered to slightly weathered rock (40%) 	11.10	13.10	<ul style="list-style-type: none"> Mostly no data recorded (42%) Weathered pegmatite (27%) 	92,94,96, 108,110,114 and 116
Low permeability zones	<ul style="list-style-type: none"> Unweathered to slightly weathered rock (53%) Slightly weathered (17%) 	11.50	20.30	<ul style="list-style-type: none"> Stained (40%) Weathered rock (27%) 	88, 90, 98,100,102, 104,106,112 and 118

Source: Roux, 2014.

Stereo plots of the fracture faults for zones of high permeability, illustrate the existence of two prominent fracture sets viz S1 - 149/64 and S2 - 124/11 (Figure

4.14). Most of the fractures are still scattered, as the maximum pole density are 11.76%. The two joint sets strike in a north-east direction, perpendicular to the dam wall.

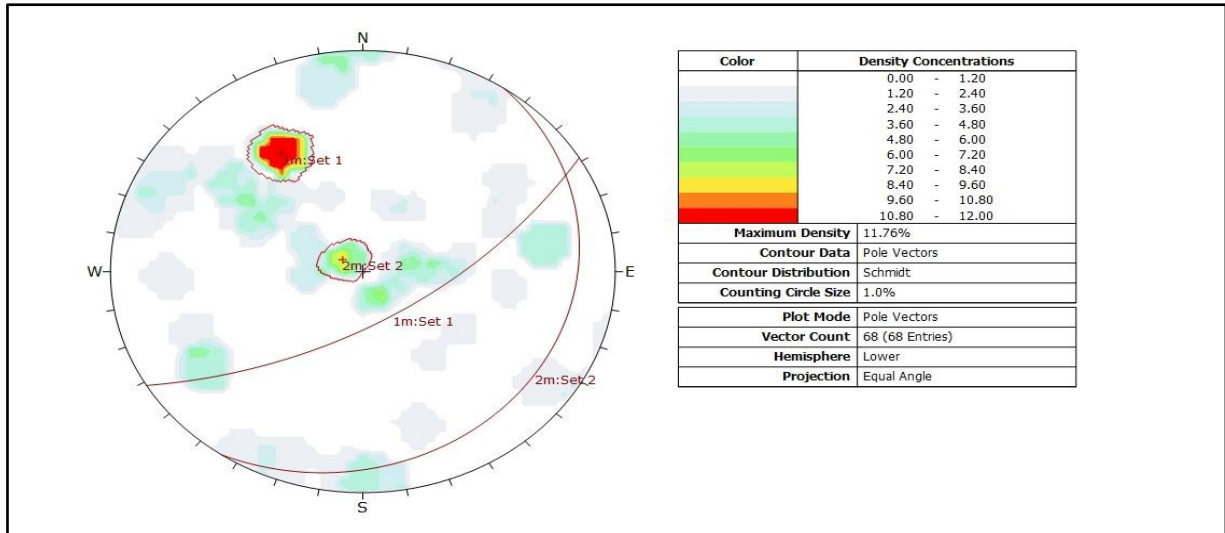


Figure 4.14: Fracture fault stereographic projection of high permeability blocks

Source: Roux, 2014.

Whereas for fracture faults situated in the low permeability blocks, the stereo plot in Figure 4.15 illustrate the blocks holding three prominent fracture sets, opposed to two in the high permeability blocks. The orientation of three fracture sets are S1 - 253/85, S2 - 140/54 and S3 - 217/80. Compared to Figure 4.14, the stereo plot indicates less scatter of poles, with a maximum pole density of 14.06%.

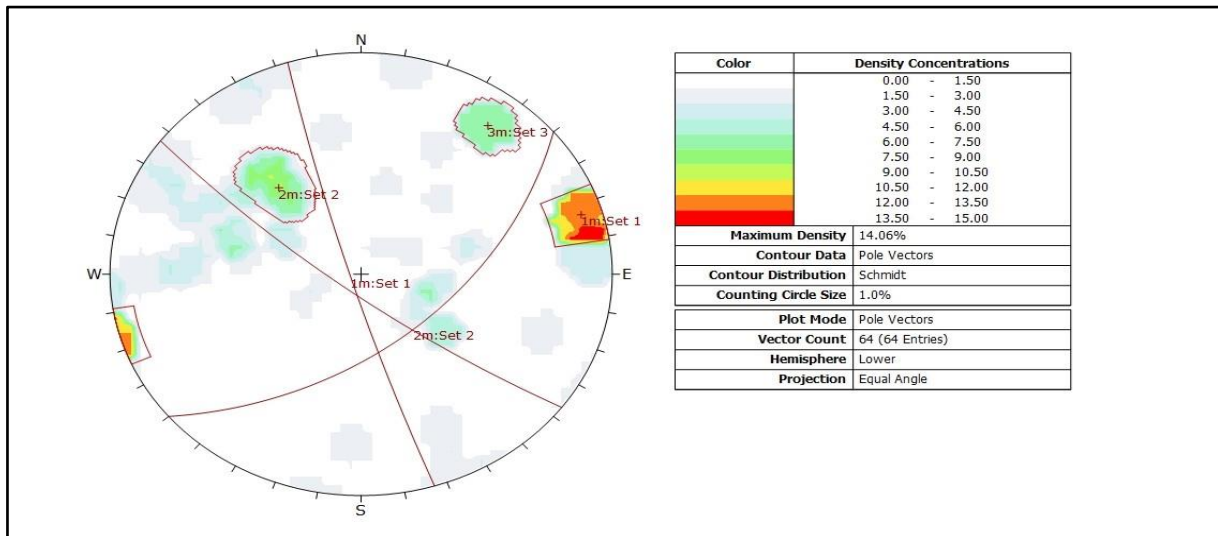


Figure 4.15: Fracture fault stereographic projection of low permeability blocks

Source: Roux, 2014.

4.4. Current state of left flank seepage flow

The seepage monitoring data are mainly collected by site staff on a daily basis through inspection of seepage areas, monitoring points and drainage hole discharge points. The excessively high seepage values were recorded, since the completion of the dam wall (KHH, 2015).

During dam construction, unexpectedly high Lugeon values were obtained from grout curtain borehole drilling. This prompted the release of a report, concerned with evaluating the degree of seepage flow from the left flank, corresponding to Blocks 90 to 130 (Ch600 to Ch820), including efficiency of existing monitoring procedures. According to the report, the main areas of high seepage indicate flow through induced cracks in the wall, the gallery and more significantly, at the toe drain hole areas on the left flank downstream of the dam (KHH, 2015).

The grouting results of the aforementioned blocks, indicate five areas of higher permeability in the first, and sometimes second stages of grouting. According to a preliminary report by KHH (2015), considerably high Lugeon values, between six and 17, were encountered in some of the primary and secondary holes in the first and

second testing stages. Copious quantities of grout had to be injected into these zones to significantly reduce the rock mass permeability. The grouting was extended to quaternary sequence spacing where Lugeon values of less than two were recorded. The five main areas with significant seepage flows, are summarised in Table 4.4: Five areas of significant seepage flows.

Table 4.4: Five areas of significant seepage flows

Block or Chainage No.	Grouting Stage	Associated Geological Structures
Block 92 (Ch620-Ch630)	Stage 1	Pegmatite band
Blocks 108 and 110 (Ch700-Ch720)	Stages 1 and 2	Pegmatite band, dolerite and anorthosite
Block 114 (Ch730-Ch740)	Stage 1	Anorthosite band
Blocks 122 and 124 (Ch770-Ch780)	Stages 1 and 2	Fault zone a closely jointed zone
Blocks 128 and 130	Stages 1 and 2	Several distinct faults

Source: KHH, 2015.

The research will provides particular attention to Block 108 and Block 110 (Chainage 700-720) - where the pegmatite vein occurs. Although detailed evaluation of monitoring seepage flows and grouting operations are equally important, these are outside the scope of this study.

CHAPTER 5 : MATERIALS AND METHODS

Through constructing an artificial joint with varying discontinuity parameters, such as roughness and aperture, this research endeavours significant observations on variable saturated fracture flow. Appropriate spacer sizes are used to generate aperture and keep the roughness (smooth) constant. Appropriate roughness surfaces are generated and the aperture is kept constant, to deduce the influence of aperture and roughness on flow. There are various materials to select from as illustrated by previous studies (Brown *et al.*, 1998; Singh *et al.*, 2014; Su *et al.*, 1999 & Tzelepis *et al.*, 2015). Considering this wide choice of materials suitable for various rock modelling (Table 5.1), two of these material types are used to optimise their use and the method of testing, to collect meaningful data.

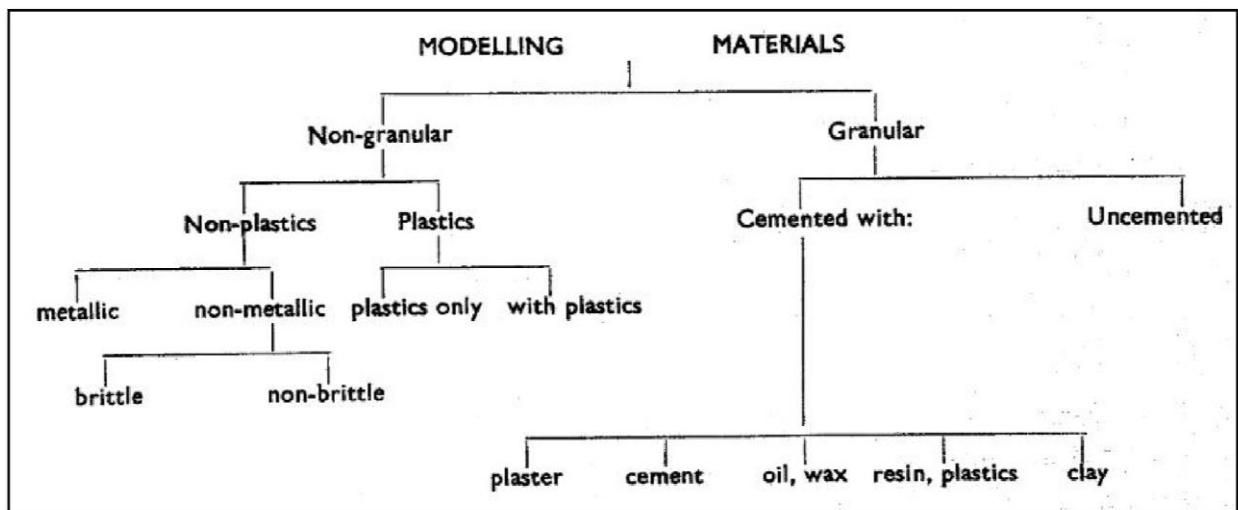


Figure 5.1: Simple classification of modelling materials

Source: Stimpson, 1970.

5.1. Experimental set-up

5.1.1 Model description

The model comprises two rectangular plexiglass sheets, with dimensions 400mm x 290mm x 10mm (Figure 5.2 and Figure 5.3), to simulate a vertical SF. As a result of the choice of material opted, the model assumes impervious rock-matrix, excluding effects of matrix imbibition. The fracture model rests on a 760mm high table, whilst the inflow container lies at approximately 1335mm from the table surface. The flow travel tube from inflow to the fracture, has a length of 1310mm. In the instance of fracture aperture, the two rectangular plexiglass sheets are separated through plexiglass strips, simulating the appropriate apertures used, indicating: 0.18mm, 0.5mm, 1mm, 1.5mm, 2mm and 3mm.

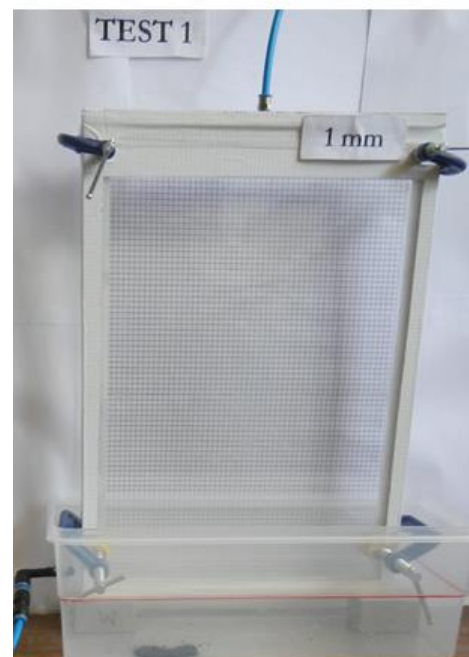
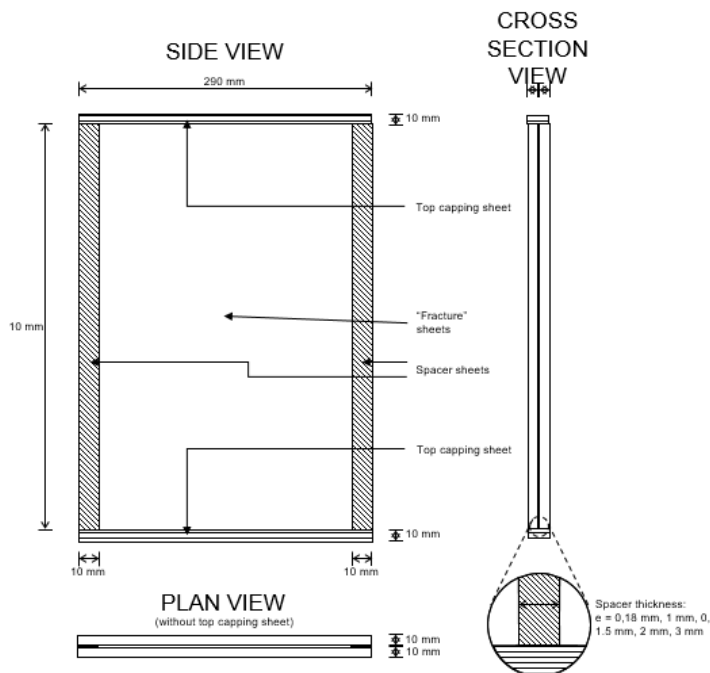


**Figure 5.2: Schematic of plexiglass single;
fracture model**

**Figure 5.3: Built
model;**

5.1.2 Roughness tests

A similar test set-up are used for roughness tests, at a constant aperture of 0.5mm, assuming the surface profiles possess JRC values of 0-2, 4-6, 10-12 and 14-16. Only one surface is altered, whilst the other is kept smooth, aiding observations during the tests. As a consequence, the spacing in the rock roughness models is controlled by the sample waviness.

The first profile, JRC 0-2, is equivalent to an 0.5mm aperture test for a smooth surface. Secondly, JRC 4-6, hold one of the sheets, roughened with sand paper and a hand-held steel threaded rod (file) (Appendix IV). For the remaining surface profiles, two rock samples (Figure 5.4 and Figure 5.5). It is assumed that these samples emulate the assumed JRC values of 10-12 and 14-16 respectively, collected with one side of their surfaces moulded.

Each sample is placed in an approximately 400mm x 290mm impervious wooden box, with the fracture surface to be moulded, facing upwards. Following recommendations by Develi and Babdagli (2014), an aerosol mould releaser is first sprayed as a thin layer over the rock surface, preventing small pieces from being plucked from the fracture surface by the resultant silicon mould when removing it from the original surface after curing.

The silicon-making rubber, a mixture of Silicon 3030 SM013 (Part A) and Silicon 3030 Catalyst SM014 (Part B), are poured over the fracture surface in the wooden box. According to product recommendations, the mould must be left to cure for four hours at room temperature (23°C) and post curing. It must be left an additional four hours at 65°C to eliminate any residual moisture and alcohol (a by-product of the condensation reaction) that can prevent cure of some urethane resins and rubbers. The moulds are left at room temperature for 24 hours, before removing it from the rock surfaces.

The mould is placed on a flat plane with the rough surface facing upwards. The model is then created, by casting Polyclear 555, an orthophthalic acrylic-modified clear casting

resin, mixed with Butanox M50 and white marble dust - a filling agent, used to prevent any air bubbles, onto the silicon rubber and left for an hour to harden. The resulting white polyclear cast is then removed from the silicon rubber (Figure 5.6 and Figure 5.7).



Figure 5.4: Granite sample



Figure 5.5 Mudrock sample

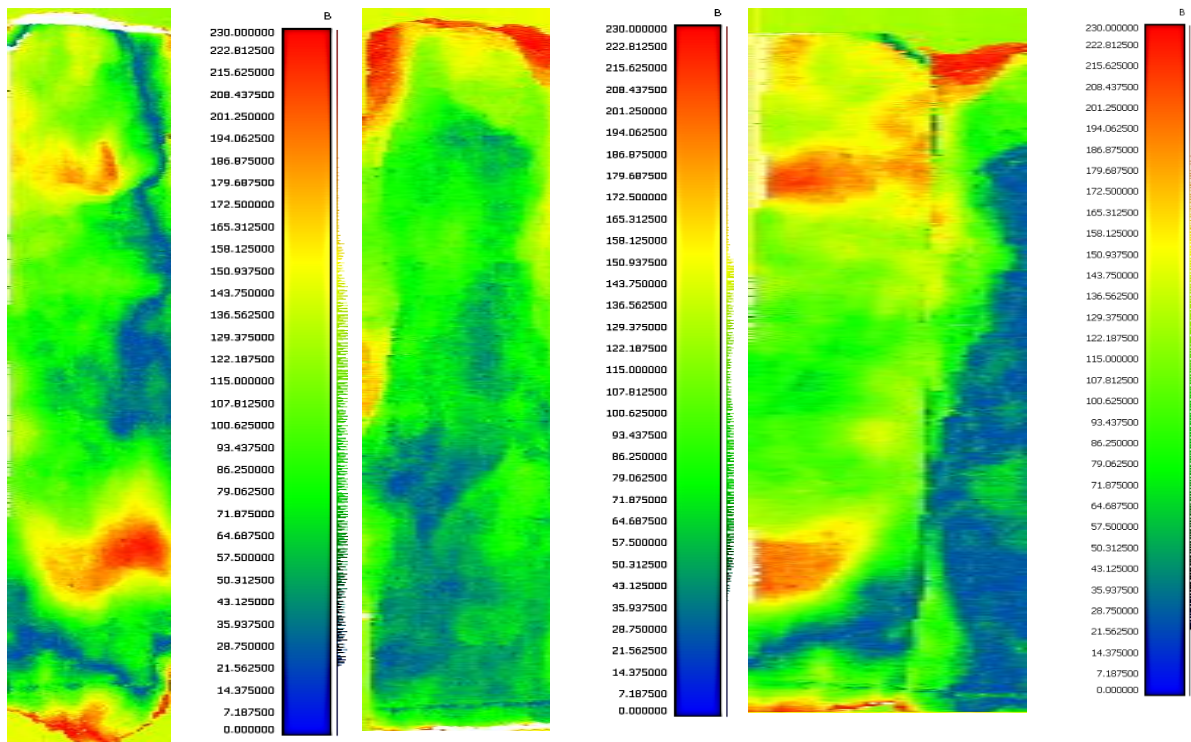


Figure 5.6: Casted granite sample



Figure 5.7: Casted Mudrock sample

The casted samples are laser scanned, to provide indication of the surface topography (Figure 5.8 and Figure 5.9). Surface points of higher relief are indicated in red, with the gradual decrease of these in yellow. Where the surface becomes more evenly, these points are marked in green and points lower relief are indicated in dark blue. The scanner can only scan a small width, as approximately indicated by the black dashed lines in Figure 5.7. The two halves from the first sample were therefore scanned separately.



Left-hand side scan Right-hand side scan Sample scanned as is

Figure 5.8: Granite laser scan image

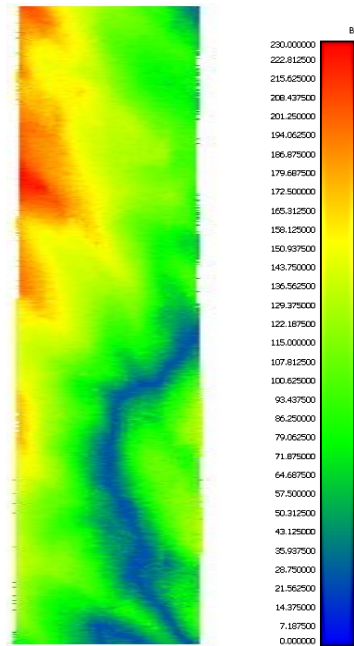


Figure 5.9: Mudrock laser scan image

Transparent plexiglass plates allow for easy and direct identification of various means of fluid flow advancement, through smooth and rough surfaces. Epoxy casts provide an accurate reproduction of the fracture surface morphology and also exhibiting the influence of uneven surfaces on fluid flow behaviour and distribution (Su *et al.*, 1999).

Some of the differences between epoxy replicas and natural rocks, include the various stress states and mating of the epoxy fracture replicas, varying from *in situ* rock conditions. Subsequently, these may affect aperture and roughness contact distributions. The differences in surface chemistry of the epoxy, relative to the natural rock sample and the impermeability of the epoxy cast, affect the wettability of the surfaces to water. The contact angle of water on epoxy cast is approximately 63° (Geller *et al.*, 1996).

5.2. Experimental procedure

Tests are conducted by introducing water into an initially dry fracture to gradually wet the fracture. The volume of fluid entering the fracture, is manually controlled through an adjustable valve (Figure 5.10 and Figure 5.11). This is performed under constant head, with water flowing into the fracture, through means of a 6mm diameter point source.

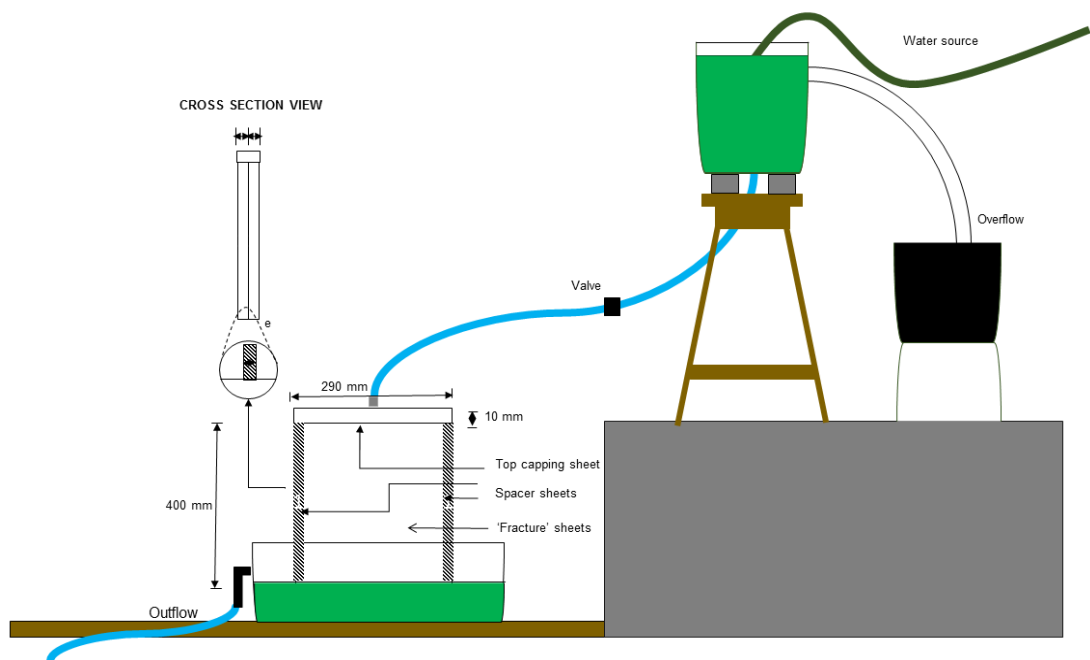


Figure 5.10: Schematic of experimental set-up

To control flow rate of fluid into the fracture, the tap is rotated to gradually increase the volume of fluid flow, assumed to be 13% at Position 1, to 100% at Position 8 or when the valve is completely rotated. The position of the tap also serves to represent each test that is conducted per experiment (Position 1 = Test 1) for the experiment run. Each test is summarised in Table 5.1. Due to small differences in the inflow velocity, for the assumed flow percentages for the different test and to highlight noticeable differences in the experiments, only the Tests 3, 5 and 8 are discussed (Figure 5.12).

A grid is placed on the outside of the opposite plexiglass sheet, facing inwards, to assess the geometry of flow mechanisms.

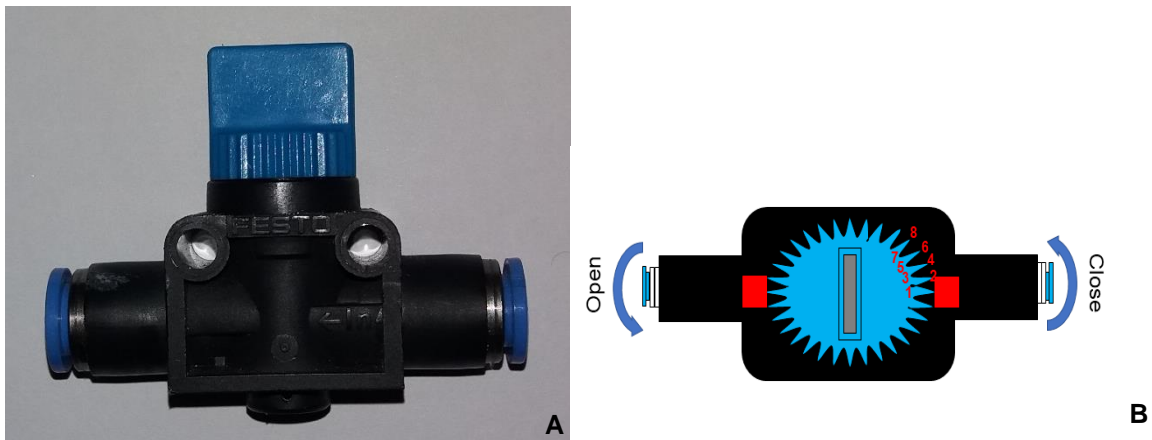


Figure 5.11: (A) Festo valve with 6mm diameter openings on either side. (B) Top view of the valve, further illustrating the numbering of the ridges. The rectangular red blocks serve as points where the ridge needs to align when opened

Table 5.1: Ridges corresponding to flow rate

Ridge	% Flow assumed	Test
1	13	1
2	25	2
3	38	3
4	50	4
5	63	5
6	75	6
7	88	7
8	100	8

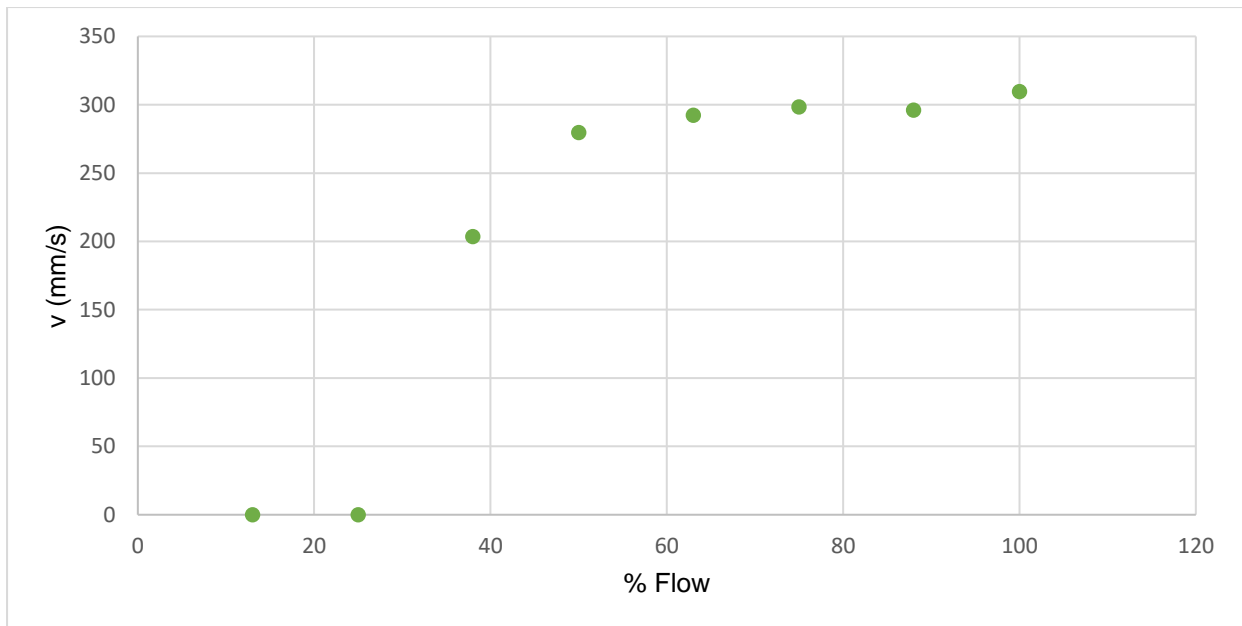


Figure 5.12: Approximated flow velocity of various tests

A video camera is placed perpendicular to and approximately 1 m from the fracture, to record each experiment. Each experiment is initiated by commencing a recording through a camera. Thirty (30) seconds thereafter, the tap on the valve is rotated to each position. Each test is concluded once a 2 l of fluid passed through the fracture. Once the experiment is completed, the recordings are analysed, and snapshots taken. Each image is annotated by: Test number; aperture; and time into the test that the snapshot was taken. Between subsequent experiments, the experimental materials are separated and dried.

CHAPTER 6 : RESULTS

The results depicted herein, are those for aperture and roughness experiments viewed from Test 3, 5 and 8 videos to highlight perceptible differences between the tests.

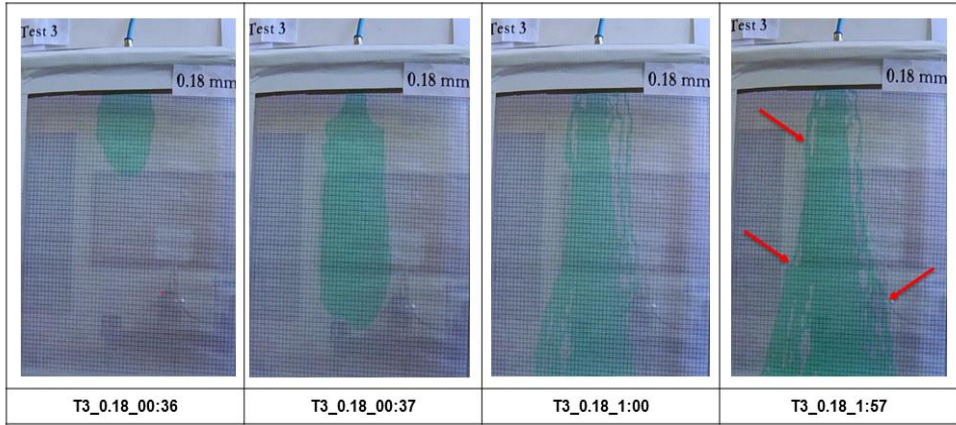
Aperture

6.1. Aperture

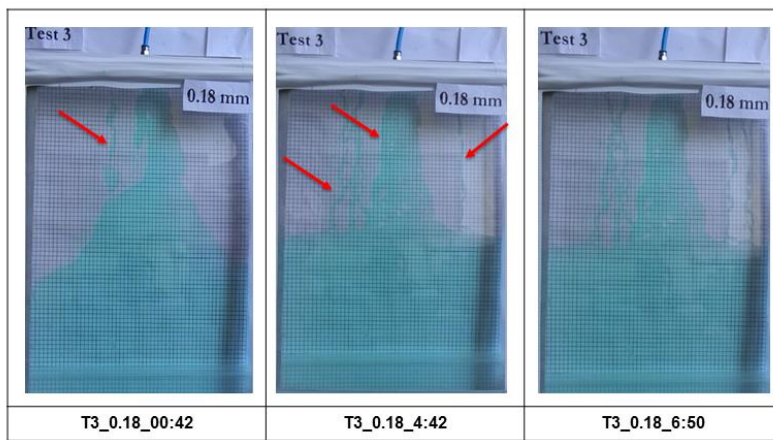
6.1.1. 0.18mm Aperture

The results of each test on the experiment containing the 0.18mm aperture fracture is indicated in Figure 6.1, 6.2 and 6.3 illustrating fluid flow through the fracture. At the lowest flow rate (Test 3), a wide wetting front is seen emerging from the inlet source, moving vertically through the centre of the fracture. Simultaneously, breakaway rivulets are observed as fluid flows laterally from the inlet. In some instances, localised rivulets breakaway from the main fluid pool and creates new isolated pathways. In another run of the experiment, Figure 6.1(B), flow is characterised ponding at the bottom of the fracture. Apart from the main rivulet, from the point source and plume, a network of two or more breakaway rivulets are also observed.

Similar observations are observed during Test 5 with an increase in flow rate, as indicated in Figure 6.2(A). A wide fluid pond bulges out from the point source, subsequently forming different sized breakaway rivulets with the main neck-sized rivulet confined to the centre. Some breakaway rivulets travel laterally towards the boundary walls of the fracture. In an additional run of the experiment, Figure 6.2(B), water bulges out from the point source, gradually forming a plume. However, the presence of an air bubble in the centre inhibits the entire fracture from completely filling up. At the highest flow rate of Test 8, as indicated in Figure 6.3, these lateral breakaway rivulets are wider, resulting in an increased percentage of the fracture being saturated.

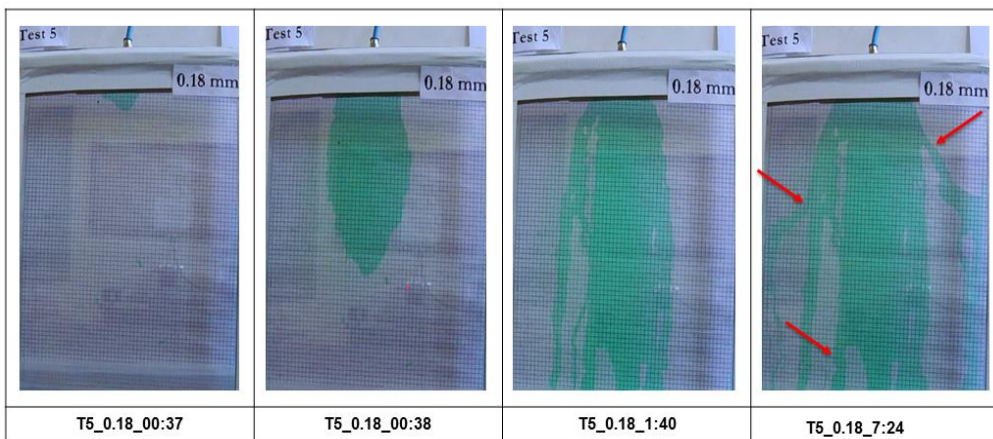


A

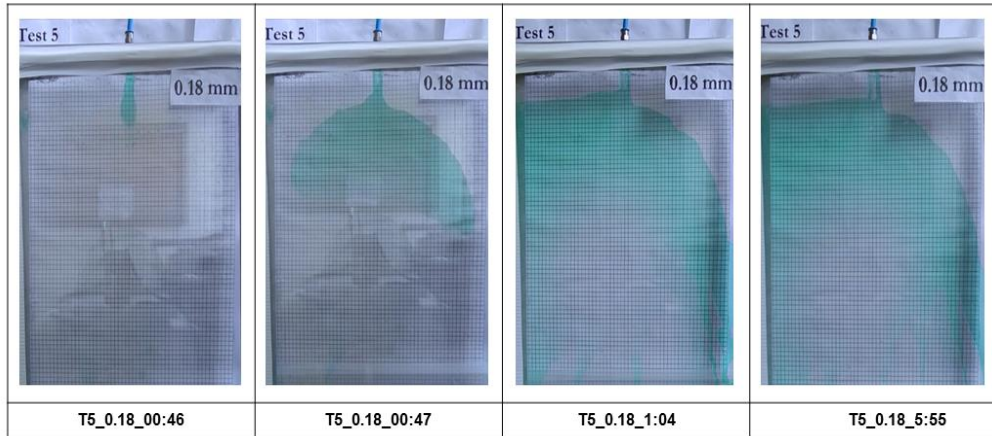


B

Figure 6.1: 0.18mm Aperture, water flow movement at 38% flow (Test 3)



A



B

Figure 6.2: 0.18mm Aperture, water flow movement at 63% flow (Test 5)

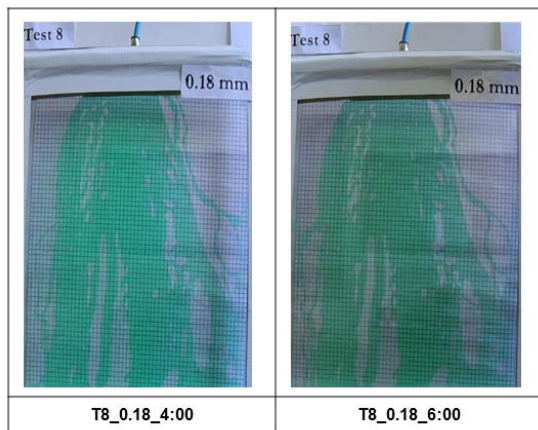
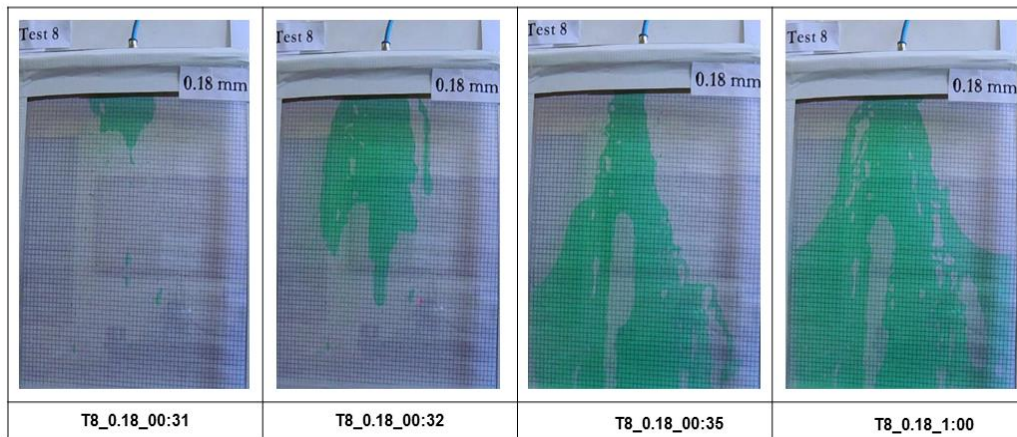


Figure 6.3: 0.18mm Aperture, water flow movement at 100% flow (Test 8)

6.1.2. 0.5mm Aperture

During Test 3, a narrow rivulet emerges from the point source with flow occurring directly down the centre of the vertical fracture, as illustrated in Figure 6.4. Some minor breakaway rivulets emerge at the base of the fracture, saturating upwards.

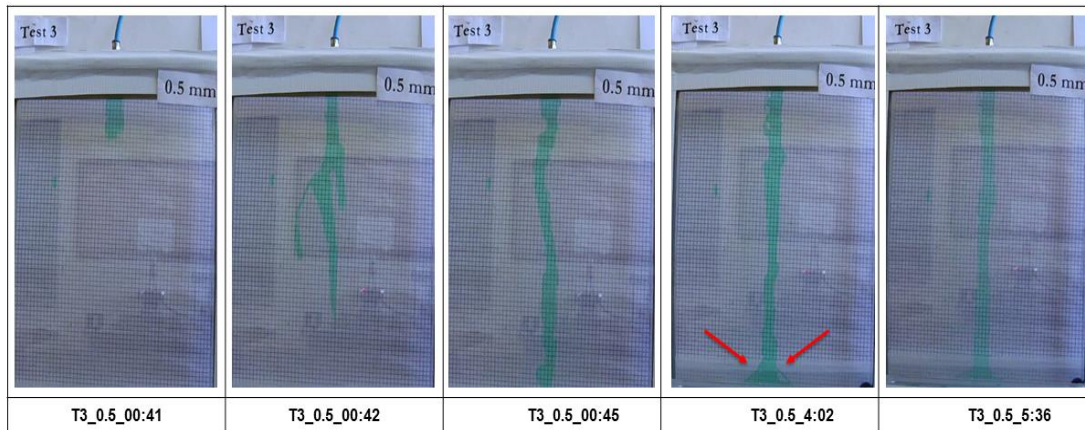


Figure 6.4: 0.5mm Aperture, water flow movement at 38% flow (Test 3)

With an increase in flow rate, a wider plume forms from point source during Test 5 and Test 8, with a larger percentage of the fracture saturating and some breakaway rivulets observed in unsaturated portions of the fracture. Faster fluid flow is observable on the edge of the plume and along some of the smaller rivulets. In addition, a network of rivulets emerges upwards from the base of the fracture. This occurs as a phreatic surface is created due to faster inflow conditions than outflow of fluid at the base of the fracture.

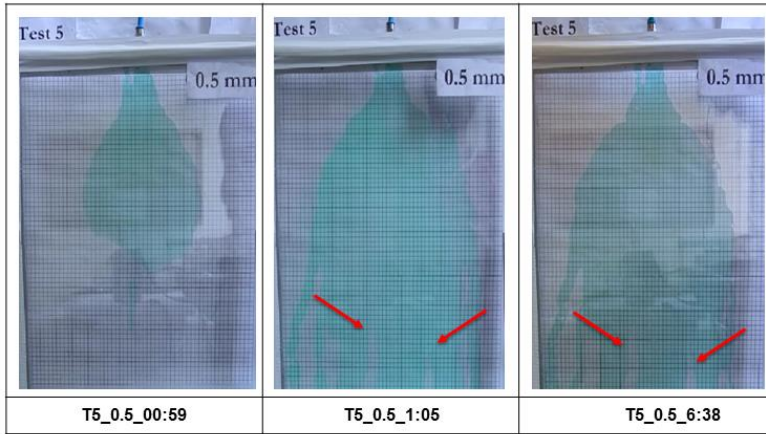
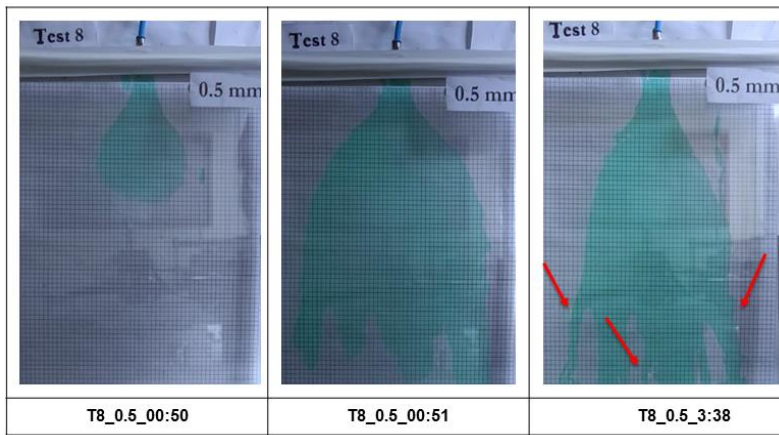
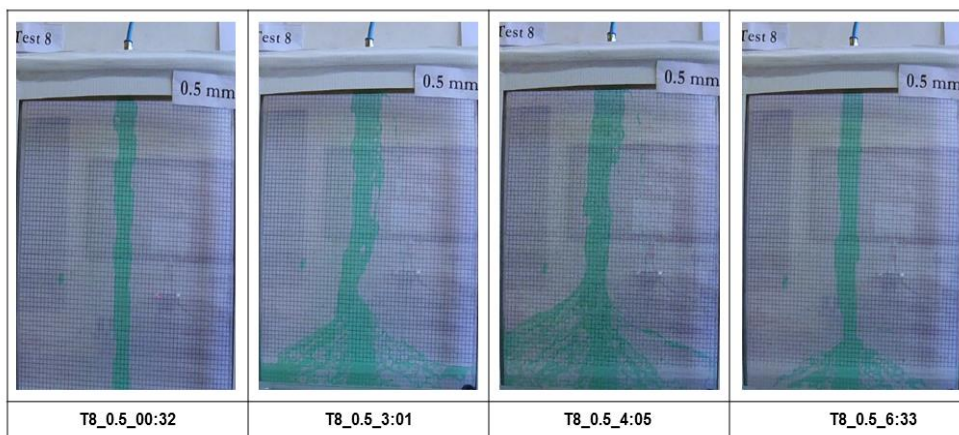


Figure 6.5: 0.5mm Aperture, water flow movement at 63% flow (Test 5)



A



B

Figure 6.6: 0.5mm Aperture, water flow movement at 100% flow (Test 8)

6.1.3. 1.0mm Aperture

A thinner rivulet emerges from the point source at the least flow rate (Test 3). Neither the fracture bottom nor the centre is saturated with water. Furthermore, numerous breakaway rivulet emerges from the rivulet resulting in multiple outflow points. As with the previous experiments (0.18 and 0.5mm), the breakaway rivulets disappear during the duration of the test, leaving only the main rivulet.

With a gradual increase in flow rate (Test 5) emerges a relatively thicker rivulet from the point source which almost immediately bulges. Water mostly flows along the path left behind by droplets from the previous test, Test 3.

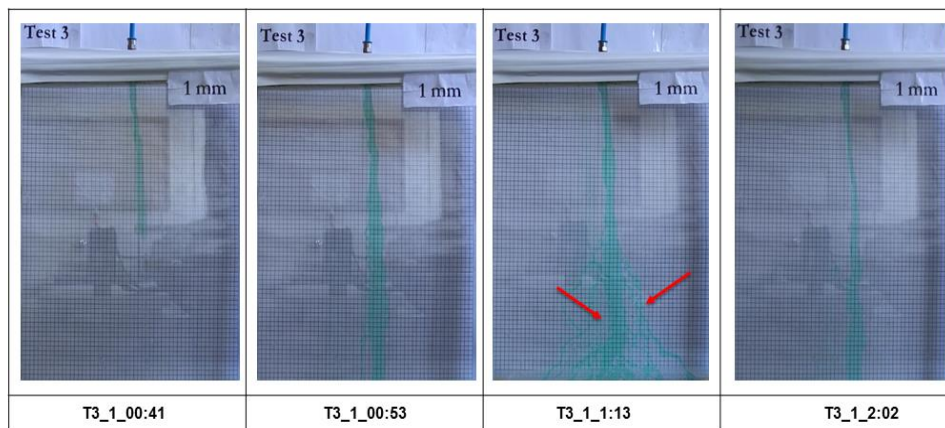


Figure 6.7: 1mm Aperture, water flow movement at 38% flow (Test 3)

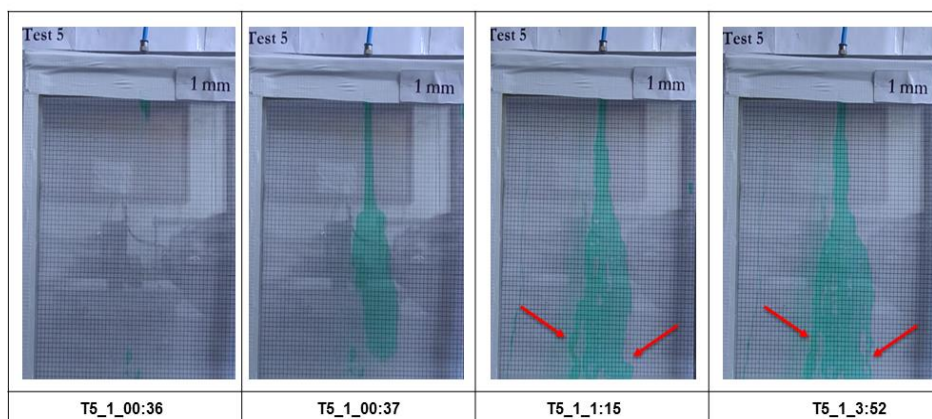


Figure 6.8: 1mm Aperture, water flow movement at 63% flow (Test 5)

Slugs of water are observable either travelling side by side with the rivulet or forming new flow pathways at the 100% flow rate. Similarly, numerous break-way rivulets emerge from the main rivulet, however, these shortly disappear leaving one or two remaining in consort with the rivulet.

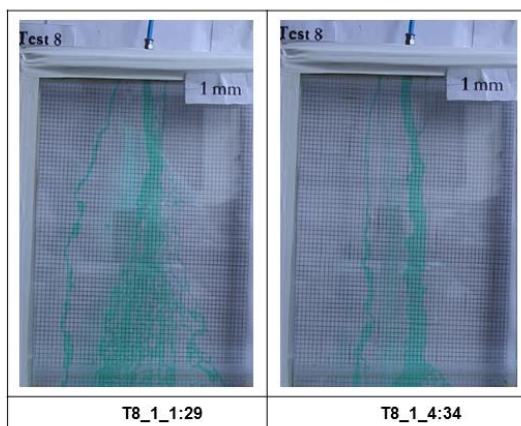
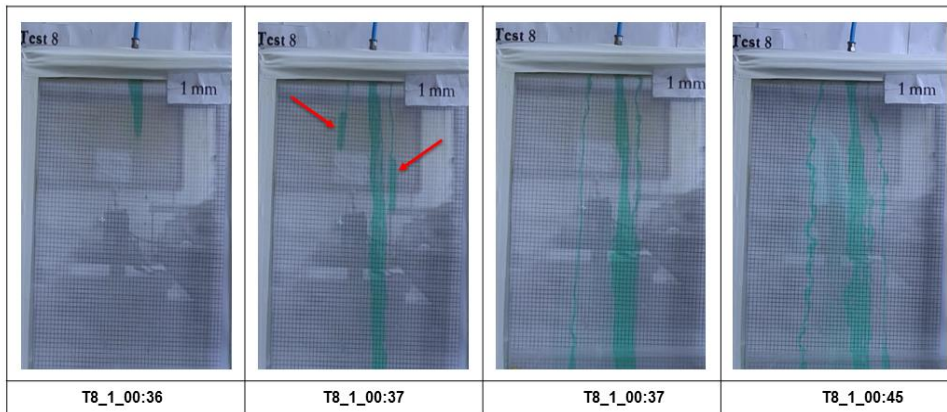


Figure 6.9: 1mm Aperture: water flow movement at 100% flow (Test 8)

6.1.4. 1.5mm Aperture

At the least flow rate (Test 3), a thinner rivulet emerges from the point source flowing in an abrupt and sinuous manner with the rivulet terminating or flow cessations on numerous counts (Figure 6.10). Flow movement becomes stable, travelling in a semi-linear and less abrupt manner.

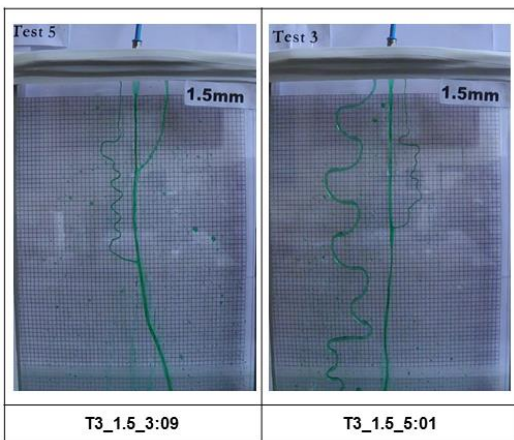
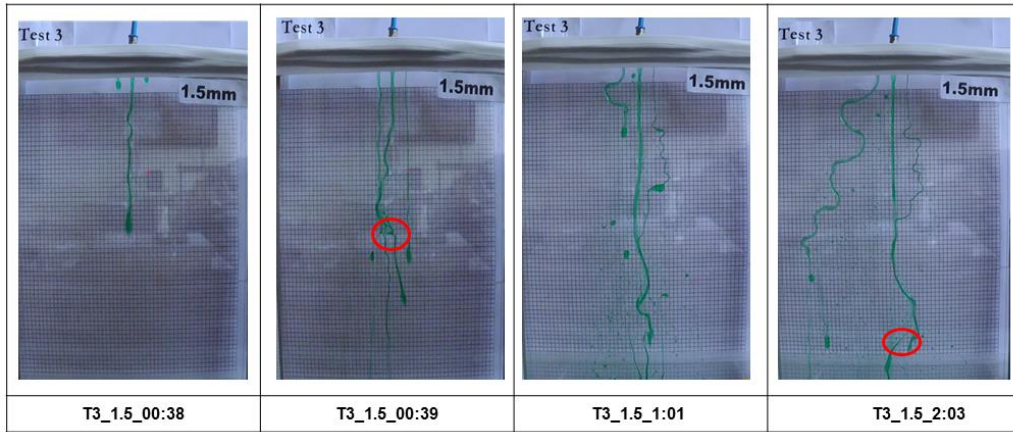


Figure 6.10: 1.5mm Aperture, water flow movement at 38% flow (Test 3)

Similar flow behaviour is also seen in Test 5 (Figure 6.11) and Test 8 (Figure 6.12) as flow rate is gradually increased. Throughout these increased flow rates, the thin rivulet remains unstable and oscillates aggressively.

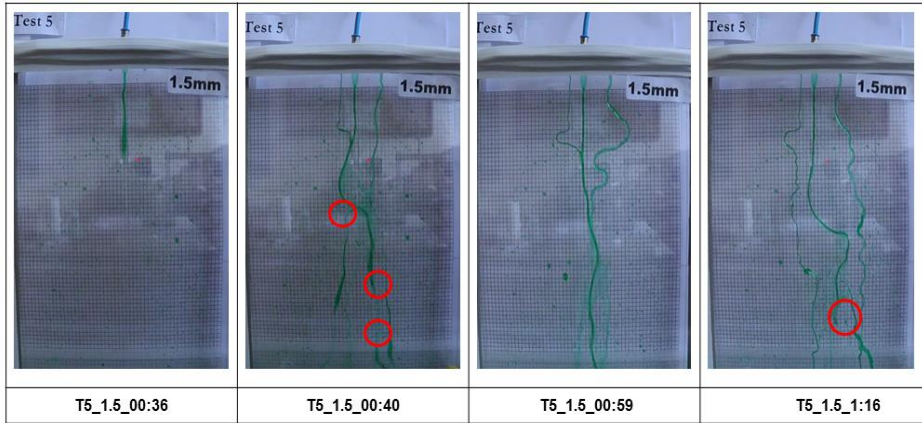


Figure 6.11: 1.5mm Aperture, water flow movement at 63% flow (Test 5)

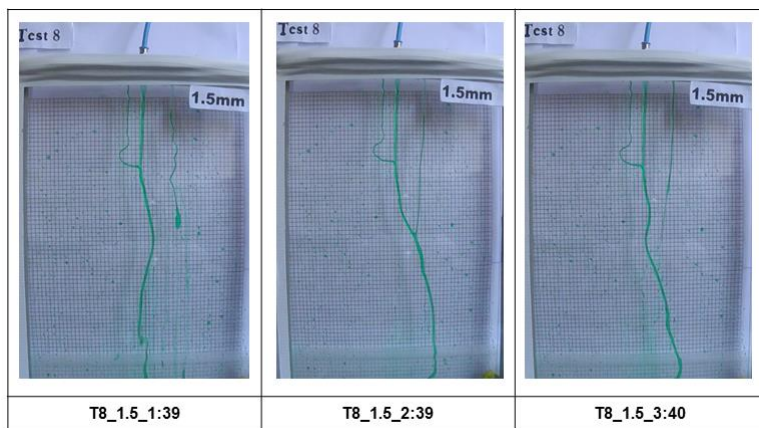
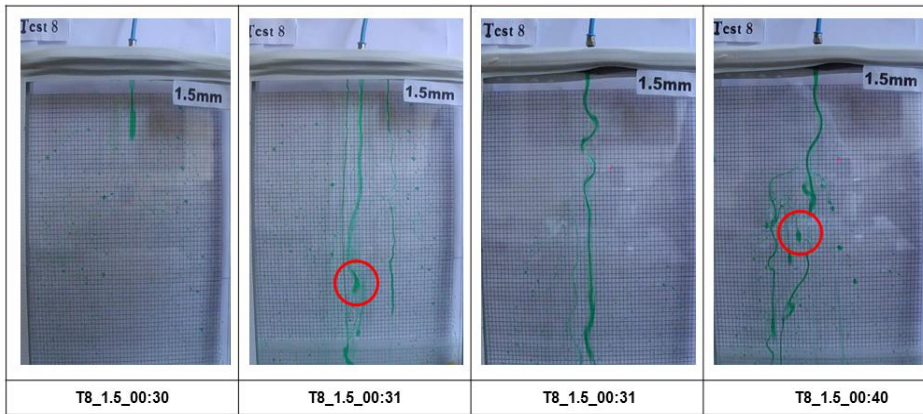


Figure 6.12: 1.5mm Aperture, water flow movement at 100% flow (Test 8)

6.1.5. 2.0mm Aperture

Similar flow behaviour to the previous experiment is observed where a thinner rivulet emerges, flowing in an abrupt and sinuous flow behaviour. Throughout the gradual increase in flow rate, the rivulet is unstable, and continues to oscillate in this sinuous manner.

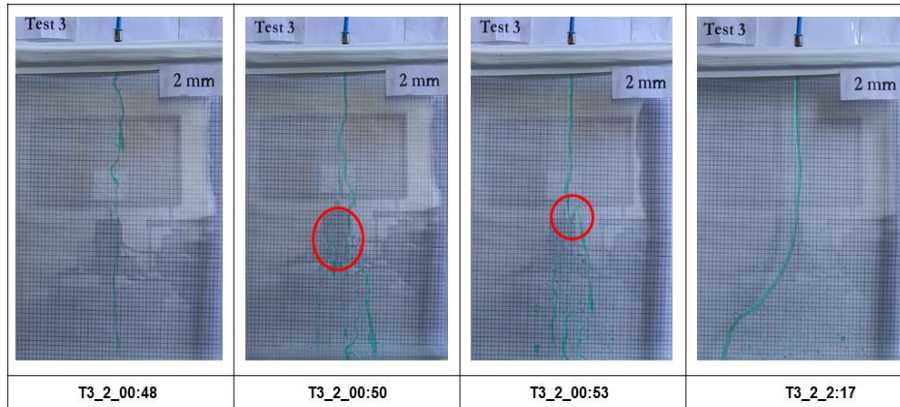


Figure 6.13: 2mm Aperture, water flow movement at 38% flow (Test 3)

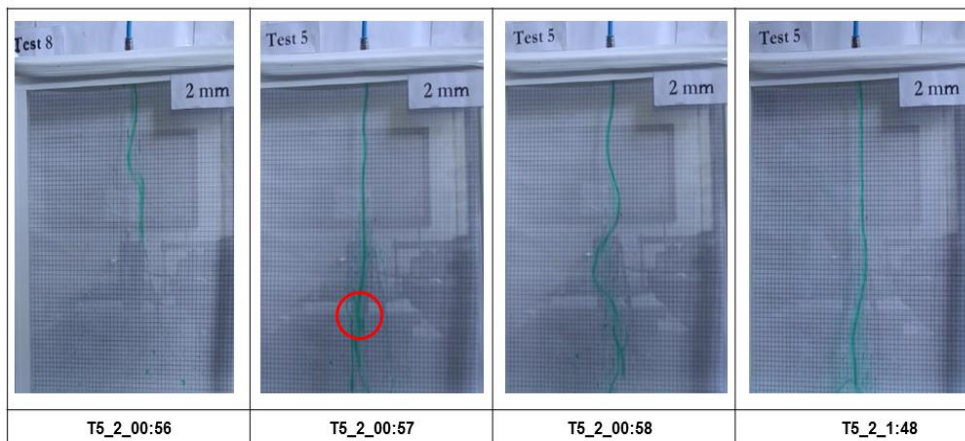


Figure 6.14: 2mm Aperture, water flow movement at 63% flow (Test 5)

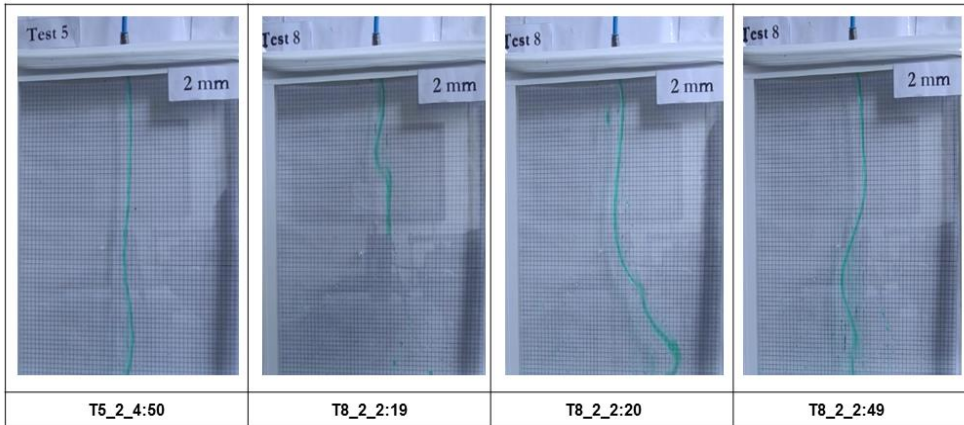


Figure 6.15: 2mm Aperture, water flow movement at 100% flow (Test 8)

6.1.6. 3.0mm Aperture

Experiments conducted at the lowest and highest flow rates are similar observations for the two previous wide aperture experiments (1.5 and 2.0mm). At the lowest flow rate (Test 3), fluid flow advances easier, is characterised by more liquid snaps and attains equilibrium much rapider. At the highest flow rate, there are lesser liquid snaps, however, the rivulet still quickly attains equilibrium with water solely travelling in a linear pathway at the same position.

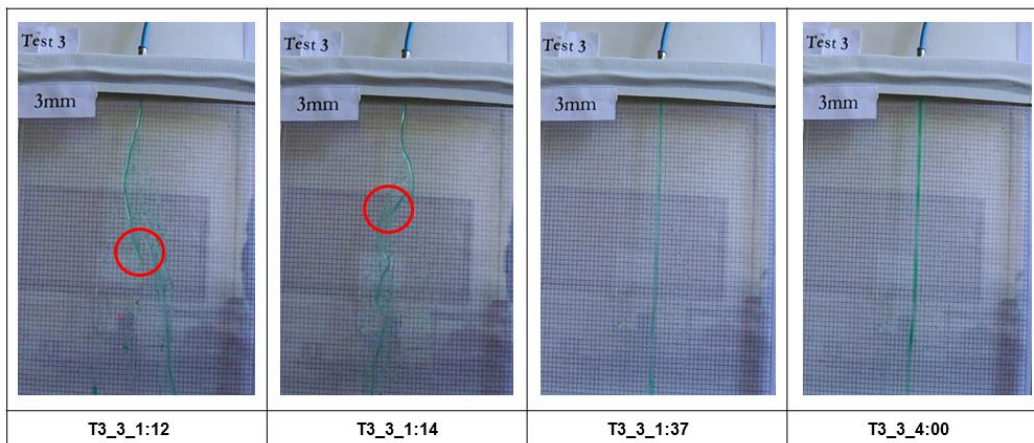


Figure 6.16: 3mm Aperture, water flow movement at 38% flow (Test 3)

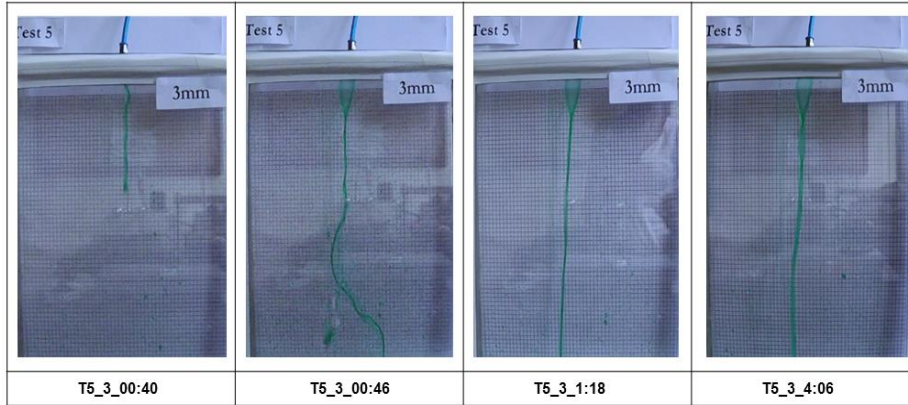


Figure 6.17: 3mm Aperture, water flow movement at 63% flow (Test 5)

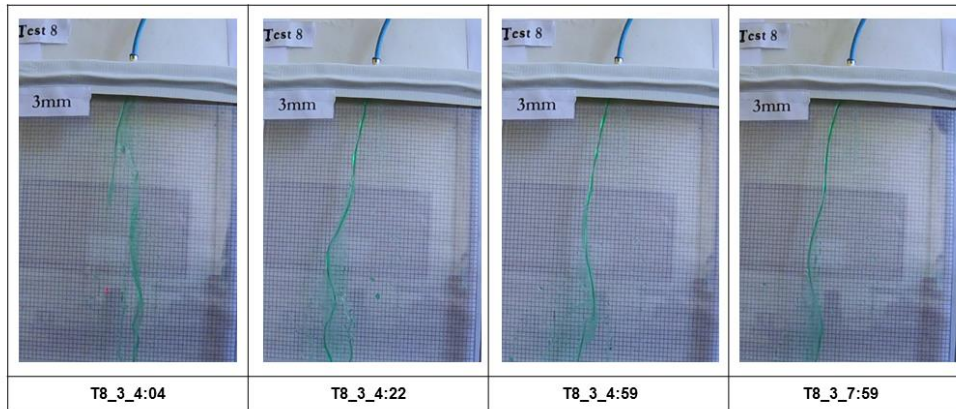


Figure 6.18: 3mm Aperture, water flow movement at 100% flow (Test 8)

Simple Darcy and cubic law equations Singhal and Gupta (2010), were used to calculate the Linear Flow Velocity and the Hydraulic Gradient, K , for each test per model experiment. Quicker water outflow is expected through fractures with narrower apertures, as indicated in Figure 6.19. Which corresponds to water either filling up the fracture bottom or the fracture centre. Conversely, a greater amount of water flow is expected in wider fractures, as indicated in Figure 6.20.

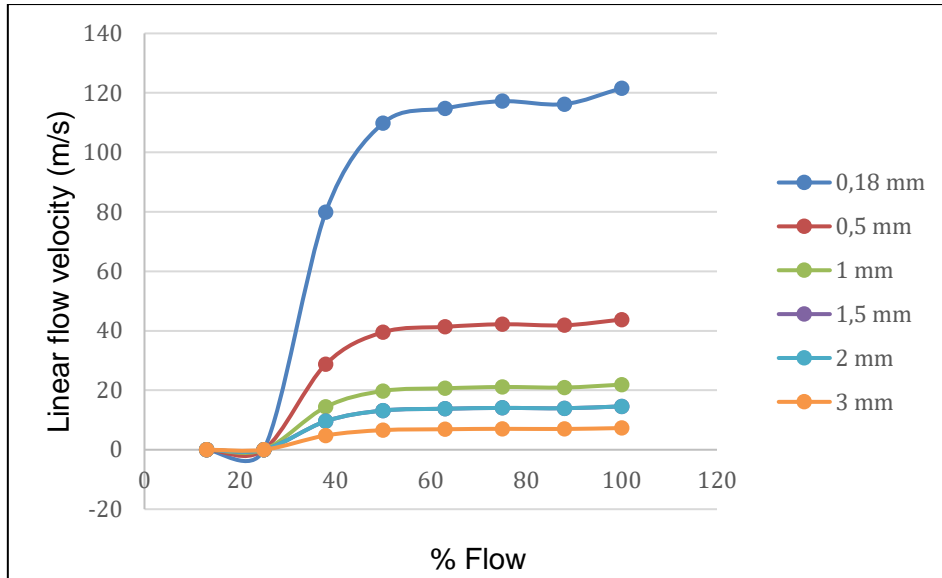


Figure 6.19: The change in linear flow velocity with a change in aperture

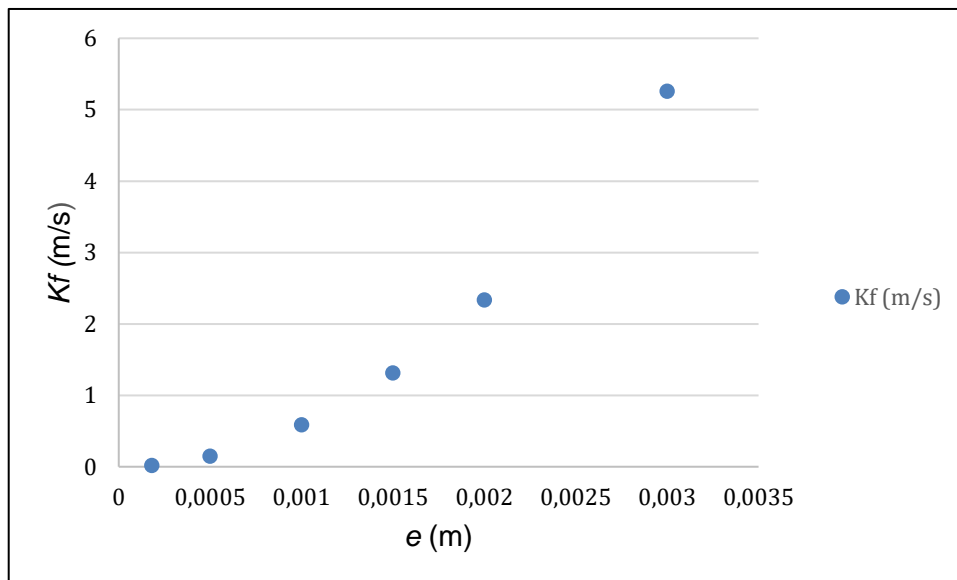


Figure 6.20: The influence of aperture (e) on fracture conductivity (K_f)

6.2. Roughness

As with the previous (aperture) experiments, a similar test set-up and procedure was used for roughness experiments. The smooth plate and either the altered or casted sample were taken apart and wiped dry for preparation of the next experiment. In experiments for surface profiles which were assumed to possess JRC values of 0-2 and 4-6, the smooth and altered plated were separated by a constant aperture of 0.5mm. Whereas no spacer was used surface profiles with JRC values 10-12 and 14-16. The spacing in between was assumed to be due to the (uneven) casted sample. The sample testing procedure was followed as with the aperture experiments.

6.2.1. R_1 (JRC 0-2)

The experimental set-up is similar to that for 0.5mm aperture (section 6.1.2) and thus observations are assumed to be similar.

6.2.2. R_2 (JRC 4-6)

At a low flow rate (Test 3); flow is characterised by an aggressively oscillating rivulet from the point source with flow cessations during flow advancement. Additional flow points emerge due to lateral flow along the horizontal plate. There is some lateral flow along the direction where encroaches have been shaped out, these also act as entrapments water droplets. The thinning out of the rivulet was ascribed to placing the sealant too close to the water in flow point.

An increase in flow rate (Test 5 and 8) results in a less thin rivulet with no flow cessations. Similarly, water droplets are briefly trapped along curves, however, additional droplets sliding along the same pathway amalgamate with the stagnant drop, further increasing its liquid mass. These eventually slide down due to the influence of gravity.

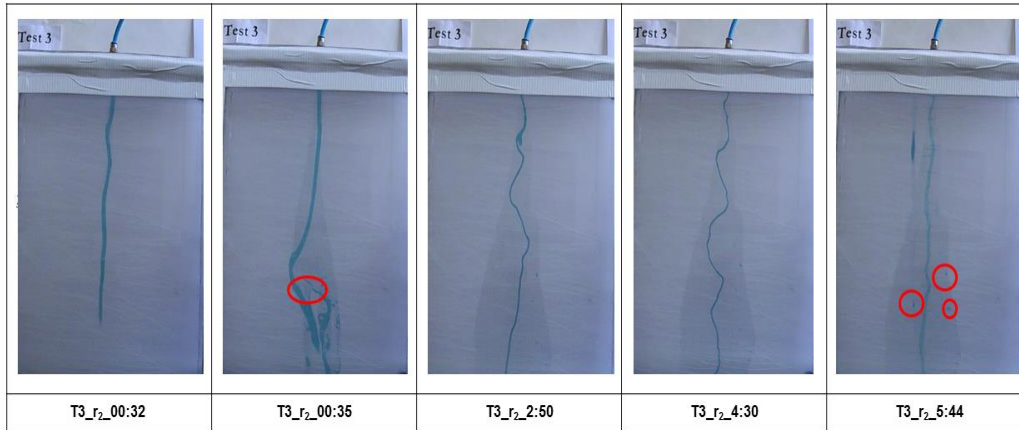


Figure 6.21: R₂ (JRC 4-6), water flow movement at 38% flow (Test 3).0

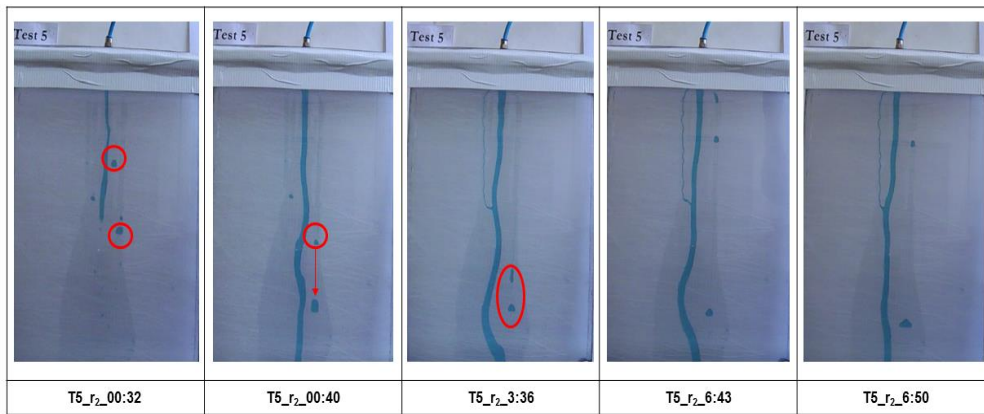


Figure 6.22: R₂ (JRC 4-6), water flow movement at 63% flow (Test 5)

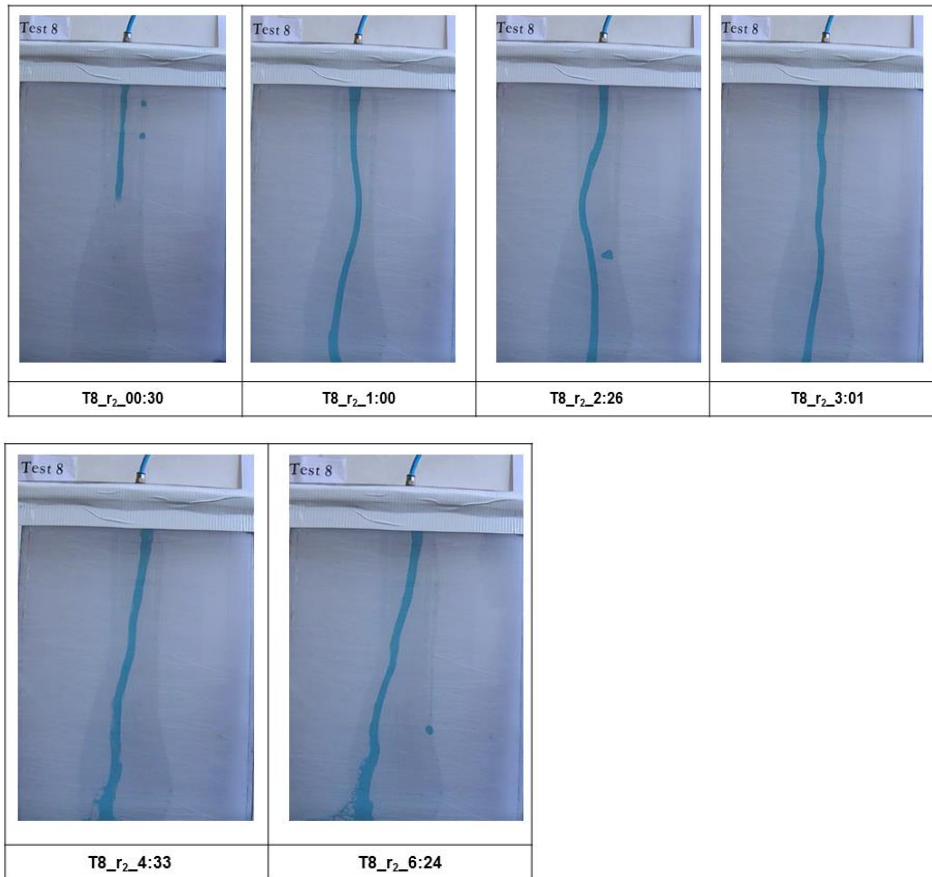


Figure 6.23: R₂ (JRC 4-6), water flow movement at 100% flow (Test 8)

6.2.3. R₃ (JRC 10-12)

A sinuous rivulet emerges with the width of the rivulet variable along its length. Along the thinner points; the dark blue colour is more pronounced. Flow cessation or flow pathway switching is observed at the contact between the smooth and uneven surface sample which further results in additional pathways. One flow path advances on the uneven sample and the other, thinner than the aforementioned, along the smooth plate.

An increase in flow rate (Test 5) results in multiple rivulets which can be attributed to lateral water flow. One rivulet advances along the sample and the other, along the smooth plate. The latter further is observed to attempt to attain equilibrium where flow path is semi-linear.

Observations in higher flow rates are similar to Test 5 and further characterised by numerous flow cessations and therefore manifestation of different pathways. The rivulet advancing along the smooth plate arises from the casted sample crest (dotted circle). It flows more sinuously, and the size of its width is lesser than the rivulet advancing along the sample.

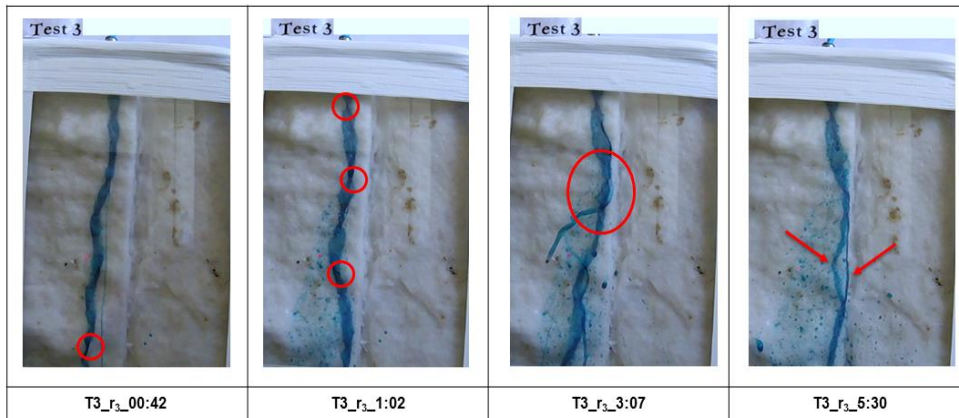


Figure 6.24: R₃ (JRC 10 - 12), water flow movement at 38% flow (Test 3)

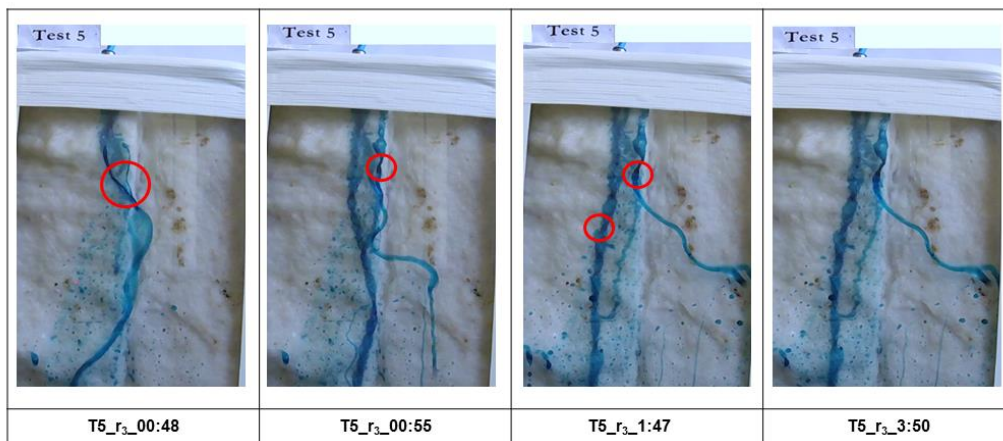


Figure 6.25: R₃ (JRC 10-12), water flow movement at 63% flow (Test 5)

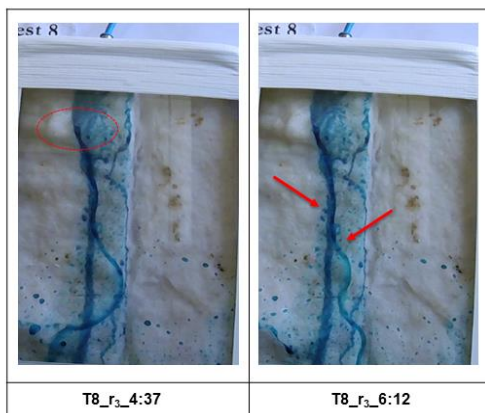
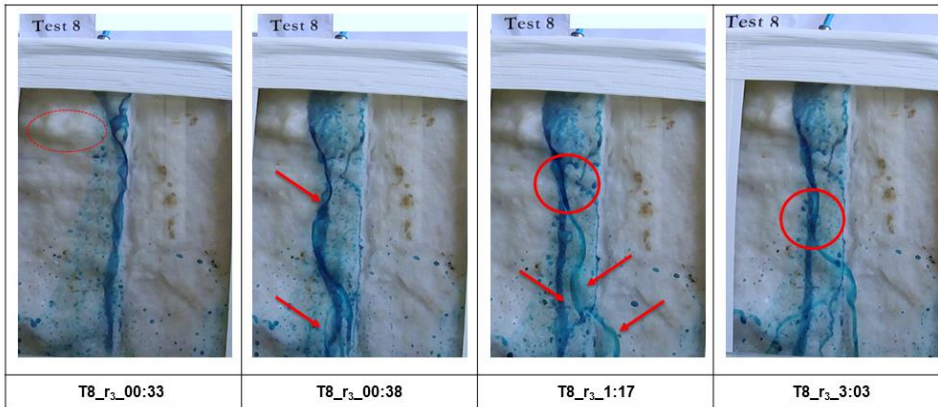
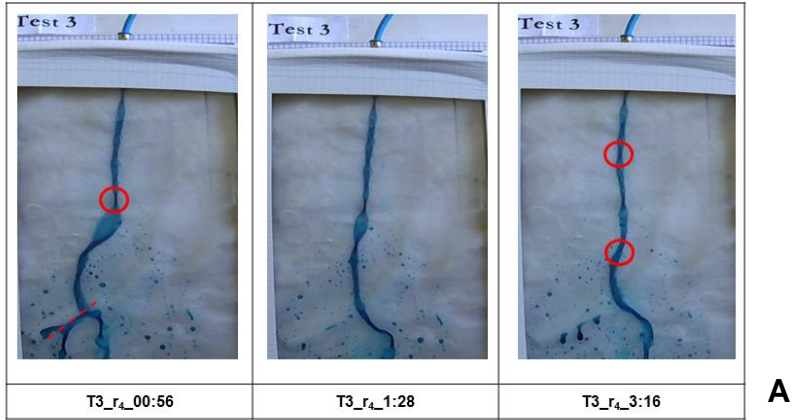


Figure 6.26: R₃ (JRC 10-12), water flow movement at 100% flow (Test 8)

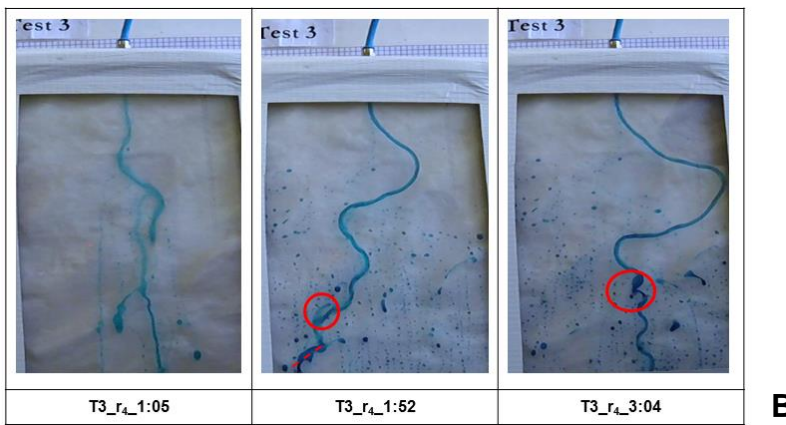
6.2.4. R₄ (JRC 14-16)

A thin rivulet emerges (Test 3) with the width of the rivulet variable along its length. Similarly, flow cessations are observed, resulting in flow pathway switching. New flow pathway is along the ridge (indicated by sub-vertical dotted line) of the uneven sample surface whilst the main rivulet attempts to attain equilibrium.

Flow behaviour does not change much with an increase in flow rate. In addition, two pathways emerge from the main rivulet.

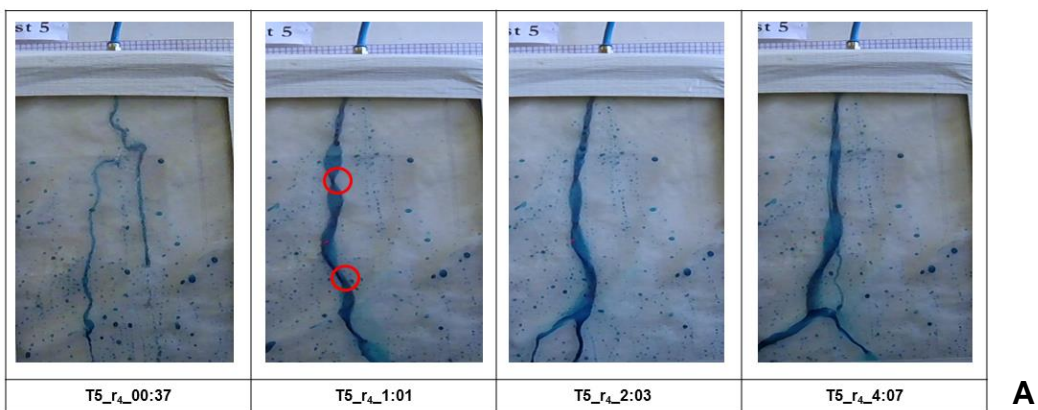


A



B

Figure 6.27: R₄ (JRC 14-16), Water flow movement at 38% flow (Test 3)



A

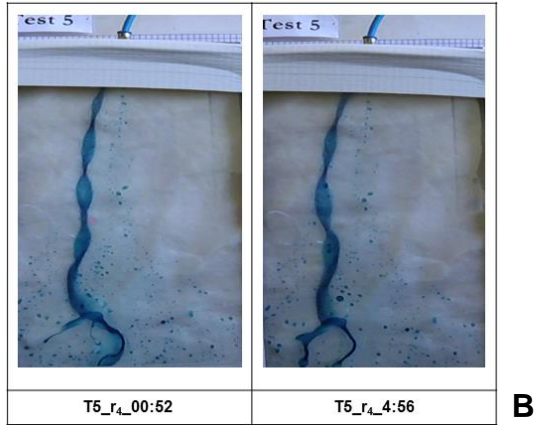


Figure 6.28: R₄ (JRC 14-16), water flow movement at 63% flow (Test 5)

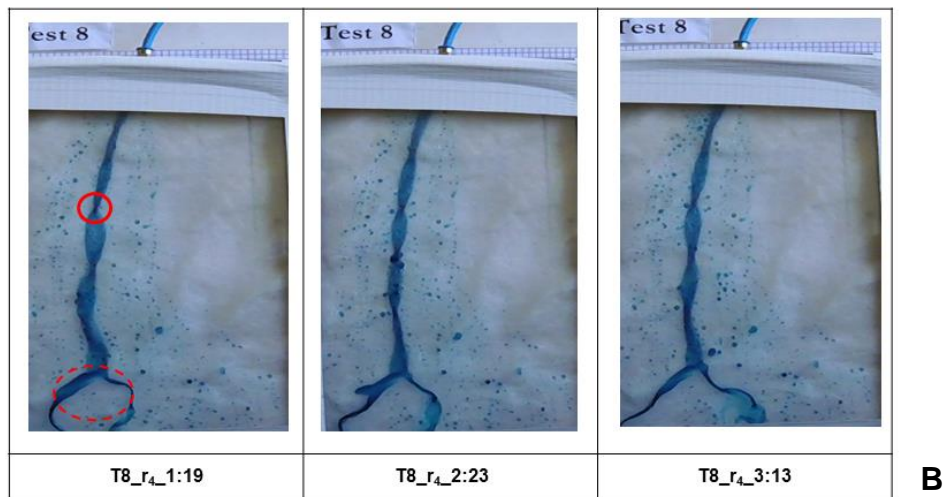
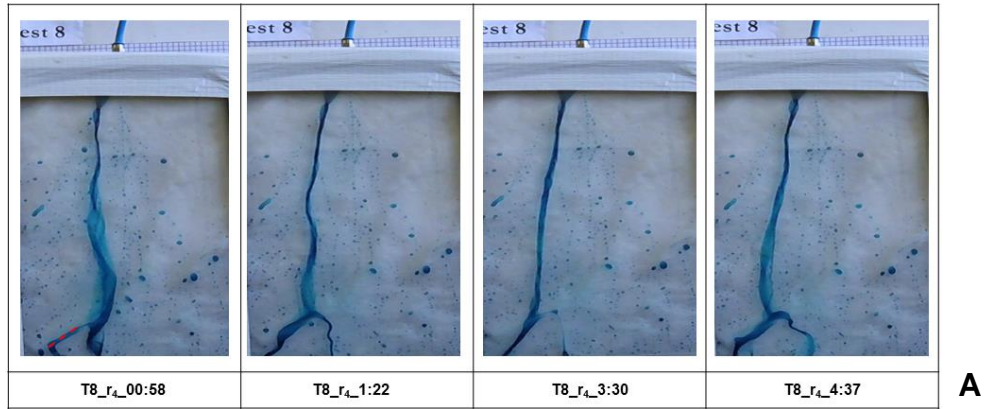


Figure 6.29: R₄ (JRC 14-16), water flow movement at 100% flow (Test 8)

CHAPTER 7 : DISCUSSION

Flow visualisation experiments were conducted on initially dry smooth parallel plates as well as epoxy-cast replicas of two naturally rock surfaces. The smooth plates were impervious with complete fluid flow occurring between the plates, whilst intermediate to high wettability was assumed for the epoxy.

Experiments on varying apertures have found that from the inlet point source, water flows sinuously through the initial quarter of the 400mm long fracture. In the narrower aperture models, (0.18mm and 0.5mm), a bulging out occurred prior to a plume forming further down the fracture. The bulging and plume development were not as pronounced in the 1mm aperture model. In some instances, flow is characterised by ponding at the fracture bottom in the narrower aperture fractures, whilst for the wider aperture, water flow is confined to breakaway rivulets forming from the main plume or rivulet. In the former scenario, water egresses along the entire fracture length; whereas, in the latter, water leaves the fracture via the breakaway rivulets, along the fracture length. An increase in flow rate or liquid volume results in an increased percentage of the fracture being saturated.

In the wider aperture experiments (1mm-3mm), the rivulet emerging from the inlet point source flows in an abrupt and sinuous manner. Throughout the gradually increasing flow rates the thin rivulet remains unstable and oscillates aggressively. The rivulet advances laterally at different points of the fracture surface, but mostly vertically with random liquid snaps within the fracture resulting in new fluid flow pathways. In comparison to the narrower aperture, no breakaway rivulets form from the main rivulet. Although not seen in the narrower aperture tests, the rivulet will attempt to attain equilibrium through flowing in a linear manner, abiding to a single pathway and subsequently egress where the rivulet is positioned.

In assuming a constant aperture of 0.5mm for two smooth plates (R_1), one observes fluid flow easily advancing through the fracture. With an increase in flow rate, a wider plume forms from point the source in consort with breakaway rivulets in unsaturated

portions of the fracture. In the R₂ visual experiments, where one of the previously smooth plates is altered (rough plate), results show few changes for Test 3 or at the least flow rate. As opposed to when both plates were smooth, no plume and breakaway rivulets form with the gradual increase in flow rate.

New rivulet or droplet pathways arise due to lateral flow along the top from the inlet point source and abrupt fluid snaps. As surface roughness is capable of leading to contact areas between fracture surfaces (Weisbrod *et al.*, 2000), these are similarly able to divert flow or result in flow switches along the fracture (indicated by sub-vertical or circular dotted lines in Figure 6.26 and Figure 6.27). Occasionally, droplets are trapped along the surface incisions. One observes a similar process described by Ghezzehei and Or (2005); whereby, with an almost constant supply of liquid droplets, these travel along the same pathway as the initially anchored droplet. The droplet is eventually detached when the mass of liquid exceeds the stabilising capillary forces.

Any separation between the uneven samples and smooth plate was assumed to result from the waviness of the two casted rock samples. There are little distinct fluid flow changes between R₃ and R₄ as troughs and crests of both sample surfaces appear to have comparable effects on fluid flow. Flow movement from the inlet source is similarly characterised by sinuous movement, however, with irregular rivulet widths, where some segments are thinner or more spread out than others. The latter can be ascribed to erratic changes in sample surface as flow advances between troughs and crests of various extremities.

A gradual increase in flow rate results in a switch; whereby, aperture and a much lesser waviness has an effect on fluid flow behaviour. This is observable by the emergence of two rivulets, with one advancing along the rock sample and the other, aggressively sinuous, advancing along the smooth plate. The size of the rivulets and numerous flow cessations are comparable to the wide aperture experiments.

From both aperture and roughness visual experiments, one mainly observes interplay between capillary, gravity and to somewhat viscous forces as a result of the glass surface. These are similar to the observations made by for e.g. Tokunaga and Wan (1997) and Su *et al.*, (1999) to name a few. In this particular study, the aforementioned

forces rather influence the liquid flow migration and to a much lesser extent the resulting flow structures. The plume forming in the narrower apertures is a result of capillary forces (small capillary number) dominating over gravity forces (low Bond number). This is due to the availability of a greater wall surface which further translates to more water flow through the fracture. Notwithstanding the formation of one or two rivulets from lateral water flow, no liquid snaps are observed.

As the available surface wall is reduced through increase in aperture, capillary forces gradually become ineffective resulting in an interchange between capillary and gravity. An interplay between the aforementioned forces is illustrated by breakaway rivulets in the 0.18mm, 0.5mm and 1mm aperture tests. Nonetheless, the extent of fracture surface being saturated suggests that capillary forces are behind fluid flow migration. In wider aperture fracture experiments, gravity dominates (high Bond number) over capillary forces (high capillary number). Hence, even under constant inlet conditions, one observes unsteady and or highly variable cycles of liquid snapping, strongly sinuous and thinner liquid rivulets; however, less snaps are observed with increase in the amount of fluid inflow.

The lack thereof of breakaway rivulets from the main rivulet for R₂ experiments suggests that surface abrasion lowers surface adhesion. The same observations are made for R₃ and R₄ experiments. As opposed to an interplay between capillary and gravity in aperture experiments, irregular width of rivulet arises from an interplay between “rock” surface wettability, and gravity, suggested by a spreading and thinning out rivulet *along* its height.

The present data collected on the feature in question at the De Hoop Dam are that it is a simple pegmatite band (Evans, 1993), identified in blocks 92 (Ch 620-Ch 650), 108 and 110 (Ch 700-Ch 720) associated with fault and shear zones initiated by the Steelpoort fault (Van Der Merwe, 2013). In addition, these presumably, occur in consort with the more complex iron-rich ultramafic pegmatites, as illustrated in Figure 4.7 and Figure 4.8, which are ubiquitous in the eastern limb of the Bushveld Complex, particularly in disturbed areas marked by extensive faulting post-Bushveld dykes (Viljoen and Scoon, 1985).

From section 4.5, the pegmatite can be grouped under fault fractures in Table 4.2, with the three prominent orientations identified as S1 140/58, S2 253 and S3 216/80. Fault fractures were further grouped into high and low permeability zone (Table 4.3) respectively possessing an average JRC value of 11.10 and 11.50 and apertures of 13.10mm and 20.30mm. High permeability fracture zones exhibited two prominent orientations, these are S1 149/64 and S2 124/11 as opposed to three in low permeability zones (Roux, 2014).

The insignificant differences in JRC values underline a vital feature that JRC can be misleading, as indicated in this instance, that a higher JRC does not imply pronounced fluid flow. Similarly, the described uneven surface experiments illustrate that an increase in the degree of roughness such as, JRC, does not necessarily translate into pronounced effect on fluid flow advancement as specified by Roy and Singh (2015).

The elemental composition, Figure 4.9, and the presence of secondary minerals, Figure 4.10, of the three samples collected from the site denotes the degree of chemical weathering undergone by the rocks. From the onsite visit, the pegmatite material, Figure 4.5 and Figure 4.6, was highly weathered, highly fractured and crumbly material. As opposed to a normal fracture where the spacing between two adjacent walls would be measured, the measured width of the pegmatite was 250mm and roughness described from the edge was slickensided and rough. Similarly, the *in situ* rock was highly weathered with closely jointed soft rock material (Appendix I).

Based on the anisotropic nature of the unsaturated fracture zone, inarguably, the visual experiments in 6.1 and 6.2 do not necessarily or out-rightly convey which aperture and roughness conditions lead to pronounced flow than others and certainly neither to any flow structures.

The visual experiments illustrate that fluid flow will preferentially flow along pathways which are easiest to advance through. With variable aperture and or roughness conditions either promoting or inhibiting flow. This is indicated by the breakaway rivulets in the narrow aperture experiments and rivulet snaps or cessations leading to

pathway “switching” or simply new pathways. This denotes an interplay between gravity and capillary forces along the smooth plate experiments. Along the casted rock and smooth plate experiments, an interplay between gravity and rock wettability unfolds. Additionally, flow pathway switching, in uneven surface experiments, occurs as result of contact areas between the uneven sample and smooth plate.

The continual mention of gravity force in the discussion illustrates a further role played by fracture orientation in either promoting or inhibiting flow the influence of fracture orientation as alluded to by Pruess (1999), Sidle *et al.* (2001) and Su *et al.* (2003), having also reporting fast preferential flow paths due to steeply dipping fractures and steep hillslopes.

The pegmatite vein in the research can be viewed as an example of the observations made by Hakami (1995), Liu *et al.* (1998) and Šimůnek *et al.*, (2003), whereby not all fractures contribute to optimum flow or to flow altogether as one would expect and, this is mainly dependent on their geological origin. With flow through an SF predominately occurs through preferential (non-uniform flow) pathways. This can further be explained by the identification of two prominent orientations in high permeability zones as opposed to three in low permeability zones.

7.1. Limitations and assumptions of this study

The observations presented in this study are limited to an over simplification of natural conditions. Notwithstanding, the results provide further basis for future physical models that ultimately seek to investigate unsaturated flow mechanisms and flow regimes. Further research needs to investigate the influence of other joint properties to ultimately make the model more representative of natural fracture conditions.

7.2. Main findings and progress

South Africa's De Hoop Dam is no exception to the various and essential purposes dams serve in various countries and in promoting economic growth. The dam supplies water to one of its districts in the Limpopo province, for construction, mining activities, and most importantly, for general use by residents (Davies, 2006; Van Vuuren, 2008). Dam infrastructure must be maintained to prevent loss of life and property. Effective and continuous monitoring of dams allow for early detection of possible dam inefficiencies and are imperative with regards to ensuring dam and human safety (Chinh and Radzicki, 2014; González De Vallejo and Ferrer, 2011).

Successful monitoring and adherence to the DSP can minimise excessive seepage rates. The latter is critical on dam stability and may ultimately result in the failure of a dam (Bedmar and Araguas, 2002, González De Vallejo and Ferrer, 2011). As in the case of De Hoop Dam, Lugeon testing prior to and post construction revealed that certain linear geological features allowed for more pronounced flow relative to adjacent fracture discontinuities. Specifically, the pegmatite vein was identified in certain foundation blocks of the dam (Appendix III). The highly weathered pegmatite falls under a class of high permeability fracture zones as classified by Roux (2014). For this reason, it is vital to understand the factors and processes governing fracture flow so that proper water seepage control strategies can be implemented (Singhal and Gupta, 2010).

The present study has examined the influence of joint parameters, aperture and roughness, on the excessive seepage of De Hoop Dam. This was achieved through means of a back analysis procedure, which was realised through an SF plexiglass model. The model was based on parallel-plate assumptions, where variously sized strips were used to simulate the appropriate aperture. Subsequently, uneven surface experiments, involved the use of an unaltered plexiglass plate with the other abraded with incisions. For the remainder of the experiments, two various rock samples of varying surfaces (unevenness) were casted.

Both aperture and roughness visual experiments demonstrate an interplay between capillary, and more so, wettability for the uneven surface experiments as well as gravity. Narrower apertures provide more contact between fluid and joint surface, thus, favouring capillary forces (low capillary number). Liquid flow migration is characterised by plume formation in consort with breakaway rivulets demonstrating some influence by gravity and the lack of liquid snaps. In contrast, wider apertures provide less contact area between water and joint surface, favouring gravity forces (high Bond number). Flow in this case is characterised by a thin rivulet with numerous flow snaps and flow pathway switching.

Uneven surface experiments suggest that surface abrasion lowers surface adhesion as suggested by the lack of breakaway rivulets from the main rivulet. The interplay between rock surface wettability and gravity, is perceived by the irregular, spreading and thinning out, width of the rivulet. Furthermore, a gradual increase in liquid mass results in a switch; whereby, aperture and to a much lesser extent, waviness has an effect on fluid flow behaviour. This is interpreted from the two rivulets observed, each advancing on a different surface such as, smooth or uneven. The size of the rivulets and number of flow cessations are comparable to those exhibited by wide aperture experiments. Furthermore, the minor differences between the average JRC values, for fracture faults grouped as those occurring in high and low permeability zones, denote that a higher JRC does not imply pronounced fluid flow and undeniably JRC can be misleading.

In conclusion:

- The aperture visual experiments illustrate that an interplay between the capillary and gravity forces (along the smooth plates) influences liquid flow migration.
- Whilst the roughness visual experiments illustrate that an interplay between gravity and rock wettability (along the casted rock and smooth plate experiments) influences liquid flow migration.
- The visual experiments do not definitely convey the aperture and roughness conditions which lead to pronounced flow than others or the occurrence of distinct flow structures.

- The visual experiments illustrate localised preferential fluid flow migration, that is, fluid flow occurring along pathways which are easiest to advance through. With variable aperture or roughness conditions either promoting or inhibiting flow. This is illustrated by breakaway rivulets in the narrow aperture experiments and in wider aperture experiments, as rivulet snaps or cessations leading to pathway switching. In roughness experiments, flow pathway switching occurs as result of contact areas between the uneven sample and smooth plate.
- The enhanced influence of gravity in most of the experiments, demonstrates a particular role played by fracture orientation, whereby it either promotes or inhibits flow. This is illustrated by the identification of two prominent orientations in high permeability fracture zones as opposed to three in low permeability zones.
- Therefore, the excessive seepage recognised in De Hoop Dam cannot be attributed to a single or definite joint parameter resulting in distinct flow structures. Rather, the variable and combined occurrence, of these fractures parameters, including aperture, roughness and orientation, results in preferential flow pathways favourable for pronounced flow relative to adjacent fractures from the site.

The site discussed in this research exemplifies the extent of how complex ground conditions can be and that fracture discontinuities should not be treated the same. As a result, evaluation of ground conditions, modelling and testing for water seepage control strategies will remain unique to a site. Research remains crucial in determining why some joints easily transmit more water than others. Therefore, to ensure that all properties of the pegmatite are accounted for; the model requires incorporating additional joint properties such as infill and changing the orientation and exploring the use of different rock samples, which will further explore the natural rock-matrix environment in transmitting fluid flow.

ACKNOWLEDGEMENTS

I thank God Almighty for the great opportunity to further my studies, strengthening and blessing me throughout the entire project. Secondly, the WRC and our steering committee, respectively, for funding and input project from Honours to the present stage of the project. I thank the National Research Foundation for investing in South African research and presenting every student with an opportunity to realise their research potential and dreams. Kobus Roux, for the initial and solid work he did on De Hoop Dam for his Honours project through the input of individuals such as Anton Van Der Merwe who allowed him to use his JLS and David Mouton who shared his in-depth experience on the engineering geological aspects of dams. My supervisor, Professor Louis van Rooy, for your time and valued comments throughout the project. Brendon Jones and Luke Brouwers - "The Fracture Flow Team AKA FFT". No words can express the gratitude I have towards you guys at the same time no words surpass THANK YOU! Thank you for your continuous input on my model - improving it and suggesting materials or items which on my own I would not have been able to come up with. Thus, I can say I am better research Engineering Geologist than I was two years ago because of your help. Last but not least, my wonderful parents - Tseleng and Kedibone Segole and my siblings - Ofentse, Mosetsi and Keamogetswe Segole, for their love, encouragement and their unwavering support.

Thank you to my editor, Ms Liza Marx from Academic and Professional Editing Services (APES), for attending to the formatting and proofreading and copy-editing of Chapters 1 to 5.

REFERENCES

- Azeemuddin, R., Roegiers, J. C., Suri, P. R., Zaman, R. & Kukreti, A. R. R. (1995, January). Stress-dependent permeability measurement of rocks in a triaxial cell. In *The 35th US Symposium on Rock Mechanics (USRMS)*. American Rock Mechanics Association.
- Bandis, S. C., Lumsden, A. C. & Barton, N. R. (1983, December). Fundamentals of rock joint deformation. In *International Journal of Rock Mechanics and Mining Sciences & Geomechanics Abstracts* (Vol. 20, No. 6, pp. 249-268). Pergamon.
- Barker, J. (1988). A generalized radial flow model for hydraulic tests in fractured rock. *Water Resources Research*, 24(10), 1796-1804.
- Barton, N. (1982). Shear-strength investigations for surface mining. In *Stability in surface mining, Proceedings 3rd international conference. Vancouver* (pp. 171 - 196).
- Barton, N. & Choubey, V. (1977). The shear-strength of rock joints in theory and practice. *Rock Mechanics and Rock Engineering*, 10(1), 1-54.
- Barton, N. & de Quadros, E. F. (1997). Joint aperture and roughness in the prediction of flow and groutability of rock masses. *International Journal of Rock Mechanics and Mining Sciences*, 34(3), 252-e1.
- Barton, N. (1973). Review of a new shear-strength criterion for rock joints. *Engineering geology*, 7(4), 287-332.
- Barton, N., Bandis, S. & Bakhtar, K. (1985, June). Strength, deformation and conductivity coupling of rock joints. In *International Journal of Rock Mechanics and Mining Sciences & Geomechanics Abstracts* (Vol. 22, No. 3, pp. 121-140). Pergamon.
- Bear, J. (1979). *Hydraulics of groundwater*. MacGraw-Hill, New-york, 567p.

- Bedmar, A. P. & Araguas, L. U. I. S. (2002). Detection and the Prevention of Leaks from Dams. CRC Press.
- Berkowitz, B. (2002). "Characterizing flow and transport in fractured geological media: A review." *Advances in Water Resources* 25(8-12): 861-884.
- Boutt, D.F., Grasselli, G., Fredrich, J. T., Cook, B.K. & Williams, J. R. (2006). Trapping zones: The effect of fracture roughness on the directional anisotropy of fluid flow and colloid transport in a single fracture. *Geophysical Research Letters*, 33(21).
- Brink, A.B. A. (1979). Engineering geology of Southern Africa. V.1.
- Brown, S. R. (1987). Fluid flow through rock joints: the effect of surface roughness. *Journal of Geophysical Research: Solid Earth (1978-2012)*, 92(B2), 1337-1347.
- Brown, S., Caprihan, A. & Hardy, R. (1998). Experimental observation of fluid flow channels in a single fracture. *Journal of Geophysical Research: Solid Earth*, 103(B3), 5125 - 5132.
- Brush, D. J. & Thompson, N. R. (2003). Fluid flow in synthetic rough-walled fractures: Navier-Stokes, Stokes, and local cubic law simulations. *Water Resources Research*, 39(4).
- Cacas, C., Ledoux, E., Marsily, G. D., Tillie, B., Barbreau, A., Durand, E. & Peaudecerf, P. (1990). Modelling fracture flow with a stochastic discrete fracture network: Calibration and validation: 1. Flow model. *Water Resources Research*, 26(3), 479-489.

- Chen, Z., Narayan, S. P., Yang, Z. & Rahman, S. S. (2000). An experimental investigation of hydraulic behaviour of fractures and joints in granitic rock. *International Journal of Rock Mechanics & Mining Sciences* 37(2000) 1061 – 1070.
- Chinh, L.m. & Radzicki, K. (2014). Using the thermal monitoring method to detect seepage and leakage of earth dykes and dams to improve the safety of flood control facilities in Vietnam.
- Cundall, P. A. & Hart, R. D. (1992). Numerical modelling of discontinua. *Engineering computations*, 9(2), 101-113.
- Davies, G. (2006). Olifants River Water Resources Development Project: De Hoop Dam: Engineering geological report for design, Volume1: Text, Volume 2: Figures, and Volume3: Appendices 1 to 3. Report Ref. No 2006-0187, dated July 2006.
- Develi, K. & Babadagli, T. (2015). Experimental and visual analysis of single-phase flow through rough fracture replicas. *International Journal of Rock Mechanics and Mining Sciences*, 73, 139-155.
- Dimadis, G., Dimadi, A. & Bacasis, I. (2014). Influence of Fracture Roughness on Aperture Fracture Surface and in Fluid Flow on Coarse-Grained Marble, Experimental Results. *Journal of Geoscience and Environment Protection*, 2(05), 59.
- Dippenaar, A., Van Rooy, J. L. & Breedts, N. (2014). Vadose Zone Hydrology: Concepts and Techniques: Report to the Water Research Commission. Water Research Commission.
- Dobson, P. F., Kneafsey, T. J., Hulen, J. & Simmons, A. (2003). Porosity, permeability, and fluid flow in the Yellowstone geothermal system, Wyoming. *Journal of Volcanology and Geothermal Research*, 123(3), 313-324.

- Dragila, m. I. & Weisbrod, N. (2003). Parameters affecting maximum fluid transport in large aperture fractures. *Advances in Water Resources*, 26(12), 1219-1228.
- Evans, A.M. (1993). Ore geology and industrial minerals: an introduction. 3rd ed. John Wiley & Sons.
- Evans, D. D., Rasmussen, T. C. & Nicholson, T. J. (2001). Flow and transport through unsaturated fractured rock: An overview (pp. 1-18). American Geophysical Union.
- Faybishenko, B., Doughty, C., Steiger, m., Long, J.C., Wood, T.R., Jacobsen, J.S., Lore, J. and Zawislanski, P.T., 2000. Conceptual model of the geometry and physics of water flow in a fractured basalt vadose zone. *Water Resour. Res*, 36(12), pp.3499-3520.
- Ge, S. (1997). A governing equation for fluid flow in rough fractures. *Water Resources Research*, 33(1), 53-61.
- Geller, J. T., Holman, H. Y., Su, G., Conrad, m. E., Pruess, K. & Hunter-Cevera, J. C. (2000). Flow dynamics and potential for biodegradation of organic contaminants in fractured rock vadose zones. *Journal of Contaminant Hydrology*, 43(1), 63-90.
- Geller, J. T., Su, G. & Pruess, K. (1996). Preliminary studies of water seepage through rough-walled fractures (No. LBNL-38810). Lawrence Berkeley National Lab., CA (United States).
- Ghezzehei, T. A. & Or, D. (2005). Liquid fragmentation and intermittent flow regimes in unsaturated fractured media. *Water resources research*, 41(12).
- González de Vallejo, L. I. G. & Ferrer, M. (2011). *Geological engineering*. CRC Press.

Guo, B. H. & Tian, C. X. (2012, October). Research advance in fluid flow through a single rock fracture. In *Applied Mechanics and Materials* (Vol. 204, pp. 628-634).

Hakami, E. & Larsson, E. (1996, June). Aperture measurements and flow experiments on a single natural fracture. In *International journal of rock mechanics and mining sciences & geomechanics abstracts* (Vol. 33, No. 4, pp. 395-404). Pergamon.

Hakami, E. (1995). *Aperture distribution of rock fractures* (Doctoral dissertation, Royal Institute of Technology).

Hendrickx, J.M. & Flury, M. (2001). Uniform and preferential flow mechanisms in the vadose zone. *Conceptual models of flow and transport in the fractured vadose zone*, 149-187.

Hillel, D. (1980). *Fundamentals of Soil Physics*.

Hoek, E. & Bray, J. D. (1981). *Rock slope engineering*. CRC Press.

<http://municipalities.co.za/demographic/127/sekhukhune-district-municipality>. Article by Yes Media. Accessed: 13 July, 2018.

<http://steelburgernews.co.za/14496/de-hoop-opening-postponed-for-second-time/> Article by Monique Labuschagne. Accessed: 10 February, 2016.

Indraratna, B. & P. Ranjith (2001). *Hydromechanical aspects and unsaturated flow in jointed rock*, AA Balkema publishers.

Indraratna, B., Ranjith, P. G. & Gale, W. (1999). Single-phase water flow through rock fractures. *Geotechnical & Geological Engineering*, 17(3-4), 211-240.

- Indraratna, B., Ranjith, P.G. & Gale, W. (2000). Single-phase water flow through rock fractures. *J. Geotech.Geol.Eng.*, 17: 1 - 37.
- ISRM (1978). Suggested methods for determining tensile strength of rock materials. *International Journal of Rock Mechanics, Mining Sciences, and Geomechanics Abstracts*, 15, 99-103.
- ISRM (1981). Suggested methods for the Quantitative Description of Discontinuities in Rock Mass determining tensile strength of rock materials. *International Journal of Rock Mechanics, Mining Sciences, and Geomechanics Abstracts*, 15(6), 319-368.
- Iwai, K. (1976). Fundamental studies of fluid flow through a single fracture (Doctoral dissertation, University of California, Berkeley).
- Jarvis, N. J. (1998). Modelling the impact of preferential flow on nonpoint source pollution. *Physical Nonequilibrium in Soils: Modelling and Application*, Ann Arbor Press, Chelsea, MI, 195-221.
- Jing, L. & Hudson, J. A. (2004). Fundamentals of the hydromechanical behaviour of rock fractures: roughness characterisation and experimental aspects. *International Journal of Rock Mechanics and Mining Sciences*, 41, 157-162.
- Jing, L. (2003). A review of techniques, advances and outstanding issues in numerical modelling for rock mechanics and rock engineering. *International Journal of Rock Mechanics and Mining Sciences*, 40(3), 283-353.
- Kapitza, P. L. & Kapitza, S. P. (1949). Wave flow of thin layers of viscous liquids. Part III. Experimental research of a wave flow regime. *Zhurnal Eksperimentalnoi i Teoreticheskoi Fiziki*, 19, 105-120.

- Knight Hall Hendry (KHH) (2015). Olifants River Water Resources Development Project (Phase 2A): De Hoop Dam. Report on Left Flank Foundation Seepage. Project Number: WP 0076.
- Kohl, T., Evans, K. F., Hopkirk, J., Jung, R. & Rybach, L. (1997). Observation and simulation of non-Darcian flow transients in fractured rock. *Water Resources Research*, 33(3), 407-418.
- Kolditz, O. (2001). Non-linear flow in fractured rock. *International Journal of Numerical Methods for Heat & Fluid Flow*, 11(6), 547-575.
- Konzuk, J. S. & Kueper, B. H. (2004). Evaluation of cubic law based models describing single-phase flow through a rough-walled fracture. *Water Resources Research*, 40(2).
- Kovács, G. (1981). *Developments in water science-seepage hydraulics*, Chap 3.2.
- Lee, C.F., Zhang, J.M. & Zhang, Y.X (1996). Evaluation and origin of ground fissures in Xian, China. *Engineering Geology*. 43(1): 45-55
- Li, B., Jiang, Y., Koyama, T., Jing, L. & Tanabashi, Y. (2008). Experimental study of the hydromechanical behaviour of rock joints using a parallel-plate model containing contact areas and artificial fractures. *International Journal of Rock Mechanics and Mining Sciences*, 45(3), 362-375.
- Liu, E. (2005). Effects of fracture aperture and roughness on hydraulic and mechanical properties of rocks: implication of seismic characterisation of fractured reservoirs. *Journal of Geophysics and Engineering*, 2(1), 38.
- Liu, H. H., Doughty, C. & Bodvarsson, G. S. (1998). An active fracture model for unsaturated flow and transport in fractured rocks. *Water Resources Research*, 34(10), 2633-2646.

- Lomize, G.M. (1951). Water flow through jointed rock, Gosenergoizdat, Moscow (in Russian).
- Louis. (1969). A study of groundwater flow in jointed rock and its influence on the stability of rock masses. Imperial College of Science and Technology.
- Méheust, Y. & Schmittbuhl, J. (2003). Scale effects related to flow in rough fractures. *Pure and Applied Geophysics*, 160(5-6), 1023-1050.
- Nicholson, T. & Evans, D. D. (1987). Flow and transport through unsaturated fractured rock. *Eos, Transactions American Geophysical Union*, 68(43), 1155-1156.
- Nylstroom 2428 (1978) 1:250 000 Geological Series, Geological Survey, Pretoria.
- Or, D. & Ghezzehei, T.A. (2007). Travelling liquid bridges in unsaturated fractured porous media. *Transport in porous media*, 68(1), 129-151.
- Oron, A. P. & Berkowitz, B. (1998). Flow in Rock Fractures: The Local Cubic Law Assumption Reexamined. *Water Resources Research*, 34, 2811-2825. <http://dx.doi.org/10.1029/98WR02285>.
- PILGRIM'S REST, Sheet 2430. (2000). 1:250 000 Topocadastral Series, Government Printer, Pretoria.
- Pruess, K. (1999). A mechanistic model for water seepage through thick unsaturated zones in fractured rocks of low matrix permeability. *Water Resources Research*, 35(4), 1039-1051.
- Pyrak-Nolte, L. J. & Morris, J. P. (2000). Single fractures under normal stress: The relation between fracture specific stiffness and fluid flow. *International Journal of Rock Mechanics and Mining Sciences*, 37(1), 245-262.

- Pyrak-Nolte, L.J. (1996). The seismic response of fractures and interrelations among fracture properties. *INTERNATIONAL JOURNAL OF ROCK MECHANICS AND MINING & GEOMECHANICS ABSTRACTS*, 33(8).
- Pyrak-Nolte, L.J. Cook, N.G. & Nolte, D.D. (1988). Fluid percolation through single fractures. *Geophysical Research Letters*, (15), 1247-1250.
- Pyrak-Nolte, L.J., Myer, L.R., Cook, N. G. & Witherspoon, P.A (1987, January). Hydraulic and mechanical properties of natural fractures in low permeability rock. In 6th ISRM Congress. International Society for Rock Mechanics.
- Qian, J., Chen, Z., Zhan, H. & Guan, H. (2011). Experimental study of the effect of roughness and Reynolds number on fluid flow in rough-walled single fractures: a check of local cubic law. *Hydrological Processes*, 25(4), 614-622.
- Qian, J., Zhan, H., Luo, S. & Zhao, W. (2007). Experimental evidence of scale-dependent hydraulic conductivity for fully developed turbulent flow in a single fracture. *Journal of hydrology*, 339(3), 206-215.
- Qian, J., Zhan, H., Zhao, W. & Sun, F. (2005). Experimental study of turbulent unconfined groundwater flow in a single fracture. *Journal of Hydrology*, 311(1), 134-142.
- Ranjith, P. G. (2010). "An experimental study of single and two-phase fluid flow through fractured granite specimens." *Environ. Earth Sci.*, 59(7), 1389-1395.
- Ranjith, P.G. & Viete, D.R. (2011). Applicability of 'cubic law' for non-Darcian fracture flow. *Journal of Petroleum Science and Engineering*, 78(2), 321-327.
- Ranjith, P.G. (2000). Analytical and Experimental Modelling of Coupled Water and Air Flow through Rock Joints. PhD thesis, University of Wollongong, Australia.

- Read, m. D., Meredith, P. G. & Murrell, S. A. F. (1989, January). Permeability measurement techniques under hydrostatic and deviatoric stress conditions. In ISRM International Symposium. International Society for Rock Mechanics.
- Reynolds, O. (1883). XXIX. An experimental investigation of the circumstances which determine whether the motion of water shall be direct or sinuous, and of the law of resistance in parallel channels. Philosophical Transactions of the Royal Society of London, 174, 935-982.
- Roux, J.I. (2014). Finding a relationship between discontinuity characterisation parameters and Lugeon values in the foundation of De Hoop Dam near Steelpoort, South Africa. Site Investigation Project 713. Department of Geology, University of Pretoria.
- Roy, D.G. & Singh, T.N. (2015, January). A Numerical Study on the Effect of Surface Roughness on the Fluid Flow through Rock Joint. Paper presented at the GEOINDIA 2015 & 3rd South Asian Geosciences Conference & Exhibition, New Delhi, India.
- Rutqvist, J., Wu, Y. S., Tsang, C. F. & Bodvarsson, G. (2002). A modelling approach for analysis of coupled multiphase fluid flow, heat transfer, and deformation in fractured porous rock. International Journal of Rock Mechanics and Mining Sciences, 39(4), 429-442.
- Sahimi, M. (2011). Flow and transport in porous media and fractured rock: from classical methods to modern approaches. John Wiley & Sons.
- Scesi, L. & Gattinoni, P. (2007). Roughness control on hydraulic conductivity in fractured rocks. Hydrogeology Journal, 15(2), 201-211.
- Scoon, R. N. & Mitchell, A. A. (2004). Petrogenesis of discordant magnesian dunite pipes from the central sector of the eastern Bushveld Complex with emphasis on the

Winnaarshoek Pipe and disruption of the Merensky Reef. *Economic Geology*, 99(3), 517-541.

Sidle, R. C., Noguchi, S., Tsuboyama, Y. & Laursen, K. (2001). A conceptual model of preferential flow systems in forested hillslopes: Evidence of self-organization. *Hydrological Processes*, 15(10), 1675-1692.

Šimůnek, J., Jarvis, N. J., Van Genuchten, m. T. & Gärdenäs, A. (2003). Review and comparison of models for describing nonequilibrium and preferential flow and transport in the vadose zone. *Journal of Hydrology*, 272(1), 14-35.

Singhal, B. B. S. & Gupta, R. P. (2010). *Applied hydrogeology of fractured rocks*. Springer Science & Business Media.

Stimpson, B. (1970). Modelling materials for engineering rock mechanics. *International Journal of Rock Mechanics and Mining Sciences & Geomechanics Abstracts*, 7, 77-121.

Su, G. W., Geller, J. T., Pruess, K. & Wen, F. (1999). Experimental studies of water seepage and intermittent flow in unsaturated, rough-walled fractures. *Water resources research*, 35(4), 1019-1037.

Su, G. W., Nimmo, J. R. & Dragila, M. I. (2003). Effect of isolated fractures on accelerated flow in unsaturated porous rock. *Water resources research*, 39(12).

Su, G.W., Geller, J.T., Hunt, J.R., Pruess, K. (2004). Small-scale features of gravity-driven flow in unsaturated fractures. *Vadose Zone J.* 3(2), 592-601.

Sun, J. P. & Zhao, Z. Y. (2011, September). Influences of Fracture Aperture and Roughness on Hydraulic Conductivity in Fractured Rock Mass. In *RECENT PROGRESSES IN FLUID DYNAMICS RESEARCH: Proceeding of the Sixth*

International Conference on Fluid Mechanics (Vol. 1376, No. 1, pp. 372-374).
AIP Publishing.

Thiel, K. (1989). Rock Mechanics in Hydro engineering. Developments in Geotechnical Engineering, Vol. 51. Elsevier, Amsterdam, 408 p.

Thompson, m.E. & Brown, S.R. (1991). The effect of anisotropic surface roughness on flow and transport in fractures. *Journal of Geophysical Research: Solid Earth*, 96(B13), 21923-21932.

Tokunaga, T. K. & Wan, J. (1997). Water film flow along fracture surfaces of porous rock. *Water Resources Research*, 33(6), 1287-1295.

Tsang, Y. W. & Tsang, C. F. (1987). Channel model of flow through fractured media. *Water Resources Research*, 23(3), 467-479.

Tsang, Y. W. (1992). Usage of "equivalent aperture" for rock and tracer tests. *Water Resources Research*, 28 (5), 1451 - 1455.

Tsang, Y.W. (1984). The effect of tortuosity on fluid flow through a single fracture. *Water Resources Research*, 20(9), 1209-1215.

Tzelepis, V., Moutsopoulos, K. N., Papaspyros, J. N. & Tsihrintzis, V. A. (2015). Experimental investigation of flow behaviour in smooth and rough artificial fractures. *Journal of Hydrology*, 521, 108-118.

Van Der Merwe, (2013). *De Hoop Dam. Geological Completion Report*. Pretoria: Knight Piesold, pp.1-8.

Van Vuuren, L. (2008). Water crucial to wealth building in Limpopo. *The Water Wheel*, 7(4), p.28.

- Viljoen, m. J. & Scoon, R. N. (1985). The distribution and main geologic features of discordant bodies of iron-rich ultramafic pegmatite in the Bushveld Complex. *Economic Geology*, 80(4), 1109-1128.
- Weinert, H. H. (1980). Natural road construction materials of Southern Africa. CSIR.
- Weisbrod, N., Nativ, R., Adar, E.M., Ronen, D. & Ben-Nun, A. (2000). Impact of coating and weathering on the properties of chalk fracture surfaces. *Journal of Geophysical Research: Solid Earth*, 105(B12), 27853-27864.
- Witherspoon, P. A., Wang, J. S. Y., Iwai, K. & Gale, J. E. (1980). Validity of cubic law for fluid flow in a deformable rock fracture. *Water resources research*, 16(6), 1016-1024.
- Wu, Y. S. (2002). Numerical simulation of single-phase and multiphase non-Darcy flow in porous and fractured reservoirs. *Transport in Porous Media*, 49(2), 209-240.
- Zhang, X. & Sanderson, D. J. (Eds.). (2002). Numerical modelling and analysis of fluid flow and deformation of fractured rock masses. Elsevier.
- Zimmerman, R. W. & Bodvarsson, G. S. (1996). Hydraulic conductivity of rock fractures. *Transport in porous media*, 23(1), 1-30.
- Zimmerman, R. W., Kumar, S. & Bodvarsson, G. S. (1991, July). Lubrication theory analysis of the permeability of rough-walled fractures. In *International Journal of Rock Mechanics and Mining Sciences & Geomechanics Abstracts* (Vol. 28, No. 4, pp. 325-331). Pergamon.
- Zimmerman, R.W. & Yeo, I. W. (2000). Fluid Flow in Rock Fractures: From the Navier-Stokes Equations to the Cubic Law. *Dynamics of fluids in fractured rock*, 213-224.

Zimmerman, R.W., Al-Yaarubi, A., Pain, C.C. & Grattoni, C.A. (2004). Non-linear regimes of fluid flow in rock fractures. *International Journal of Rock Mechanics and Mining Sciences*, 41, 163-169.

APPENDIX I *IN SITU* JOINT LINE DESCRIPTIONS

∞ **Pegmatite vein description**

Highly weathered rock, coarse-grained, highly fractured, loose, crumbly material - gravelly sand. Roughness on edge: slickensides and rough; width = 250mm; wavelength = 800mm, 75/135; 73/153; 82/150; 78/308; 75/305; 75/130; 70/124; 80/147

UCS = 29MPa

UCS = 75 (strong rock)

∞ ***In situ* rock description**

Dark olive stained and streaked black/dark purple, highly weathered, medium to coarse-grained, closely jointed (<15mm, 4mm, 13mm, 11mm), Soft rock

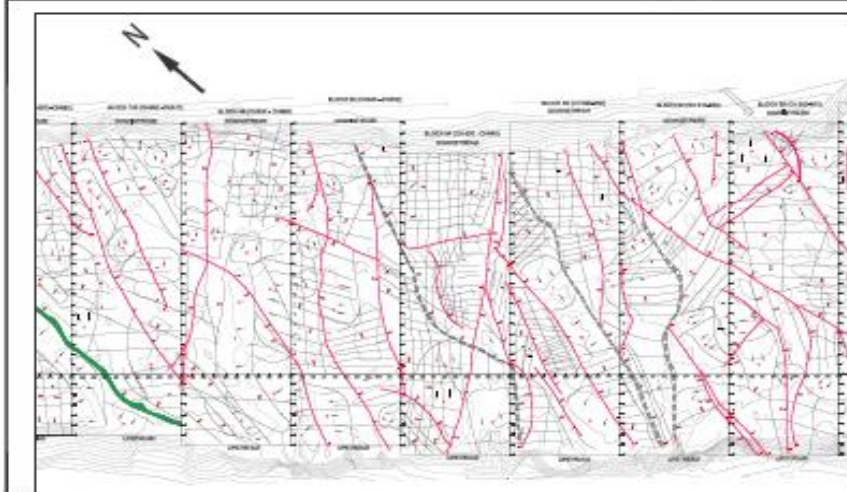
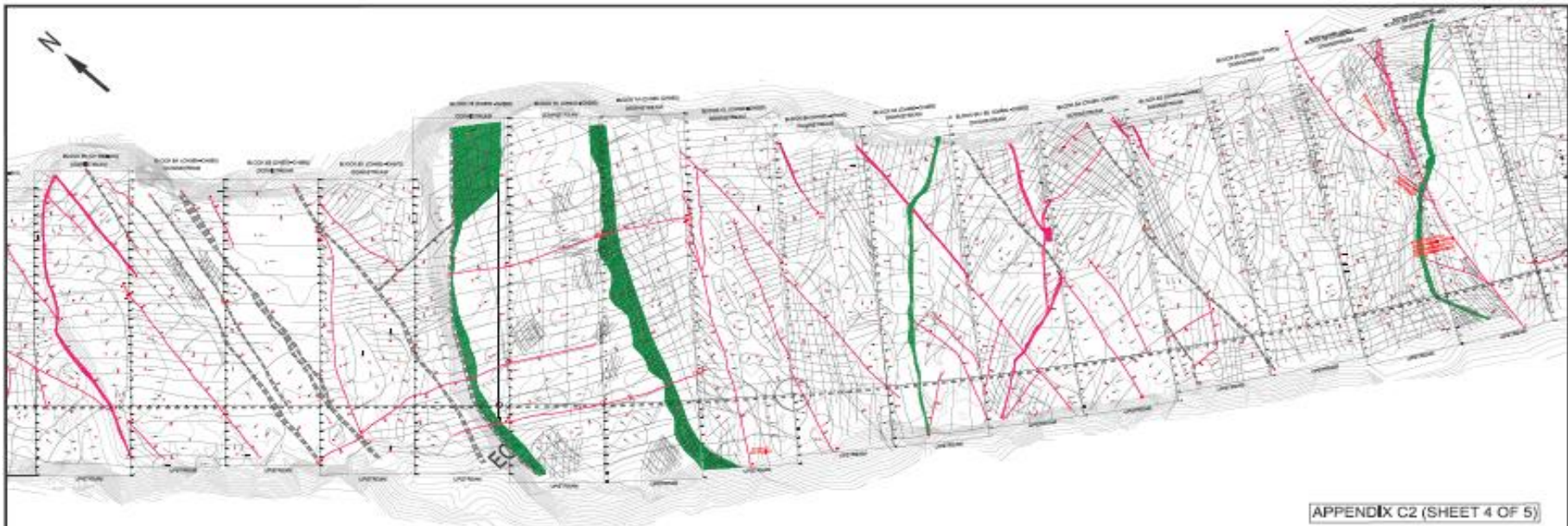
In situ soil description: Dark brownish green, loose, slightly moist, intact, gravelly sandy silt.

∞ **Description of blast damages**

Weathered soft rock, dark olive, highly jointed and open width = 240mm, rough and wavy; wavelength 800mm. (73/110, 70/105, 78/100)

UCS 25MPa (moderately strong)

APPENDIX II AS-BUILT FOUNDATION MAPS



LEGEND	
	AREA TO BE ACQUIRED
	AREA TO BE EXPROPRIATED
	PROPOSED ROAD
	PROPOSED RAILROAD
	PROPOSED CANAL
	PROPOSED DRAINAGE CANAL
	PROPOSED FLOOD CONTROL CANAL
	PROPOSED IRRIGATION CANAL
	PROPOSED POWER LINE
	PROPOSED TELEPHONE LINE
	PROPOSED WATER MAIN
	PROPOSED SEWER MAIN

		De Hoop Dam	
DIVISION OF DAMS AND WEIERS OFFICE OF THE DISTRICT ENGINEER DIVISION OF DAMS AND WEIERS OFFICE OF THE DISTRICT ENGINEER		DIVISION OF DAMS AND WEIERS OFFICE OF THE DISTRICT ENGINEER	
NO. 100 100-100-100	DATE 10-10-10	SCALE 1:1000	SHEET NO. 100
PROJECT NO. 100-100-100	TITLE 100-100-100	DRAWN BY 100-100-100	CHECKED BY 100-100-100

APPENDIX III PEGMATITE VEIN IDENTIFIED IN DIFFERENT FOUNDATION BLOCKS

